

## **Copyright Warning & Restrictions**

The copyright law of the United States (Title 17, United States Code) governs the making of photocopies or other reproductions of copyrighted material.

Under certain conditions specified in the law, libraries and archives are authorized to furnish a photocopy or other reproduction. One of these specified conditions is that the photocopy or reproduction is not to be “used for any purpose other than private study, scholarship, or research.” If a user makes a request for, or later uses, a photocopy or reproduction for purposes in excess of “fair use” that user may be liable for copyright infringement,

This institution reserves the right to refuse to accept a copying order if, in its judgment, fulfillment of the order would involve violation of copyright law.

**Please Note: The author retains the copyright while the New Jersey Institute of Technology reserves the right to distribute this thesis or dissertation**

Printing note: If you do not wish to print this page, then select “Pages from: first page # to: last page #” on the print dialog screen

The Van Houten library has removed some of the personal information and all signatures from the approval page and biographical sketches of theses and dissertations in order to protect the identity of NJIT graduates and faculty.

## ABSTRACT

### ADAPTIVE INTERFERENCE CANCELATION TECHNIQUES FOR MULTICARRIER MODULATED SYSTEMS

by  
Matthijs A. Visser

Current wireline systems and wireless broadcasting systems employ multicarrier modulation (MCM). This includes the high-rate digital subscriber line (HDSL), digital audio broadcasting system (DAB) and the digital terrestrial television broadcasting system (dTTb). Multicarrier modulation is also envisioned for high-speed indoor wireless local area networks (WLAN). Additionally, multicarrier code division multiple access (MC-CDMA), a hybrid of orthogonal frequency division multiplexing (OFDM) and CDMA, is proposed for the downlink (base-to-mobile) of a 3<sup>rd</sup> generation wireless system as part of the IMT-2000 standardization process.

The performance of an MC-CDMA system—similar to a direct sequence CDMA (DS-CDMA) system—is limited by the presence of multiple access interference (MAI). Downlink communications also suffers from MAI as a result of the multipath channel effect, even if it implements orthogonal code multiplexing. Additionally, transmissions aimed at different mobile users may be assigned different powers in order to increase the system capacity, essentially creating a near-far problem for some users.

Due to the MC-CDMA signal structure the conventional decorrelator (based on the inverse of the correlation matrix) is dependent on the channel coefficients, suggesting the use of an adaptive multiuser detector, which can track a time-variant channel. The performance of a blind adaptive multiuser detector for MC-CDMA, based on the “bootstrap algorithm,” is investigated and compared to the performance of the conventional decorrelator. Additionally, the performance is investigated for different channel conditions. First, for a non-faded flat additive white Gaussian

noise (AWGN) channel. Second, for a frequency selective channel with and without correlation between the channel coefficients at the different subcarriers.

In general, the mobile terminal suffers from limited available resources such as computing power or battery life and, therefore, cannot accommodate the same level of receiver complexity as the base station. For the downlink, however, the received signal structure is less complex due to the assumed synchronized transmission. Moreover, the mobile receiver is merely required to detect the desired user's data stream. To reduce the complexity, detectors are proposed that do not require knowledge of the active users nor their respective codes, but rather use a combined code to represent all the interfering users at once. The performance of the reduced complexity conventional decorrelator is compared to the performance of an adaptive reduced complexity detector using the bootstrap algorithm. The performance of these detectors is also investigated for the aforementioned channel types.

For spectral-efficiency, closely spaced subcarriers are used in a multicarrier modulated system. A resulting drawback is a high sensitivity of the performance to a frequency offset. This results from a Doppler shift, due to mobile movement, as well as from a mismatch between the carrier frequencies at the transmitter and receiver. To mitigate this problem an adaptive decorrelator based frequency offset correction scheme is developed for OFDM and its performance is investigated. Additionally, a blind frequency offset estimation and correction structure is proposed based on a stochastic gradient method. The convergence and statistical properties of this estimator are investigated.

A blind adaptive joint multiuser detection and frequency offset correction structure for downlink MC-CDMA is developed. This detector is a combination of the structures for multiuser detection for MC-CDMA and frequency offset correction for OFDM. Moreover, the performance of this detector is investigated and compared to a joint detector based on a minimum mean square error (MMSE) criterion.

**ADAPTIVE INTERFERENCE CANCELATION TECHNIQUES FOR  
MULTICARRIER MODULATED SYSTEMS**

by  
**Matthijs A. Visser**

**A Dissertation  
Submitted to the Faculty of  
New Jersey Institute of Technology  
in Partial Fulfillment of the Requirements for the Degree of  
Doctor of Philosophy**

**Department of Electrical and Computer Engineering**

**May 1999**

Copyright © 1999 by Matthijs A. Visser

ALL RIGHTS RESERVED

## APPROVAL PAGE

### ADAPTIVE INTERFERENCE CANCELATION TECHNIQUES FOR MULTICARRIER MODULATED SYSTEMS

Matthijs A. Visser

---

Dr. Yeheskel Bar-Ness, Dissertation Advisor Distinguished Professor of Electrical and Computer Engineering, NJIT	Date
---	------

---

Dr. Alex Haimovich, Committee Member Associate Professor of Electrical and Computer Engineering, NJIT	Date
--	------

---

Dr. Hongya Ge, Committee Member Assistant Professor of Electrical and Computer Engineering, NJIT	Date
---	------

---

Dr. Michael Porter, Committee Member Professor of Mathematical Sciences, NJIT	Date
--	------

---

Dr. Moe Z. Win, Committee Member Senior Technical Staff Member, AT&T Labs, Red Bank, NJ	Date
--	------

---

Dr. ir. Gerard J.M. Janssen, Committee Member Assistant Professor of Electrical Engineering, Delft University of Technology, Delft, the Netherlands	Date
---	------

## BIOGRAPHICAL SKETCH

**Author:** Matthijs A. Visser  
**Degree:** Doctor of Philosophy in Electrical Engineering  
**Date:** May 1999

### Graduate Education:

- Doctor of Philosophy in Electrical Engineering,  
New Jersey Institute of Technology, Newark, NJ, U.S.A., 1999
- Master of Science in Electrical Engineering,  
Delft University of Technology, Delft, the Netherlands, 1995

### Publications and Presentations:

- M. A. Visser and Y. Bar-Ness,  
“Adaptive Reduced Complexity Multicarrier CDMA (MC-CDMA) Structure for Downlink PCS,” to appear in the *special issue on Multicarrier Spread-Spectrum of the European Transactions on Telecommunications*, 1999.
- M. A. Visser and Y. Bar-Ness,  
“Frequency Offset Correction for OFDM Using a Blind Adaptive Decorrelator in a Time-Variant Selective Rayleigh Fading Channel,” *to be presented at the IEEE Vehicular Technology Conference*, (Houston, TX, U.S.A.), May 1999.
- M. A. Visser and Y. Bar-Ness,  
“Joint Multiuser Detection and Frequency Offset Correction for Downlink MC-CDMA,” *submitted to the IEEE Globecom Conference*, (Rio de Janeiro, Brazil), Dec. 1999.
- M. A. Visser, P. Zong, and Y. Bar-Ness,  
“A novel method for Blind Frequency Offset Correction in an OFDM system,” *Proceedings of the IEEE Personal, Indoor and Mobile Radio Communications Conference*, (Boston, MA, U.S.A.), pp. 816–820, Sept. 1998.
- M. A. Visser and Y. Bar-Ness,  
“OFDM Frequency Offset Correction Using an Adaptive Decorrelator,” *Proceedings of the 32nd Annual Conference on Information Sciences and Systems*, (Princeton, NJ, U.S.A.), pp. 483–488, Mar. 1998.



- M. A. Visser and Y. Bar-Ness,  
“Adaptive Multi-Carrier CDMA (MC-CDMA) Structure for Downlink PCS,”  
*Proceedings of the 9th Tyrrhenian International Workshop on Digital Commu-  
nication*, (Lerici, Italy), Sept. 1997.
- H. Ge, Y. Bar-Ness, and M. A. Visser,  
“Combined Adaptive Interference Cancellation and Bootstrap Separation of  
Dual Polarized Signals,” *Proceedings of the 30th Asilomar Conference on Signal  
Systems and Computers*, (Pacific Grove, CA, U.S.A), pp. 694–698, Nov. 1996.

Aan mijn ouders

To my parents

## ACKNOWLEDGMENT

I would like to express my sincere gratitude to my advisor, Dr. Yeheskel Bar-Ness. His constant encouragement and support have been invaluable during my time at the Center for Communications and Signal Processing Research. Both on a professional and on a personal level he has greatly contributed to my life as a graduate student.

I would also like to express my appreciation to the distinguished members of the dissertation committee: Dr. Alex Haimovich, Dr. Hongya Ge, Dr. Michael Porter, Dr. Moe Z. Win and Dr. ir. Gerard J.M. Janssen. Their valuable discussions and insightful comments have improved the quality of this dissertation.

Many thanks are due to the professors of the ECE department for making my graduate experience intellectually rewarding and for providing me with a strong background in communications and signal processing.

I would also like to thank my colleagues and friends at the CCSPR as well all those involved with the Graduate Student Association for providing me with extra-curricular diversions that have greatly added to the enjoyment of my time at NJIT.

Finally, I sincerely thank my parents for their constant encouragement and belief in my abilities.

## TABLE OF CONTENTS

Chapter	Page
1 INTRODUCTION . . . . .	1
1.1 Wireless Systems . . . . .	1
1.2 Multicarrier Modulation . . . . .	2
1.3 Multicarrier CDMA . . . . .	4
1.4 Multiuser Detection . . . . .	5
1.5 Reduced Complexity Multiuser Detection . . . . .	7
1.6 The Bootstrap Algorithm . . . . .	8
1.7 Frequency Offset Correction . . . . .	9
1.8 Outline . . . . .	11
2 ADAPTIVE MULTIUSER DETECTION FOR MC-CDMA . . . . .	12
2.1 MC-CDMA System Model . . . . .	12
2.2 Multiuser Detection . . . . .	15
2.2.1 Conventional Decorrelator . . . . .	15
2.2.2 Improved Multiuser Detection . . . . .	17
2.2.3 Adaptive Implementation . . . . .	19
2.3 Reduced Complexity Multiuser Detection . . . . .	20
2.3.1 Reduced Complexity Decorrelator . . . . .	21
2.3.2 Adaptive Reduced Complexity Detector . . . . .	22
2.4 Discussion of Results . . . . .	23
2.4.1 General Discussion . . . . .	23
2.4.2 Non-faded AWGN Channel . . . . .	26
2.4.3 I.I.D. Rayleigh Fading Channel . . . . .	30
2.4.4 Correlated Rayleigh Fading Channel . . . . .	40

Chapter	Page
3 FREQUENCY OFFSET CORRECTION FOR OFDM . . . . .	44
3.1 Frequency Offset Correction Using a Blind Adaptive Decorrelator . . .	44
3.1.1 System Model . . . . .	44
3.1.2 Time-Variant Channel . . . . .	46
3.1.3 Channel Amplitude Estimation . . . . .	47
3.1.4 Decorrelator Based Frequency Offset Correction . . . . .	47
3.1.5 Adaptive Implementation . . . . .	50
3.1.6 Discussion of Results . . . . .	51
3.2 Blind Adaptive Frequency Offset Estimation and Correction . . . . .	61
3.2.1 System Model . . . . .	61
3.2.2 Frequency Offset Calculation . . . . .	62
3.2.3 Frequency Offset Estimation . . . . .	64
3.2.4 Adaptive Frequency Offset Control . . . . .	65
3.2.5 Statistical Properties Of The Frequency Offset Estimate . . . .	66
3.2.6 Convergence Criteria . . . . .	68
4 JOINT MULTIUSER DETECTION AND FREQUENCY OFFSET CORRECTION FOR DOWNLINK MC-CDMA . . . . .	72
4.1 System Model . . . . .	72
4.2 Conventional Decorrelator . . . . .	75
4.3 Adaptive Decorrelating Detector . . . . .	76
4.4 Wiener Filter . . . . .	80
4.5 Discussion and Results . . . . .	81
5 CONCLUSIONS . . . . .	86
5.1 Adaptive Multiuser Detection for MC-CDMA . . . . .	86
5.2 Frequency Offset Correction for OFDM . . . . .	89
5.2.1 Frequency Offset Correction Using an Adaptive Decorrelator . .	89
5.2.2 Blind Adaptive Frequency Offset Estimation and Correction . .	90

Chapter	Page
5.3 Joint Multiuser Detection and Frequency Offset Correction for Downlink MC-CDMA .....	91
APPENDIX A CORRELATED RAYLEIGH FADING IN THE FREQUENCY DOMAIN .....	93
APPENDIX B NUMERICAL DETERMINATION OF THE BOOTSTRAP WEIGHTS FOR LOW INTERFERENCE TO SIGNAL RATIOS .....	97
APPENDIX C OUTPUT OF THE DFT IN THE PRESENCE OF A FREQUENCY OFFSET .....	102
APPENDIX D LIST OF SYMBOLS AND ABBREVIATIONS .....	104
REFERENCES .....	110

## LIST OF TABLES

<b>Table</b>		<b>Page</b>
2.1	The various detectors used for performance comparison. . . . .	24
2.2	Parameters for simulation of the ARCD performance in a non-faded AWGN channel. . . . .	27
2.3	Parameters for simulation of the ARCD and AFDD performance in an i.i.d. Rayleigh fading channel. . . . .	31
2.4	Parameters for simulation in a correlated Rayleigh fading channel. . . . .	41

## LIST OF FIGURES

Figure	Page
1.1 OFDM spectrum compared to BPSK spectrum. . . . .	3
1.2 Block diagram of the downlink in an MC-CDMA system. . . . .	6
1.3 Bootstrapped forward-forward structure. . . . .	9
1.4 Carrier to Interference Ratio for conventional OFDM as a function of the normalized frequency offset $\varepsilon$ . . . . .	10
2.1 Adaptive multiuser detector. . . . .	20
2.2 Bootstrap decorrelator with compounded codes. . . . .	22
2.3 Regions for performance comparison of the various detectors. . . . .	25
2.4 BER of the RCD, ARCD(ISR=0 dB), and FDD vs. $K_a$ in a non-faded AWGN channel. . . . .	28
2.5 BER of the ARCD vs. ISR in a non-faded AWGN channel for $K_a = 8$ . . .	29
2.6 BER of the ARCD vs. ISR in a non-faded AWGN channel for $K_a = 29$ . .	29
2.7 BER of the ARCD vs. ISR in a non-faded AWGN channel for $K_a =$ 2, 8, 20, 30. . . . .	30
2.8 BER of the RCD, ARCD(ISR=0 dB), and FDD vs. $K_a$ with EGC in an i.i.d. Rayleigh faded channel. . . . .	35
2.9 BER of the RCD, ARCD(ISR=0 dB), and FDD vs. $K_a$ with MRC in an i.i.d. Rayleigh faded channel. . . . .	35
2.10 BER of the RCD, ARCD(ISR=0 dB), and FDD vs. $K_a$ with EGC and MRC in an i.i.d. Rayleigh faded channel. . . . .	36
2.11 BER of the ARCD and AFDD vs. $K_a$ for ISR=0 dB, with both EGC and MRC in an i.i.d. Rayleigh faded channel. . . . .	36
2.12 BER of the ARCD and AFDD vs. ISR with EGC for $K_a = 8$ in an i.i.d. Rayleigh faded channel. . . . .	37
2.13 BER of the ARCD and AFDD vs. ISR with EGC for $K_a = 20$ in an i.i.d. Rayleigh faded channel. . . . .	37
2.14 BER of the ARCD and AFDD vs. ISR with MRC for $K_a = 8$ in an i.i.d. Rayleigh faded channel. . . . .	38



Figure	Page
2.15 BER of the ARCD and AFDD vs. ISR with MRC for $K_a = 20$ in an i.i.d. Rayleigh faded channel. . . . .	38
2.16 BER of the ARCD vs. ISR with EGC and MRC for $K_a = 2, 8, 20$ in an i.i.d. Rayleigh faded channel. . . . .	39
2.17 BER of the AFDD vs. ISR with EGC and MRC for $K_a = 2, 8, 20$ in an i.i.d. Rayleigh faded channel. . . . .	39
2.18 BER of the RCD, ARCD(ISR=0 dB), and FDD vs. $K_a$ with EGC and MRC in a correlated Rayleigh faded channel. . . . .	42
2.19 BER of the ARCD(ISR=0 dB) vs. $K_a$ with EGC and MRC in both an i.i.d. and correlated Rayleigh fading channel. . . . .	43
2.20 BER of the FDD vs. $K_a$ with EGC and MRC in both an i.i.d. and correlated Rayleigh fading channel. . . . .	43
3.1 Block diagram of an OFDM system with frequency offset correction. . . .	56
3.2 Wittwer's method for generating correlated complex Gaussian samples. . .	56
3.3 Time Correlation Function for $\tau_0 = 1000$ . . . . .	57
3.4 Two stage implementation for adaptive frequency offset correction. . . .	57
3.5 Constellations of 16-QAM transmission for $N_c = 8$ , $\varepsilon = 0.2$ and SNR = 16 dB, (a) transmitted constellation; (b) constellation at output of DFT; (c) constellation after $\mathbf{V}$ ; (d) constellation after $\tilde{\mathbf{V}}$ . . . . .	58
3.6 SINR as a function of the normalized frequency offset $\varepsilon$ for $N_c = 8$ subcarriers, (a) SNR = 0 dB; (b) SNR = 10 dB; (c) SNR = 20 dB . . .	58
3.7 Gain over conventional OFDM as a function of the normalized frequency offset $\varepsilon$ for $N_c = 8$ subcarriers, (a) SNR = 0 dB; (b) SNR = 10 dB; (c) SNR = 20 dB . . . . .	59
3.8 Bit error rate of a 4-QAM transmission versus the SNR, (a) $\varepsilon=0.1$ ; (b) $\varepsilon=0.15$ ; (c) $\varepsilon=0.2$ . . . . .	59
3.9 Performance with the regular bootstrap algorithm. . . . .	60
3.10 Performance with the augmented bootstrap algorithm. . . . .	60
3.11 Block diagram of an OFDM system with adaptive frequency offset correction. . . . .	69
3.12 Ensemble averaged squared error for $N_c = 8$ and SNR = 10 dB. . . . .	69
3.13 Normalized frequency offset estimate $\hat{\varepsilon}$ versus actual normalized frequency offset $\varepsilon$ for $N_c = 8$ and for SNR = 10 dB and SNR = $\infty$ . . . . .	70

Figure	Page
3.14 BPSK constellation for $\varepsilon = 0.2$ and SNR = 10 dB, (a) without frequency offset, (b) without correction, (c) with frequency offset correction . . . .	70
3.15 Variance of $\hat{\Delta}$ versus the SNR for $N_c = 8$ . . . . .	71
4.1 Block diagram of a downlink MC-CDMA system with joint multiuser detection and frequency offset correction . . . . .	82
4.2 Two stage implementation for joint multiuser detection and frequency offset correction . . . . .	83
4.3 Constellations of 4-QAM transmission for $N_c = 7$ , $K_a = 4$ , $\varepsilon = 0.25$ and SNR = 12 dB, (a) transmitted constellation, (b) constellation after $\mathbf{C}^T$ , (c) constellation after $\mathbf{V}$ , (d) constellation after $\tilde{\mathbf{V}}$ . . . . .	83
4.4 BER versus SNR for $N_c = 7$ , $K_a = 4$ , $\varepsilon = 0.2$ and SIR = -10 dB . . . . .	84
4.5 BER versus SNR for $N_c = 7$ , $K_a = 4$ , $\varepsilon = 0.2$ and SIR = 0 dB . . . . .	84
4.6 BER versus SNR for $N_c = 7$ , $K_a = 4$ , $\varepsilon = 0.2$ and SIR = 10 dB . . . . .	85
A.1 Absolute value of the frequency correlation function as a function of $\Delta f$ with $\tau_d$ as a parameter. . . . .	95

# CHAPTER 1

## INTRODUCTION

### 1.1 Wireless Systems

Since the introduction of analog cellular radio systems in the late seventies and early eighties there has been a remarkable increase in the demand for wireless telephony. During this time, a shift took place from a mostly professional use of the wireless systems to a more popular use. With this shift came the consumer's requirement for a higher subjective speech quality, similar to that of wireline systems. Additionally, due to the spectral limitations of wireless transmissions, systems offering a higher spectral efficiency were needed.

The development of digital cellular radio systems introduced both the desired increase in spectral efficiency as well as an improved quality of service (QOS). Moreover, the utilization of digital transmission techniques offered the possibility for many new services. The first digital cellular radio systems —also referred to as second generation wireless systems— such as IS-54 in the U.S.A. or GSM in Europe, were based on time division multiple access (TDMA). In a TDMA system, each user is assigned a so-called time-slot during which its transmission may take place.

In parallel, another digital wireless system, using code division multiple access (CDMA), was developed. In a CDMA system, each active user is assigned a different code or signature sequence. Different CDMA implementations have been described in the literature, such as time hopping (TH), frequency hopping (FH) and direct sequence (DS), differing in their use of the signature sequence [1].

In the U.S.A., IS-95, based on DS-CDMA, has proven to be a popular standard for wireless communication systems. The principle of DS-CDMA is based on the spread spectrum (SS) techniques that were originally developed for military use. In a DS-CDMA system, the user transmits a chip sequence, which is generated by multiplication of its data stream and signature sequence, allowing the users to use

the full available frequency band for the full time period needed for the transmission. In other words, no time or frequency slot structure is imposed.

CDMA has several features which enhance the capacity. First, as no slot structures are imposed, the CDMA system inherently gains from the fact that a user might not need the allocated resources all the time. For instance, it has been shown that in voice communication a user will generate speech slightly more than half of the time. In an FDMA (such as the original analog systems) or TDMA (such as IS-54 or GSM) system, a user would waste approximately half of the allocated frequency or time slots. In a CDMA system, however, the quiet user will not generate interference for the other users in the same cell, hence more active users can be accommodated utilizing the same amount of resources. Additionally, a wideband system such as DS-SS, in combination with a RAKE receiver, has inherent frequency diversity, which improves the performance with respect to a narrowband system at the expense of an increased transmission bandwidth and complexity [2].

## 1.2 Multicarrier Modulation

The principle of transmitting data using multiple orthogonal carriers has been established some time ago [3, 4, 5]. In [6] it was recognized that the discrete Fourier transform (DFT) could serve as an efficient modulation and demodulation technique for a multicarrier system, resulting in the orthogonal frequency division multiplexing (OFDM) system. A multicarrier system has two major advantages over a single carrier system: (1) reduced noise enhancement as a result of linear equalization; (2) increased immunity to impulse noise due to the increased symbol time. In addition, a reduction or elimination of inter-symbol interference (ISI) is possible with the use of an appropriate guard-time or cyclic prefix. Moreover, due to the overlapping spectra of the subcarriers a multicarrier system can achieve a higher bandwidth efficiency than a single carrier system [7, 8], as is also depicted in figure 1.1.

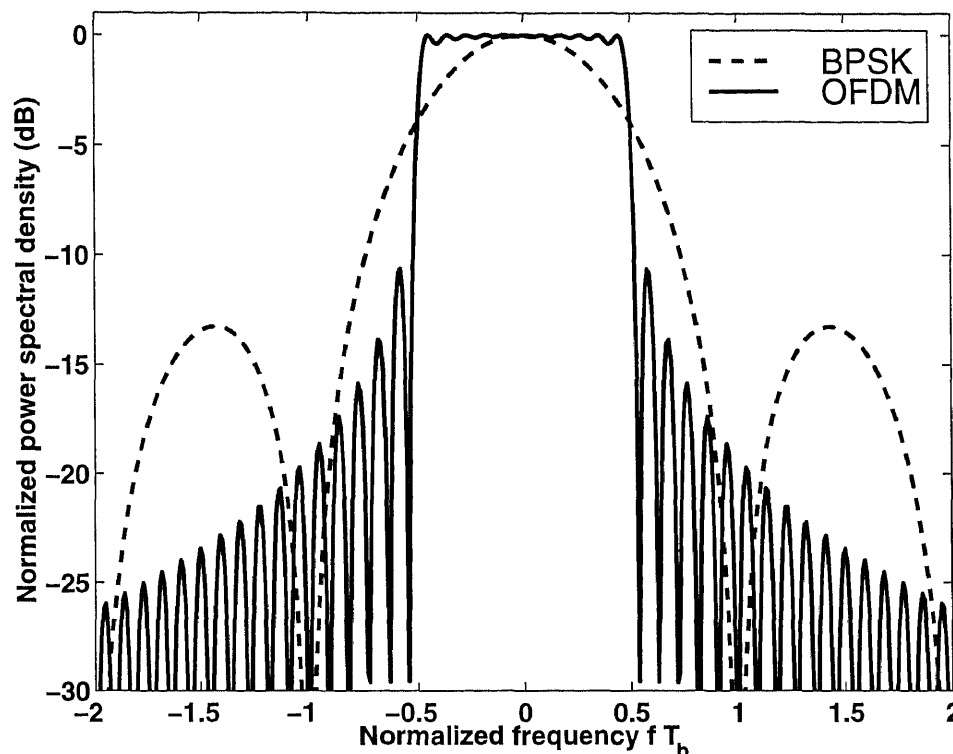


Figure 1.1 OFDM spectrum compared to BPSK spectrum.

Multicarrier based communication systems find broad application in wireline as well as wireless environments. For wireline, multicarrier communications, research has been driven by users' rapidly increasing bandwidth demands for emerging multimedia based services. These high bandwidth applications have led to the development of the spectrally efficient high-rate digital subscriber line (HDSL), which employs multicarrier modulation (MCM). Until now, most wireless, multicarrier based systems have been developed for broadcasting, such as digital audio broadcasting (DAB) and digital terrestrial television broadcasting (dTTb) [7, 9, 10, 11]. In [12] high-speed indoor wireless communication based on multicarrier modulation is described.

Future wireless personal communication systems (PCS) will also require high bandwidth since the multimedia services, currently only available through wireline

connections, will be offered by wireless service providers. Hence the interest in wideband wireless communications in general. Recently, the use of multicarrier techniques for wireless PCS has been considered in the IMT-2000 (third generation mobile communications systems) standardization process [13]. In December 1997, the TIA TR45.5 committee adopted the framework for Wideband cdmaOne, a wideband CDMA standard backward compatible with IS-95. One of the main differences between Wideband cdmaOne in the U.S. and WCDMA in Europe and Japan is the downlink channel structure. Both systems support direct spread with higher spreading factors. The former, however, also supports a multicarrier downlink transmission, resulting in a multicarrier code division multiple access (MC-CDMA) structure. This proposed MC-CDMA implementation uses three carriers, where each carrier is spread as in the original IS-95 system.

### 1.3 Multicarrier CDMA

Different forms of MC-CDMA have been described by various authors [2, 14, 15, 16, 17]. For instance, Vandendorpe [17] describes a system which is a hybrid of OFDM and DS-SS. In this dissertation, however, the MC-CDMA system as described by Yee, Linnartz and Fettweis [14] is employed, in which each user bit is transmitted simultaneously over multiple subcarriers without any spreading per subcarrier. The resultant signal is a composition of multiple narrowband signals at different frequencies, spaced regularly in the frequency domain. As a result, it provides resistance against frequency selective fading due to the fact that each subcarrier will be narrowband with respect to the coherence bandwidth of the channel [6, 7, 8]. In comparison with wideband transmission based on the DS-SS techniques, the multicarrier transmission will not need to employ the complex RAKE receiver as each subcarrier is essentially subject to flat fading.

A block diagram of the downlink in an MC-CDMA system is shown in figure 1.2. In such an MC-CDMA system multiple access is achieved by assigning a 0 or  $\pi$  degrees phase shift offset to each subcarrier for each user. The sequence of offsets assigned to each user forms a unique orthogonal or pseudo-orthogonal signature sequence, such as Hadamard, Gold or Kasami code sequences. Here,  $c_k(m)$ ,  $m = 1, \dots, N_c$  is the signature sequence of user  $k$ ,  $k = 1, \dots, K_a$ . When the subcarriers are separated by  $1/T_b$ , where  $T_b$  denotes the bit duration, the multicarrier modulators and demodulators can be replaced by an inverse discrete Fourier transform (IDFT) and a discrete Fourier transform respectively.

#### 1.4 Multiuser Detection

The performance of an MC-CDMA system —similar to a DS-CDMA system— is limited by the presence of multiple access interference (MAI). As a result of the multipath channel effect downlink (base-to-mobile) communications also suffers from MAI, even if it implements orthogonal code multiplexing. Additionally, to increase system capacity, transmissions aimed at different mobile users may be assigned different powers, essentially creating a near-far problem for some users. Hence, it is judicious to use a so-called 'near-far resistant' (multiuser) detector to improve the performance of the desired user.

The optimal near-far resistant detector performs much better than the conventional matched filter (MF) detector at the expense of a complexity that is exponential in the number of users [18]. A sub-optimal detector, called decorrelating detector, that is linear (in operation as well as in complexity) was presented in [19] and [20]. Adaptive decorrelating detectors based on the bootstrap algorithm [21], have been applied to the CDMA system in various operating scenarios [22, 23, 24]. Some work on the application of the bootstrap algorithm to MC-CDMA has been reported in [25, 26]. These adaptive bootstrap based detectors have been shown to achieve

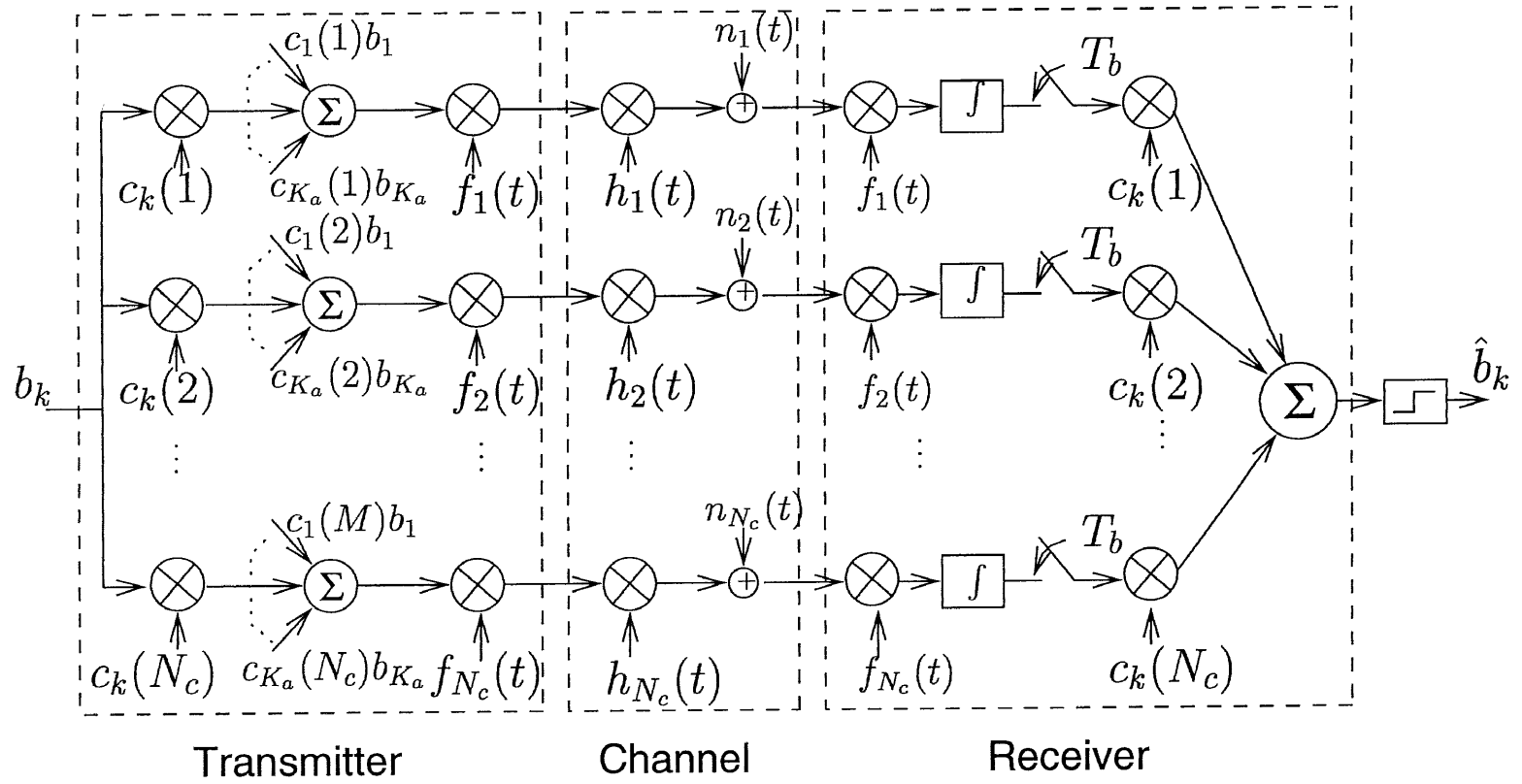


Figure 1.2 Block diagram of the downlink in an MC-CDMA system.



single-user performance, i.e. outperform the fixed decorrelators, in the case of low interference power, while achieving equal performance in the case of high interference power; as such they behave similar to MMSE based detectors [27, 28]. Another sub-optimal near-far resistant detector, with a multistage detector (a cancellation stage follows the decorrelation stage), was proposed by Varanasi [29]. With this detector, however, the cancellation stage requires the knowledge of the received signal energies. An adaptive multistage detector, as described in [30], does not suffer from this limitation. Additionally, all the aforementioned detectors require the knowledge of which users are active in order to utilize their particular codes.

### 1.5 Reduced Complexity Multiuser Detection

In general, the mobile terminal suffers from limited available resources such as computing power and battery life and can, therefore, not accommodate the same level of receiver complexity as the base station. However, for the downlink, the received signal structure is less complex due to the assumed synchronized transmission. Moreover, the mobile receiver is merely required to detect the desired user's data stream. Hence, it is both essential and realizable to develop a receiver for use in the mobile terminal with a lower complexity than the ones currently proposed for the uplink. In [31], a simplified adaptive decorrelator was developed by concentrating only on the correlation of the desired user with the other users and ignoring the correlations between the other users. This detector, however, still requires knowledge of the active users and their codes. In [32, 33], detectors were proposed that do not require knowledge of which users are active and their respective codes, but rather use a combined code to represent all the interfering users at once.

## 1.6 The Bootstrap Algorithm

The bootstrap algorithm is based on a cross-coupled structure that provides signal enhancement for both the desired signal and the interference samples. The cross-coupling is such that the output of one canceler is used to improve the output of the other. Therefore, this structure can operate independently, hence the name “bootstrap.” Also, this structure is often referred to as a signal separator rather than an interference canceler as both outputs produce “cleaned” samples.

The application of the bootstrap algorithm to an interference cancelation problem was first proposed in [34]. The algorithm has also been successfully applied to cross-polarization cancelation for satellite communications [35] and in a microwave terrestrial radio link [36].

Three different structures for bootstrapped operation with different criteria for adaptation, have been described: the backward-backward (BB) structure which uses a minimum power criterion, the forward-forward (FF) structure which uses a correlation criterion and the forward-backward (FB) structure which is a combination of the BB and FF. In figure 1.3 the FF structure is shown for a two-input/two-output configuration.

In order for the bootstrap algorithm to converge to the steady-state, a so-called discriminator is needed. In a digital implementation of the bootstrap structure, this discriminator can be implemented using a hard-limiter. The function of the discriminator is to emphasize the undesired component relative to the desired component. It can be seen from figure 1.3 that without the discriminators the controls for both weights are identical. To control  $w_{21}$  a sample of  $y_2$ , which contains  $y_1$  as interference, is correlated with  $\hat{b}_1$ . However,  $\hat{b}_1$  should equal  $b_1$  to generate the proper feedback. A similar explanation holds for the control of  $w_{12}$ . Initially, both  $\hat{b}_1$  and  $\hat{b}_2$  contain interference, so neither weight is controlled properly. However, when one processor cancels some interference it results in a cleaner sample for the other processor and

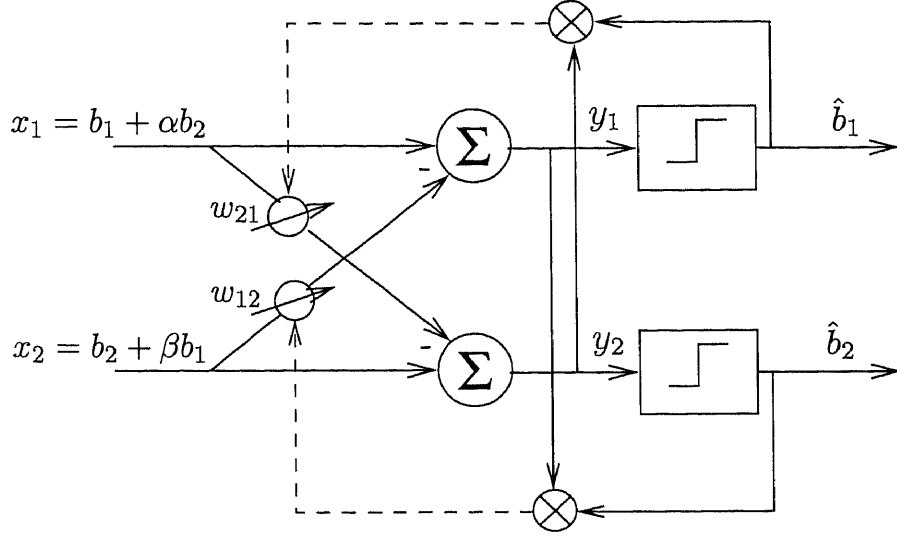


**Figure 1.3** Bootstrapped forward-forward structure.

vice versa. This is the essence of the so-called bootstrapping operation that can perform blind signal separation [37, 38].

### 1.7 Frequency Offset Correction

For spectral-efficiency reasons, closely spaced subcarriers are used in a multicarrier modulated system. A resulting drawback is a high sensitivity of the performance to a frequency offset (FO), which results from a Doppler shift, due to mobile movement, as well as from a mismatch between the carrier frequencies at the transmitter and receiver [39, 40]. This is illustrated in figure 1.4 by the decrease in carrier-to-interference ratio (CIR) as a function of the normalized frequency offset, which is the absolute frequency offset as a percentage of the subcarrier spacing. For example, a CIR greater than 20 dB requires the normalized frequency offset to be less than 7%. To illustrate the strictness of this requirement, notice that for a subcarrier spacing of 10 kHz and a carrier frequency of 1 GHz, the oscillator stability must be better than 0.7 ppm, which exceeds today's specifications.

As a consequence of the frequency offset, the subcarriers' orthogonality is lost, causing inter-carrier interference (ICI). In addition, the constellation of the desired signal at each subcarrier is rotated. This in turn results in inter-rail interference between the I- and Q-rails, which further reduces the carrier-to-interference ratio.

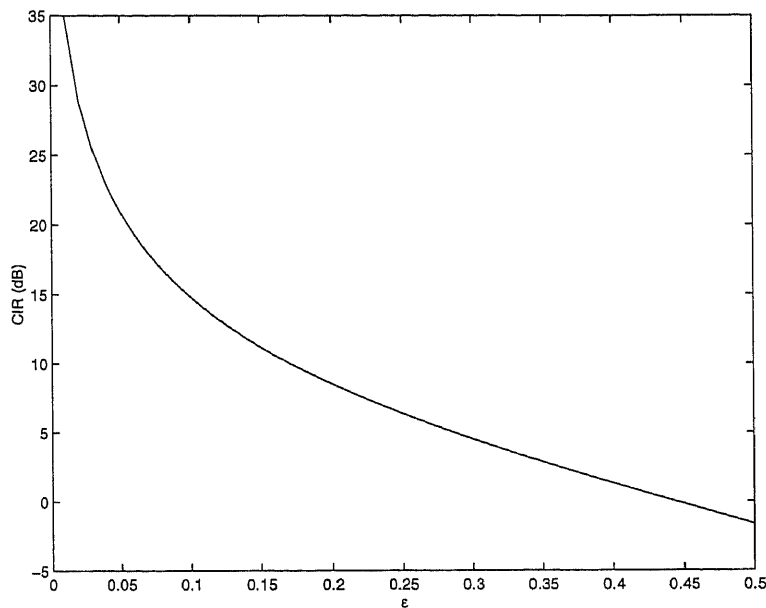


**Figure 1.4** Carrier to Interference Ratio for conventional OFDM as a function of the normalized frequency offset  $\epsilon$ .

A method for estimating the frequency offset based on the retransmission of an information symbol, thus reducing the channel throughput, is presented in [41]. Another method, proposed in [40], merely mitigates the effect of the ICI instead of completely correcting for the frequency offset. This scheme is based on a form of repetition coding in the frequency domain, hence also suffers from a reduction in bandwidth efficiency. A method using frequency domain correlative coding, which does not reduce the bandwidth efficiency, was developed in [42].

On the other hand, as the ICI can also be regarded as correlation between the different subcarriers, an adaptive decorrelator may be applied to compensate for the negative effect of a frequency offset.

## 1.8 Outline

In chapter 2, multiuser detection for MC-CDMA is addressed. The conventional decorrelator (based on the inverse of the correlation matrix) is derived and it is shown that for MC-CDMA this detector is dependent on the channel coefficients. Then, an adaptive signal separator, for multiuser detection, based on the bootstrap algorithm is developed. Following this, a reduced complexity detector for operation in a downlink scenario is developed. Both the conventional reduced complexity decorrelator and the adaptive reduced complexity detector are examined and compared with the full-dimensional detectors.

Chapter 3 treats the issue of frequency offset correction for OFDM. As the presence of a frequency offset leads to inter-carrier-interference, an adaptive interference cancelation structure to combat the effects of the frequency offset is suggested. The adaptive structure is based on the bootstrap algorithm acting as a signal separator for the different subcarriers. Also, another structure, based on blind adaptive frequency offset estimation and correction is proposed.

A joint multiuser detection and frequency offset correction scheme for downlink MC-CDMA is proposed in chapter 4. This detector combines the work on multiuser detection (chapter 2) and frequency offset correction (chapter 3).

Finally, conclusions are presented in chapter 5.

## CHAPTER 2

### ADAPTIVE MULTIUSER DETECTION FOR MC-CDMA

#### 2.1 MC-CDMA System Model

A downlink MC-CDMA system with  $N_c$  subcarriers and  $K_a$  active users ( $K_a \leq K$ , the maximum number of users) is considered (see also figure 1.2). Multiple access is achieved by assigning a signature sequence from a set of Gold<sup>1</sup> code sequences of length  $N_c$  to each user. Each element (chip) of this sequence together with the user's information bit (added modulo 2) is BPSK modulated on a subcarrier. The use of Gold codes of length  $N_c$  results in a maximum of  $N_c + 2$  different codes [43].

The transmitted signal during the  $i^{\text{th}}$  bit interval ( $(i-1)T_b < t \leq iT_b$ ) at subcarrier  $m$ ,  $m \in 1, 2, \dots, N_c$ , may be described as

$$\begin{aligned} s_m(t) &= \sum_{k=1}^{K_a} c_k(m) \sqrt{p_k} b_k(i) \sqrt{2} p(t) \cos \left[ 2\pi \left( f_c + F \frac{m-1}{T_b} \right) t \right] \\ &= \sum_{k=1}^{K_a} c_k(m) \sqrt{p_k} b_k(i) \phi_m(t), \end{aligned} \quad (2.1)$$

where  $p(t) = \frac{1}{\sqrt{T_b}} \Pi(\frac{t}{T_b})$  is a normalized rectangular pulse shape,  $b_k = \pm 1$  is the information bit of user  $k$  in the  $i^{\text{th}}$  bit interval,  $p_k$  is the power of user  $k$ ,  $c_k(m) = \pm \frac{1}{\sqrt{N_c}}$ ,  $m = 1, \dots, N_c$ , is the signature code sequence of the  $k^{\text{th}}$  user and  $F$  is a dimensionless system parameter that determines the spacing of the subcarriers by an integer multiple of the inverse of the bit time. Additionally, the orthonormal basis function  $\phi_m(t)$ , associated with subcarrier  $m$ , is defined as:

$$\phi_m(t) = \sqrt{\frac{2}{T_b}} \Pi(\frac{t}{T_b}) \cos \left[ 2\pi \left( f_c + F \frac{m-1}{T_b} \right) t \right], \quad (2.2)$$

such that

$$\int_{(i-1)T_b}^{iT_b} \phi_m(t) \phi_n(t) dt = \begin{cases} 1, & m = n \\ 0, & m \neq n. \end{cases} \quad (2.3)$$

---

<sup>1</sup>The performance of different code sequences, such as Gold, Walsh-Hadamard or Kasami, will be very similar as the frequency selective channel reduces the (pseudo-) orthogonality of these code sequences.

It is assumed that the subcarrier bandwidth,  $B_s$ , is sufficiently small, such that the inter-symbol interference (ISI) is negligible and no guard-interval is needed. Additionally, as a consequence of the downlink transmission, the amplitude and phase distortion at each subcarrier will be the same for all users' signals, as shown in figure 1.2. Hence, the complex transfer function for all users at subcarrier  $m$  is described by

$$h_m = a_m e^{j\theta_m}, \quad (2.4)$$

where  $a_m$  is the amplitude distortion, and  $\theta_m$  the phase distortion, are random variables (r.v.) that have a Rayleigh distribution and a uniform distribution in the interval  $[-\pi, \pi)$ , respectively. The correlation between the random variables  $h_{m1}$  and  $h_{m2}$  is given by the spaced-frequency correlation function (a derivation is given in appendix A):

$$\rho(\Delta f) = \frac{1 - j2\pi\tau_d\Delta f}{1 + (2\pi\tau_d\Delta f)^2}, \quad (2.5)$$

where  $\tau_d$  is the rms channel delay spread and  $\Delta f$  is the frequency separation of subcarriers  $m1$  and  $m2$ :

$$\Delta f = \frac{(m1 - m2)F}{T_b}. \quad (2.6)$$

Taking into account the effect of the channel as well as the additive noise the expression for the signal of subcarrier  $m$  at the input of the receiver during the  $i^{\text{th}}$  bit interval follows:

$$r_m(t) = h_m s_m(t) + n_m(t), \quad (2.7)$$

where  $n_m(t)$  denotes the additive white Gaussian noise process.

The received signal  $r_m(t)$  is processed by a coherent (matched filter) detector and it is assumed that the orthogonality of the subcarriers is still intact after transmission through the channel.<sup>2</sup> The output of the detector for subcarrier  $m$ , sampled

---

<sup>2</sup>This assumption indicates that no significant frequency offset exists, either as a result of a Doppler shift due to mobile movement or as a result of a carrier synchronization error in the receiver.

at time  $iT_b$  is

$$\begin{aligned} z_m(i) &= \int_{(i-1)T_b}^{iT_b} r_m(t) \phi_m(t) e^{-j\theta_m} dt \\ &= a_m \sum_{k=1}^{K_a} c_k(m) \sqrt{p_k} b_k(i) + n_m(i). \end{aligned} \quad (2.8)$$

Combining the  $N_c$  subcarrier outputs,  $z_m$ , into a vector  $\mathbf{z}$  and dropping the time index  $i$ , it follows that:

$$\mathbf{z} = \mathbf{A} \mathbf{C} \sqrt{\mathbf{P}} \mathbf{b} + \mathbf{n}, \quad (2.9)$$

where  $\mathbf{P} = \text{diag}\{p_1, \dots, p_{K_a}\}$  is a  $K_a \times K_a$  diagonal matrix that accounts for the possibility of transmitting to different users with different powers. The matrix  $\mathbf{A} = \text{diag}\{a_1, \dots, a_{N_c}\}$  is an  $N_c \times N_c$  diagonal matrix and  $\mathbf{n}$  is a vector of length  $N_c$  containing independent identically distributed (i.i.d.) zero-mean Gaussian noise samples with covariance matrix

$$\mathbf{R}_n = E[\mathbf{n}\mathbf{n}^T] = \sigma_n^2 \mathbf{I}_{N_c}, \quad (2.10)$$

where  $E$  is the expectation operator,  $\sigma_n^2$  is the power of the additive noise and  $\mathbf{I}_{N_c}$  is the  $N_c \times N_c$  identity matrix. Additionally, the  $N_c \times K_a$  code matrix  $\mathbf{C}$  is defined as

$$\mathbf{C} = [\mathbf{c}_1, \mathbf{c}_2, \dots, \mathbf{c}_{K_a}], \quad (2.11)$$

where  $\mathbf{c}_k = [c_k(1), c_k(2), \dots, c_k(N_c)]^T$ ,  $T$  denoting the transpose operator.

The output of the receiver can be multiplied with either  $\mathbf{c}_k$ , to get the decision variable using conventional single user detection (SUD) for user  $k$ , or with the complete code matrix  $\mathbf{C}$ , to generate decision variables for all users such that multiuser detection (MUD) can be applied. Multiplication with  $\mathbf{C}$  results in

$$\mathbf{x} = \mathbf{C}^T \mathbf{z} = \mathbf{C}^T \mathbf{A} \mathbf{C} \sqrt{\mathbf{P}} \mathbf{b} + \boldsymbol{\eta} = \mathbf{P}'_c \sqrt{\mathbf{P}} \mathbf{b} + \boldsymbol{\eta}, \quad (2.12)$$

where the conditional (on  $\mathbf{A}$ ) code cross-correlation matrix  $\mathbf{P}'_c$  is defined as

$$\mathbf{P}'_c = \mathbf{C}^T \mathbf{A} \mathbf{C}, \quad (2.13)$$



and  $\boldsymbol{\eta} = \mathbf{C}^T \mathbf{n}$  is a zero mean Gaussian noise vector with covariance matrix

$$\mathbf{R}_{\boldsymbol{\eta}} = E[\boldsymbol{\eta}\boldsymbol{\eta}^T] = \mathbf{C}^T E[\mathbf{n}\mathbf{n}^T] \mathbf{C} = \sigma_n^2 \mathbf{P}_c, \quad (2.14)$$

where  $\mathbf{P}_c = \mathbf{C}^T \mathbf{C}$  is the code cross-correlation matrix. Each element of  $\mathbf{P}_c$  gives the cross-correlation between two signature code sequences:  $\mathbf{P}_c(i, j) = \mathbf{c}_i^T \mathbf{c}_j$ .

As the magnitude of all code elements is equal ( $|c_k(m)| = 1/\sqrt{N_c}$ ), the expression in equation (2.12) can be viewed as equal gain combining (EGC) of the signals on the different subcarriers. It is well known, however, that the combiner that achieves the best performance in the presence of additive noise only is the maximal ratio combiner (MRC) [2], which weights each subcarrier by the channel gain on that subcarrier:

$$\begin{aligned} \mathbf{x}_{\text{MRC}} &= \mathbf{C}^T \mathbf{A} \mathbf{z} = \mathbf{C}^T \mathbf{A}^2 \mathbf{C} \sqrt{\mathbf{P}} \mathbf{b} + \boldsymbol{\eta}_{\text{MRC}} \\ &= \mathbf{P}_c'' \sqrt{\mathbf{P}} \mathbf{b} + \boldsymbol{\eta}_{\text{MRC}}, \end{aligned} \quad (2.15)$$

where  $\mathbf{P}_c'' = \mathbf{C}^T \mathbf{A}^2 \mathbf{C}$  is the conditional code cross-correlation matrix for MRC and  $\boldsymbol{\eta}_{\text{MRC}} = \mathbf{C}^T \mathbf{A} \mathbf{n}$  is a zero-mean Gaussian noise vector with covariance matrix

$$\begin{aligned} \mathbf{R}_{\boldsymbol{\eta}_{\text{MRC}}} &= E[\boldsymbol{\eta}_{\text{MRC}} \boldsymbol{\eta}_{\text{MRC}}^T | \mathbf{A}] = \mathbf{C}^T \mathbf{A} E[\mathbf{n}\mathbf{n}^T] \mathbf{A} \mathbf{C} \\ &= \sigma_n^2 \mathbf{C}^T \mathbf{A}^2 \mathbf{C} = \sigma_n^2 \mathbf{P}_c''. \end{aligned} \quad (2.16)$$

## 2.2 Multiuser Detection

### 2.2.1 Conventional Decorrelator

Equation (2.12), implies that the signals of the different users are correlated due to the presence of MAI. In the case of a DS-CDMA system the so-called *conventional decorrelator* uses the inverse of the code cross-correlation matrix  $\mathbf{P}_c$  to separate the signals [19]. In an MC-CDMA system with a non-faded AWGN channel ( $\mathbf{A} = \mathbf{I}$ ) the inverse of the code cross-correlation matrix can also be used to completely separate

the users' signals as shown by

$$\mathbf{y} = \mathbf{P}_c^{-1} \mathbf{x} = \mathbf{P}_c^{-1} \mathbf{C}^T \mathbf{C} \sqrt{\mathbf{P}} \mathbf{b} + \mathbf{P}_c^{-1} \boldsymbol{\eta} = \sqrt{\mathbf{P}} \mathbf{b} + \boldsymbol{\xi}, \quad (2.17)$$

where  $\boldsymbol{\xi} = \mathbf{P}_c^{-1} \boldsymbol{\eta}$  is a zero-mean Gaussian noise vector with covariance

$$\mathbf{R}_\xi = E [\boldsymbol{\xi} \boldsymbol{\xi}^T] = \sigma_n^2 \mathbf{P}_c^{-1}. \quad (2.18)$$

This detector is near-far resistant as the performance of one user does not depend on the power of the interfering users. In the case of a multipath fading channel, however, the inverse of the code cross-correlation matrix no longer separates the signals as  $\mathbf{A} \neq \mathbf{I}$ . Now, the inverse of the conditional code cross-correlation matrix  $\mathbf{P}'_c$  is defined as the *conventional decorrelator*<sup>3</sup> for MC-CDMA, which completely separates the different users' signals:

$$\mathbf{y} = \mathbf{P}'_c^{-1} \mathbf{x} = \mathbf{P}'_c^{-1} \mathbf{C}^T \mathbf{A} \mathbf{C} \sqrt{\mathbf{P}} \mathbf{b} + \mathbf{P}'_c^{-1} \boldsymbol{\eta} = \sqrt{\mathbf{P}} \mathbf{b} + \boldsymbol{\xi}', \quad (2.19)$$

where  $\boldsymbol{\xi}' = \mathbf{P}'_c^{-1} \boldsymbol{\eta}$  is a zero-mean Gaussian noise vector with covariance

$$\mathbf{R}_{\xi'} = E [\boldsymbol{\xi}' \boldsymbol{\xi}'^T] = \sigma_n^2 \mathbf{P}'_c^{-1} \mathbf{P}_c \mathbf{P}'_c^{-1}. \quad (2.20)$$

Due to the signal structure of MC-CDMA, the conventional decorrelator has become dependent on the channel parameters, indicating that an adaptive approach might be preferable, because it may track changes in the channel.

When MRC is employed, the transformation that separates the users' signals is the inverse of  $\mathbf{P}''_c$ :

$$\mathbf{y}_{\text{MRC}} = \mathbf{P}''_c^{-1} \mathbf{x}_{\text{MRC}} = \mathbf{P}''_c^{-1} \mathbf{C}^T \mathbf{A}^2 \mathbf{C} \sqrt{\mathbf{P}} \mathbf{b} + \mathbf{P}''_c^{-1} \boldsymbol{\eta}_{\text{MRC}} = \sqrt{\mathbf{P}} \mathbf{b} + \boldsymbol{\xi}'', \quad (2.21)$$

where  $\boldsymbol{\xi}'' = \mathbf{P}''_c^{-1} \boldsymbol{\eta}_{\text{MRC}}$  is a zero-mean Gaussian noise vector with covariance

$$\mathbf{R}_{\xi''} = E [\boldsymbol{\xi}'' \boldsymbol{\xi}''^T] = \sigma_n^2 \mathbf{P}''_c^{-1} \mathbf{P}_c \mathbf{P}''_c^{-1}. \quad (2.22)$$

---

<sup>3</sup>This detector will also be referred to as the full dimensional decorrelator (FDD), to emphasize the difference with the reduced complexity decorrelator, to be proposed in the next section.

### 2.2.2 Improved Multiuser Detection

In [22] an adaptive multiuser detector was proposed for DS-CDMA that does not totally separate the users' signals, but leaves some interference residue in the output. This detector has the advantage that the additive noise is less enhanced than with the conventional decorrelator, resulting in a better output signal-to-interference-plus-noise (SINR) ratio, particularly when the interference power is low.<sup>4</sup> The application of this detector to MC-CDMA has also been studied in [25, 26].

The improved performance was achieved by using a matrix  $\mathbf{V}$  to separate the signals, while  $\mathbf{V} \neq \mathbf{P}'_c^{-1}$ . It was proposed to use  $\mathbf{V} = \mathbf{I} - \mathbf{W}$ , where

$$\mathbf{W} = \begin{bmatrix} 0 & w_{21} & w_{31} & \dots & w_{K_a 1} \\ w_{12} & 0 & w_{32} & \dots & w_{K_a 2} \\ \vdots & & \ddots & & \vdots \\ \vdots & & & 0 & w_{K_a, K_a-1} \\ w_{1K_a} & \dots & w_{K_a-1, K_a} & & 0 \end{bmatrix}. \quad (2.23)$$

Using this  $\mathbf{V}$  and the expression for  $\mathbf{x}$  from equation (2.12) the following output of the decorrelator follows:

$$\mathbf{y} = \mathbf{V}^T \mathbf{x} = \mathbf{x} - \mathbf{W}^T \mathbf{x}. \quad (2.24)$$

The vector  $\mathbf{x}$ —the output of the detector after multiplication with the codes—exclusive of the additive noise component (see also equation (2.12)), can be rewritten for user number one ( $k = 1$ )<sup>5</sup>:

$$\mathbf{x} = \begin{bmatrix} x_1 \\ \mathbf{x}_1 \end{bmatrix} = \begin{bmatrix} \mathbf{c}_1^T \mathbf{A} \mathbf{c}_1 & \mathbf{c}_1^T \mathbf{A} \mathbf{C}_1 \\ \mathbf{C}_1^T \mathbf{A} \mathbf{c}_1 & \mathbf{C}_1^T \mathbf{A} \mathbf{C}_1 \end{bmatrix} \sqrt{\mathbf{P}} \mathbf{b}, \quad (2.25)$$

where  $\mathbf{x}_1$  is  $\mathbf{x}$  without  $x_1$ , the first element of  $\mathbf{x}$  and  $\mathbf{C}_1$  is the matrix  $\mathbf{C}$  without its first column, thus  $\mathbf{C} = \begin{bmatrix} \mathbf{c}_1 & \mathbf{C}_1 \end{bmatrix}$ .

---

<sup>4</sup>This improvement in performance is due to the fact that this detector inherently uses knowledge about the signal powers, while the conventional decorrelator does not.

<sup>5</sup>This is without loss of generality for any  $k$ .

In order to separate the different users' signals and to motivate the adaptive control of  $\mathbf{W}$  it has been proposed in [22] to choose the matrix  $\mathbf{W}$  such that

$$E[y_k \mathbf{b}_k] = \mathbf{0}, \quad (2.26)$$

where  $\mathbf{b}_k$  is  $\mathbf{b}$  without the  $k^{\text{th}}$  element and  $\mathbf{0}$  is a vector of length  $K_a - 1$  with all elements equal to zero. If the SINR at any decorrelator output ( $j \neq k$ ) is sufficiently high then  $E[y_k \hat{b}_j] \simeq E[y_k b_j (1 - P_{e_j})]$ . The condition in equation (2.26) may then be interpreted as an approximation to  $E[y_k \hat{\mathbf{b}}_k] = \mathbf{0}$  where  $\hat{\mathbf{b}}_k = \text{sgn}(\mathbf{y}_k)$  is the estimate of  $\mathbf{b}_k$ . Assuming the condition on the SINR is met, equation (2.26) is expanded with the use of equation (2.25) for  $k = 1$  as follows<sup>6</sup>:

$$\begin{aligned} E[y_1 \mathbf{b}_1] &= E[x_1 \mathbf{b}_1 - \mathbf{w}_1^T \mathbf{x}_1 \mathbf{b}_1] \\ &= E \left[ \left( \mathbf{c}_1^T \mathbf{A} \mathbf{c}_1 \sqrt{p_1} b_1 + \mathbf{c}_1^T \mathbf{A} \mathbf{C}_1 \sqrt{\mathbf{P}_1} \mathbf{b}_1 \right) \mathbf{b}_1 \right. \\ &\quad \left. - \mathbf{w}_1^T \left( \mathbf{C}_1^T \mathbf{A} \mathbf{c}_1 \sqrt{p_1} b_1 + \mathbf{C}_1^T \mathbf{A} \mathbf{C}_1 \sqrt{\mathbf{P}_1} \mathbf{b}_1 \right) \mathbf{b}_1 \right] \\ &= \sqrt{\mathbf{P}_1} \mathbf{C}_1^T \mathbf{A} \mathbf{c}_1 - \sqrt{\mathbf{P}_1} \mathbf{C}_1^T \mathbf{A} \mathbf{C}_1 \mathbf{w}_1 = \mathbf{0}, \end{aligned} \quad (2.27)$$

where  $\mathbf{P}_1$  is the matrix  $\mathbf{P}$  without the first row and column, and  $\mathbf{w}_1$  is the first column of  $\mathbf{W}$  without its first element. To evaluate the expectation operation the assumption that the information sequences of the different users are uncorrelated was used.

From equation (2.27) the solution for the so-called *decorrelating weights*,  $\mathbf{w}_1$  or, in general,  $\mathbf{w}_k$ , can be found in the limit, i.e for very strong interference or a high interference-to-signal ratio (ISR):

$$\mathbf{w}_k = \left( \mathbf{C}_k^T \mathbf{A} \mathbf{C}_k \right)^{-1} \mathbf{C}_k^T \mathbf{A} \mathbf{c}_k = \mathbf{P}'_{c_k}{}^{-1} \boldsymbol{\rho}'_k, \quad (2.28)$$

where  $\mathbf{P}'_{c_k} = \left( \mathbf{C}_k^T \mathbf{A} \mathbf{C}_k \right)$ , which is  $\mathbf{P}'_c$  without the  $k^{\text{th}}$  row and column and  $\boldsymbol{\rho}'_k$  is the  $k^{\text{th}}$  column of  $\mathbf{P}'_c$  without the  $k^{\text{th}}$  element. As expected, with the *decorrelating*

---

<sup>6</sup>In the case when  $\mathbf{A}$  is random, i.e. a fading channel, the expectation in equation (2.27) is conditional on  $\mathbf{A}$ .

*weights*, the performance of the conventional decorrelating detector is attained. The ISR is defined as the ratio of any of the interfering users and the desired user's signal power. Assuming the first user is the desired one ( $k = 1$ ) the ISR is defined as:

$$\text{ISR} = \frac{p_i}{p_1}, \quad i = 2, \dots, K_a. \quad (2.29)$$

Similar to EGC, the decorrelating weights in the case of MRC can be derived:

$$\mathbf{w}_{k\text{MRC}} = \left( \mathbf{C}_k^T \mathbf{A}^2 \mathbf{C}_k \right)^{-1} \mathbf{C}_k^T \mathbf{A}^2 \mathbf{c}_k = \mathbf{P}_{c_k}''^{-1} \boldsymbol{\rho}_k'', \quad (2.30)$$

where  $\mathbf{P}_{c_k}''$  is  $\mathbf{P}_c''$  without the  $k^{\text{th}}$  row and column and  $\boldsymbol{\rho}_k''$  is the  $k^{\text{th}}$  column of  $\mathbf{P}_c''$  without the  $k^{\text{th}}$  element.

### 2.2.3 Adaptive Implementation

As in a DS-CDMA system [22], rather than using the decorrelating weights, an adaptive scheme for improved performance, particularly in the region of low ISR, can be used. This adaptive implementation will be referred to as the adaptive full dimensional detector (AFDD). The adaptive scheme implements the so-called bootstrap algorithm [22], which recursively updates the elements of the weight matrix  $\mathbf{W}$  as follows:

$$\mathbf{w}_k(i+1) = \mathbf{w}_k(i) + \mu y_k \text{sgn}(\mathbf{y}_k), \quad (2.31)$$

where  $\mu$  is the step-size parameter of the adaptation process. The operation of the adaptive algorithm is shown graphically in figure 2.1. An analytical solution for the weights in the case of low ISR cannot be found due to the nonlinear nature of the control. However, in the next section the reduced complexity receiver is presented for which a numerical solution is derived in appendix B. Note that the algorithm presented in equation (2.31) can be used for EGC as well as for MRC.

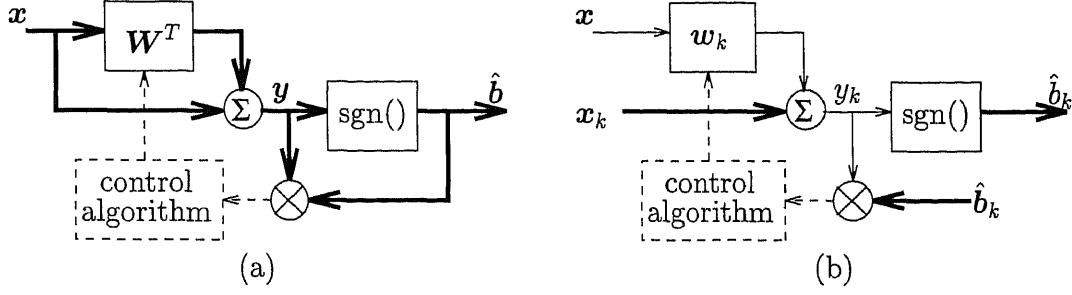


**Figure 2.1** (a) Adaptive multiuser detector; (b) detail for  $k^{\text{th}}$  user.

### 2.3 Reduced Complexity Multiuser Detection

For a large number of users the complexity of the full decorrelator will become prohibitively large as the complexity increases with the number of users. Additionally, the required knowledge about the interfering users — which users are active, their powers and their codes — might inhibit application of the multiuser detector. To reduce the complexity and to alleviate these requirements it is proposed to use a ‘compounded’ signature code that represents *all* the possible interfering users. In this way, only the code of the desired user and this compounded code are remaining. As a result, the size of the weight matrix for the decorrelator is reduced from  $K_a \times K_a$  to  $2 \times 2$ . Additionally, this significantly reduces the number of adaptively controlled weights of an adaptive implementation.

The codes of all the possible interfering users can be compounded as follows:

$$\mathbf{c}_k^{c^T} = \boldsymbol{\alpha}^T \mathbf{C}_{K_k}^T, \quad (2.32)$$

where  $\boldsymbol{\alpha}$  is a  $K-1 \times 1$  vector that compounds the codes of all the possible interfering users and  $\mathbf{C}_{K_k}$  is an  $N_c \times K-1$  matrix containing all  $K$  users’ signature codes except the code of user  $k$  (the desired user).

The output of the detector after multiplication with the code of the desired user and the compounded code can be expressed as

$$\mathbf{x} = \begin{bmatrix} x_k \\ x_k^c \end{bmatrix} = \begin{bmatrix} \mathbf{c}_k^T \\ \mathbf{c}_k^{c^T} \end{bmatrix} \mathbf{z} = \mathbf{C}_k^{c^T} \mathbf{z} = \mathbf{C}_k^{c^T} \mathbf{A} \mathbf{C} \sqrt{\mathbf{P}} \mathbf{b} + \boldsymbol{\zeta}, \quad (2.33)$$

where  $\mathbf{C}_k^c = [\mathbf{c}_k, \mathbf{c}_k^c]$ ,  $\mathbf{z}$  is the output of the coherent detector previously defined in equation (2.9) and  $\boldsymbol{\zeta} = \mathbf{C}_k^{c^T} \mathbf{n}$  is a zero-mean Gaussian noise vector with covariance matrix

$$\mathbf{R}_\zeta = E[\boldsymbol{\zeta} \boldsymbol{\zeta}^T] = \mathbf{C}_k^{c^T} E[\mathbf{n} \mathbf{n}^T] \mathbf{C}_k^c = \sigma_n^2 \mathbf{C}_k^{c^T} \mathbf{C}_k^c. \quad (2.34)$$

Maximal ratio combining can also be applied in the case of the reduced complexity receiver leading to the following output of the detector:

$$\mathbf{x}_{\text{MRC}} = \mathbf{C}_k^{c^T} \mathbf{A}^2 \mathbf{C} \sqrt{\mathbf{P}} \mathbf{b} + \boldsymbol{\zeta}_{\text{MRC}}, \quad (2.35)$$

where  $\boldsymbol{\zeta} = \mathbf{C}_k^{c^T} \mathbf{A} \mathbf{n}$  is a zero-mean Gaussian noise vector with covariance matrix

$$\mathbf{R}_\zeta = E[\boldsymbol{\zeta} \boldsymbol{\zeta}^T | \mathbf{A}] = \mathbf{C}_k^{c^T} \mathbf{A} E[\mathbf{n} \mathbf{n}^T] \mathbf{A} \mathbf{C}_k^c = \sigma_n^2 \mathbf{C}_k^{c^T} \mathbf{A}^2 \mathbf{C}_k^c. \quad (2.36)$$

### 2.3.1 Reduced Complexity Decorrelator

The multiuser interference is cancelled in the desired output by the use of the  $2 \times 2$  bootstrap algorithm, shown in figure 2.2. To find  $\boldsymbol{\alpha}$  it is assumed<sup>7</sup> that  $w_{12} = 1$ , and  $K_a = K$ , i.e. the maximum number of users is active and consequently  $\mathbf{C} = \mathbf{C}_K$ . The vector  $\boldsymbol{\alpha}$  that totally cancels the multiuser interference can be derived as follows:

$$\begin{aligned} y_k &= x_k - x_k^c = \mathbf{c}_k^T \mathbf{A} \mathbf{C}_K \sqrt{\mathbf{P}} \mathbf{b} - \mathbf{c}_k^{c^T} \mathbf{A} \mathbf{C}_K \sqrt{\mathbf{P}} \mathbf{b} + \mathbf{c}_k^T \mathbf{n} - \mathbf{c}_k^{c^T} \mathbf{n} \\ &= [\mathbf{c}_k^T \mathbf{A} \mathbf{c}_k - \boldsymbol{\alpha}^T \mathbf{C}_{K_k}^T \mathbf{A} \mathbf{c}_k] \sqrt{p_k} b_k \\ &\quad + [\mathbf{c}_k^T \mathbf{A} \mathbf{C}_{K_k} - \boldsymbol{\alpha}^T \mathbf{C}_{K_k}^T \mathbf{A} \mathbf{C}_{K_k}] \sqrt{\mathbf{P}_k} \mathbf{b}_k + \xi_k^c, \end{aligned} \quad (2.37)$$

where  $\xi_k^c = \mathbf{c}_k^T \mathbf{n} - \mathbf{c}_k^{c^T} \mathbf{n}$  is the additive Gaussian noise term. From equation (2.37) it can be seen that the second term of the right hand side has to be equated to zero in order to totally cancel the interference. Consequently:

$$\boldsymbol{\alpha} = (\mathbf{C}_{K_k}^T \mathbf{A} \mathbf{C}_{K_k})^{-1} \mathbf{C}_{K_k}^T \mathbf{A} \mathbf{c}_k. \quad (2.38)$$

---

<sup>7</sup>This is similar to using a conventional decorrelator and will henceforth be referred to as the reduced complexity decorrelator (RCD)

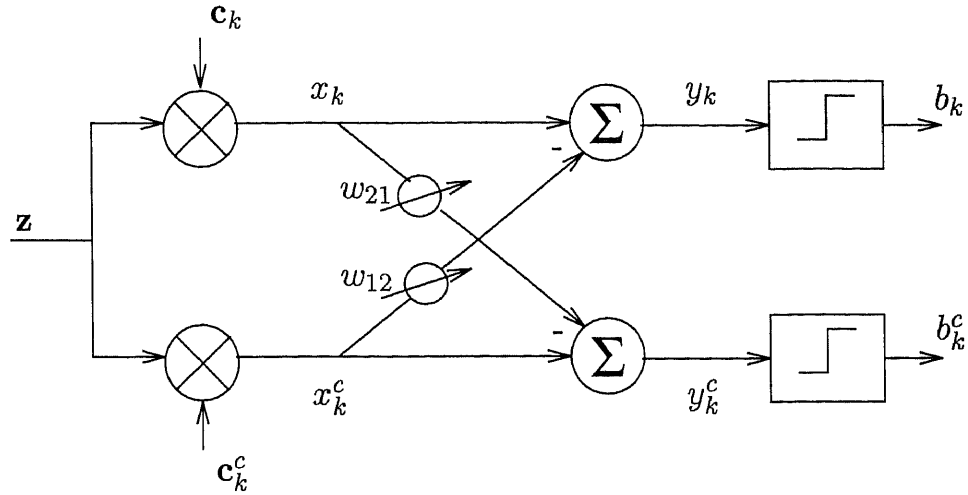


**Figure 2.2** Bootstrap decorrelator with compounded codes.

As expected, when  $K_a = K$ , the solution for  $\alpha$  is equal to  $\mathbf{w}_k$  of the regular decorrelator shown in equation (2.28). In other words, when the maximum number of users ( $K$ ) is active, all the multiuser interference will be cancelled and the performance will equal that of the full dimensional decorrelator. However, when  $K_a < K$  users are active there will be a mismatch in cancelling the interference, because  $\alpha$  was calculated based on  $K$  active users. This residual interference will be reduced with the adaptive implementation of this detector, the ARCD.

Similar to EGC,  $\alpha_{\text{MRC}}$  can be computed when MRC is used:

$$\alpha_{\text{MRC}} = \left( \mathbf{C}_{K_k}^T \mathbf{A}^2 \mathbf{C}_{K_k} \right)^{-1} \mathbf{C}_{K_k}^T \mathbf{A}^2 \mathbf{c}_k. \quad (2.39)$$

### 2.3.2 Adaptive Reduced Complexity Detector

As in the case of the adaptive full dimensional detector of section 2.2 the adaptive scheme depicted in figure 2.1 will be used to implement the adaptive reduced complexity detector, rather than using the decorrelating weights. In the case of the compounded codes, however, the weight matrix  $\mathbf{W}$  is reduced to a  $2 \times 2$  matrix:

$$\mathbf{W} = \begin{bmatrix} 0 & w_{21} \\ w_{12} & 0 \end{bmatrix}. \quad (2.40)$$



The weight update equation for this  $\mathbf{W}$  is the same as previously expressed in equation (2.31). Also, the solutions for the weights in the case of high ISR can be derived analogously to the derivation in section 2.2. In appendix B a numerical solution for the weights in the case of low ISR is derived.

## 2.4 Discussion of Results

### 2.4.1 General Discussion

In this section, numerical results of the bit error rates (BER) of the ARCD are presented. As explained in the preceding sections, the term reduced complexity refers to the fact that the  $K_a$  matched filters of the full dimensional multiuser detector have been replaced by 2 matched filters. The performance of the ARCD is compared to the performance of the RCD, the conventional decorrelator, also called the FDD, and the AFDD. Additionally, the performance is compared to the single user bound (SUB)<sup>8</sup>, and the SUD, also called the conventional matched filter detector, which simply multiplies with  $\mathbf{c}_k$ , the code of the desired user. An overview of these detectors is given in table 2.4.1. Moreover, results for both equal gain combining (EGC) and maximal ratio combining (MRC) have been obtained. In addition, the results have been obtained for a non-faded additive white Gaussian noise channel, and a frequency-selective Rayleigh fading channel, with and without correlation between the fading parameters at the different subcarriers.

A performance comparison between the ARCD and the AFDD can be related to three regions of the interference-to-signal ratio (ISR) as shown in figure 2.3. The ISR is defined as the ratio of the desired user's power and any interfering user's power, assuming all the interfering users have equal power. In the first region, a scenario with very weak interfering users is assumed and in the limit for this region ( $\text{ISR} \rightarrow -\infty$ ), both detectors perform similarly. In the second region, where the interfering users are

---

<sup>8</sup>For the SUB it is assumed that only one user is present and one filter matched to the desired code is used, i.e. there is no interference.

**Table 2.1** The various detectors used for performance comparison.

Detector Type	Transformation	Size
Full Dimensional Decorrelator (FDD)	$\mathbf{P}_c'^{-1}$	$K_a \times K_a$
Adaptive Full Dimensional Detector (AFDD)	$\mathbf{V}$	$K_a \times K_a$
Reduced Complexity Decorrelator (RCD)	$w_{12} = 1$	$2 \times 2$
Adaptive Reduced Complexity Detector (ARCD)	$\mathbf{V}$	$2 \times 2$
Single User Detector (SUD)	None	N/A

neither very weak nor very strong, the performance will be illustrated and compared using equal strength desired user and interferers (ISR=0 dB). The performance for ISR=0 dB is indicative of a downlink scenario without power control. In the third region, very strong interfering users are assumed and in the limit for this region (ISR  $\rightarrow \infty$ ), the adaptive weights of both detectors approach their respective decorrelating weights as was shown in the preceding sections. Consequently, the performance of the ARCD and AFDD approaches the performance of the RCD and FDD respectively, hence this performance may be seen as the asymptotic performance of the adaptive detectors. Both the RCD and FDD are near-far resistant, i.e. their performances are independent of the ISR. Nevertheless, the following results will show that the adaptive bootstrap detector always outperforms the corresponding non-adaptive decorrelator, establishing the decorrelator performance as a bound for the performance. Even though the performance of the adaptive detectors is dependent on the ISR they will be referred to as near-far resistant as their performance is bounded by the performance of the near-far resistant decorrelators.

In the low ISR region, with multiple users present, an adaptive reduced complexity bootstrap detector may be applied, in combination with either EGC or MRC. For Rayleigh fading channels, surprising as it may seem, the application of this algorithm with EGC, results in a BER lower than the SUB or conventional

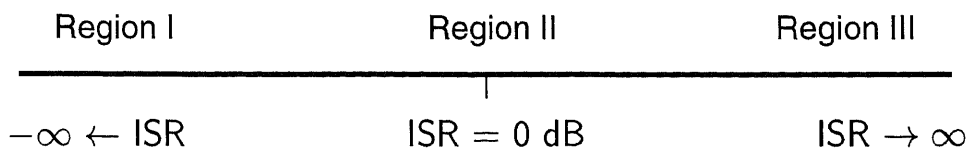


**Figure 2.3** Regions for performance comparison of the various detectors.

detector with EGC. This effect has been shown by simulation as well as by analysis in combination with a numerical method, and is depicted in the appropriate figures with 'ARCD Weak Int. Bound' as a legend.

In the case of the ARCD<sup>9</sup>, for a frequency selective channel and in the absence of interference ( $\text{ISR} = -\infty$ ), the desired signal is present at the desired matched filter output as well as the other matched filter output, because the two code sequences are not orthogonal. However, each matched filter output has a different SNR, demonstrating the possibility for improved performance when the outputs are appropriately combined. Now, the aforementioned observed effect might be explained by viewing the bootstrap algorithm as a combiner that weights these different matched filter outputs relative to their SNR. Alternatively, the bootstrap algorithm may be viewed jointly with the matched filters as a combiner of the different subcarrier signals that have different SNRs due to the frequency selectivity of the channel.

As expected, in the low ISR region, the ARCD in combination with MRC does not improve the performance over the SUB or SUD with MRC, because MRC maximizes the signal-to-noise ratio (SNR) in the presence of only additive white Gaussian noise.

In order to utilize the reduced complexity detector an acceptable choice for  $K$ , the maximum number of users allowed to operate in the system, needs to be determined. Heuristically, it has been established that if the maximum number of

---

<sup>9</sup>This discussion also holds for the AFDD, but with more degrees of freedom (see also the figures in section 2.4.3).

interfering users is even and the elements in  $\alpha$  are all equal (as will be the case for an AWGN channel) then at least half of the elements of  $\mathbf{c}^c$  are zero. Therefore, it is preferred to use an odd maximum number of interfering users ( $K - 1$ ) whose codes will be compounded, hence an even number for the maximum number of users ( $K$ ) will be selected.

#### 2.4.2 Non-faded AWGN Channel

Simulations for the non-faded AWGN channel have been carried out with the following parameters:  $N_c = 31$  subcarriers, the SNR of the desired user is 7 dB, the maximum number of users,  $K = 30$ . The performances of the SUB, FDD, RCD and the bootstrap algorithm in the low ISR region, have been determined numerically by the application of the Q-function, which describes the area under the tail of the Gaussian probability density function (pdf):

$$Q(x) = \frac{1}{\sqrt{2\pi}} \int_x^\infty e^{-t^2/2} dt \quad (2.41)$$

All other BER curves have been obtained by bit error counting over  $10^5$  bits in the steady state of the adaptive algorithm. The step-size parameter,  $\mu$ , of the bootstrap algorithm has been set to  $\mu = 0.5 \times 10^{-3}$ . Additionally, the local mean signal-to-noise-ratio (LSNR) of the desired user is 7 dB. The LSNR is defined as the average SNR, averaged over the probability density function of the channel amplitudes. These parameters are summarized in table 2.4.2.

In figure 2.4 the BER of the desired user as a function of the number of active users  $K_a$  for a non-faded AWGN channel is shown. It is clear that for a non-faded AWGN channel the performance with MRC will be the same as the performance with EGC, hence only the results for EGC are shown. The figure shows that the performance of the RCD, i.e. with  $w_{12} = 1$ , is independent of the number of active users, since  $\alpha$  does not depend on the number of active users (see equation (2.38)) and hence the same compounded code is used for all  $K_a$ . Comparing the performance

**Table 2.2** Parameters for simulation of the ARCD performance in a non-faded AWGN channel.

Parameter	Value
$N_c$	31
$K$	30
LSNR	7 dB
$N_b$	$10^5$
$\mu$	$0.5 \times 10^{-3}$

of the RCD with the FDD, the trade-off between complexity and performance is clear. However, the loss in performance, as a result of the reduction in complexity, decreases with an increasing number of active users as the performance of the FDD worsens, approaching the performance of the RCD. The RCD and FDD have equal performance when the maximum number of users is active, i.e.  $K_a = K$ . Thus, when the system is heavily loaded the knowledge of the actual active users and their respective codes does not provide additional performance improvement. When using equal strength desired user and interferers (ISR=0 dB), the figure shows a large improvement in performance of the ARCD over the RCD and only a moderate loss with respect to the FDD up to  $K_a = 24$ . For  $K_a > 24$  and with ISR = 0 dB, the ARCD outperforms both the RCD and FDD. Note that the performance of the RCD as well as the FDD is independent of the ISR, while the performance of the ARCD is dependent on the ISR (see also figure 2.7). This figure also shows that the performance of the ARCD is the same as that of the SUD, which is equal to the SUB, for very weak interferers in a non-faded AWGN channel.

Figures 2.5 and 2.6 show a comparison between the ARCD, the RCD and the FDD, which is the bound for the AFDD, as a function of the ISR. From these two figures the behavior of the ARCD as a function of the ISR is clearly displayed. For

low ISR levels the performance of the ARCD approaches the SUB, while for high ISR levels it approaches the RCD's performance. As the FDD performs better than the RCD for  $K_a < K$ , there is an ISR level above which the ARCD performs worse than the FDD. This ISR level increases with increasing  $K_a$  as the performance of the FDD approaches the performance of the RCD.

Figure 2.7 shows the performance of the bootstrap decorrelator with compounded codes in an AWGN channel as a function of the ISR with the number of active users  $K_a$  as a parameter. These results indicate that the performance of the ARCD is always better than the performance of the RCD. It is clear from the figure that even with a fully loaded system,  $K_a = K = 30$ , and for  $\text{ISR} = 10$  dB the bit error rate of the ARCD is below that of the RCD. For weak interferers a significant improvement can be noted as the performance approaches the single user bound.

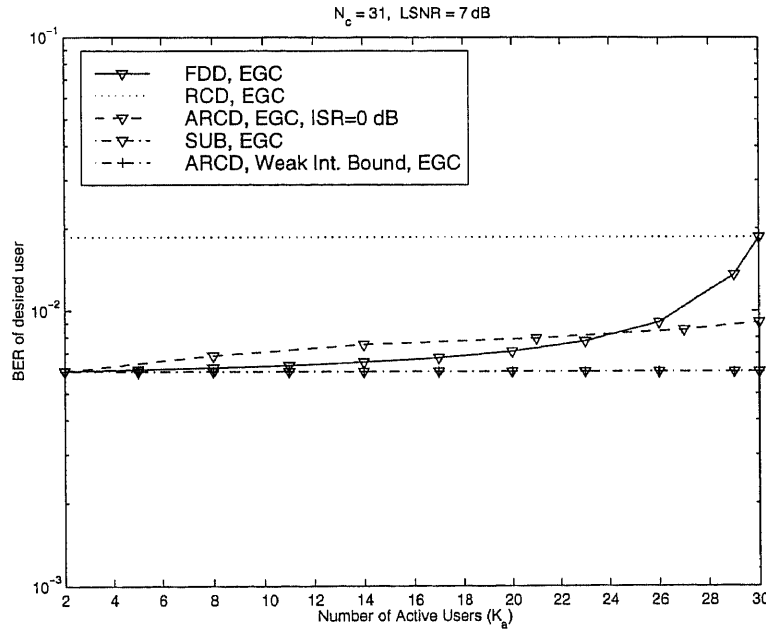


**Figure 2.4** BER of the RCD, ARCD(ISR=0 dB), and FDD vs.  $K_a$  in a non-faded AWGN channel.

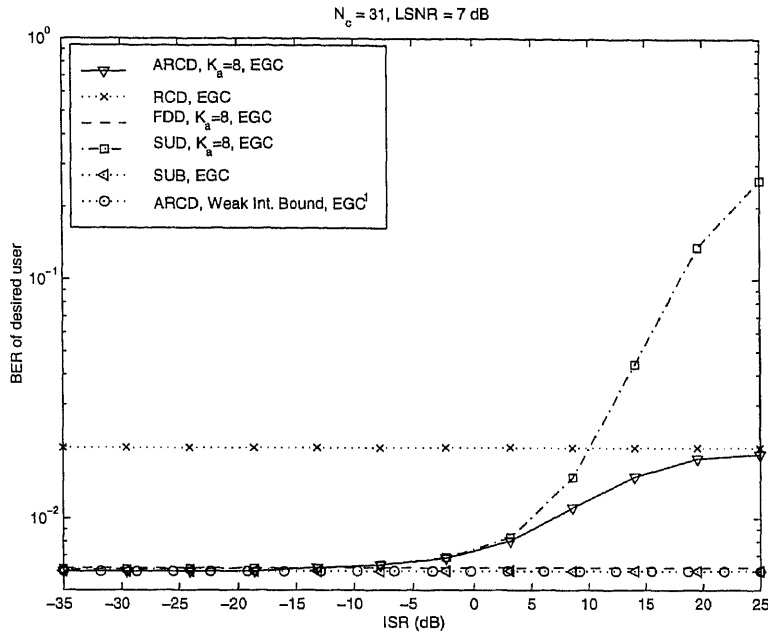


Figure 2.5 BER of the ARCD vs. ISR in a non-faded AWGN channel for  $K_a = 8$ .

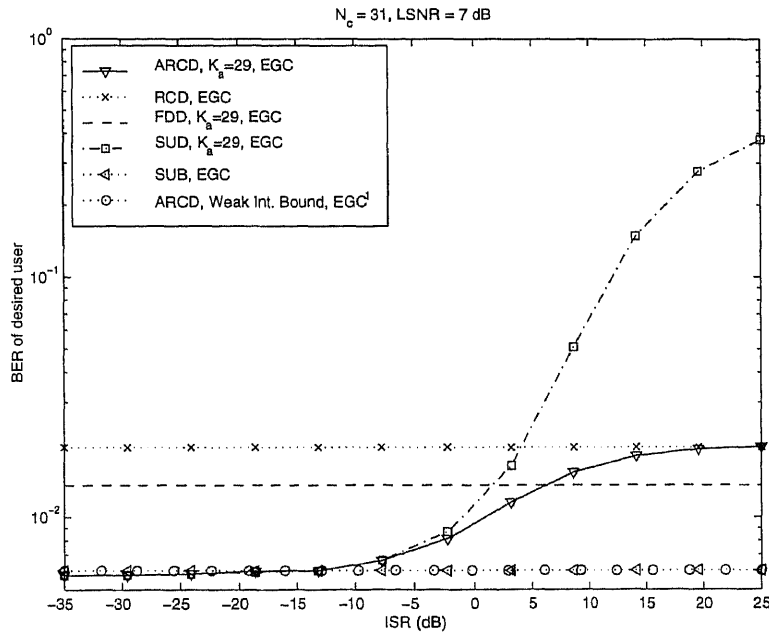
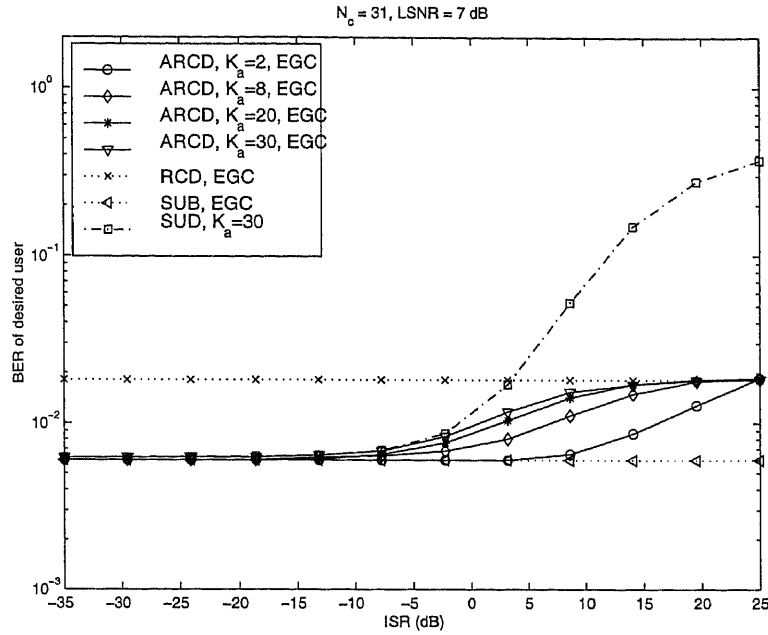


Figure 2.6 BER of the ARCD vs. ISR in a non-faded AWGN channel for  $K_a = 29$ .



**Figure 2.7** BER of the ARCD vs. ISR in a non-faded AWGN channel for  $K_a = 2, 8, 20, 30$ .

### 2.4.3 I.I.D. Rayleigh Fading Channel

In this subsection independent identically distributed (i.i.d) frequency flat Rayleigh fading per subcarrier is assumed. This is characteristic of a system with a subcarrier spacing greater than or equal to the coherence bandwidth. The Rayleigh fading alters the favorable, near-orthogonal, cross-correlation properties of the different users' codes, see also equation (2.13), resulting in a loss of performance with respect to the AWGN channel.

Simulations for the i.i.d. Rayleigh fading channel have been carried out with the following parameters:  $N_c = 31$  subcarriers, the LSNR of the desired user is 7 dB, the maximum number of users,  $K = 30$ . The performances of the SUB, FDD, RCD and the bootstrap algorithm in the low ISR region, have been determined numerically by the application of the Q-function. The BER curves of the ARCD and AFDD have been obtained by bit error counting over  $10^5$  and  $5 \times 10^5$  bits respectively, in



the steady state of the adaptive algorithm. Since the BER is dependent on the channel realization, average BER curves are shown, where the averaging is indicated by the number of Monte-Carlo runs ( $N_{mc}$ ). Hence, for each Monte-Carlo run the conditional BER is obtained by bit error counting over  $10^5$  or  $5 \times 10^5$  bits. The adaptive bootstrap algorithm is used with step-size parameter  $\mu = 0.5 \times 10^{-3}$  for the ARCD. In case of the AFDD, different values for the step-size parameter  $\mu$ , from  $\mu = 0.125 \times 10^{-5}$  to  $\mu = 0.4 \times 10^{-4}$ , are used for different values of the ISR, where the larger  $\mu$  is used for the smaller ISR. These parameters are summarized in table 2.4.3.

**Table 2.3** Parameters for simulation of the ARCD and AFDD performance in an i.i.d. Rayleigh fading channel.

Parameter	Value
$N_c$	31
$K$	30
LSNR	7 dB
$N_b$ (ARCD)	$10^5$
$N_b$ (AFDD)	$5 \times 10^5$
$\mu$ (ARCD)	$0.5 \times 10^{-3}$
$\mu$ (AFDD)	$0.125 \times 10^{-5} \sim 0.4 \times 10^{-4}$
$N_{mc}$	100 or 250

Figure 2.8 shows that the RCD and the FDD have equal performance when the maximum number of users is active, i.e.  $K_a = K$ , the same as for the non-faded AWGN channel. However, for  $K_a < K$ , especially when  $K_a$  is small, the RCD has a significant performance loss relative to the FDD, prompting the application of the ARCD. For ISR=0 dB with EGC, the ARCD almost always performs equal or better than the FDD. This figure also indicates an improved performance over the single user bound when using the bootstrap algorithm in the case of weak interferers. The reason for this effect was explained in section 2.4.1. Comparing figure 2.8 with

figure 2.4, it can be seen that for the i.i.d. Rayleigh fading channel the BER level of the ARCD with EGC is higher and also increases more rapidly as a function of  $K_a$  than for the AWGN channel, due to the reduced code orthogonality as a result of the Rayleigh fading.

Figure 2.9 shows the same set of curves as in figure 2.8 except for the use of MRC instead of EGC. Again, the ARCD at  $\text{ISR}=0$  dB performs better than the RCD. Now, however, the adaptive detector at  $\text{ISR}=0$  dB performs almost always worse than the FDD. As was suggested in section 2.4.1 it can be seen that with MRC, the ARCD with low ISR has the same performance as the SUD with MRC. Comparing figure 2.9 with figure 2.4, shows that the BER of the ARCD with a low number of active users is almost the same for both channel types. However, the BER increases more rapidly with increasing  $K_a$  for the i.i.d. Rayleigh fading channel than for the AWGN channel, due to the reduced code orthogonality as a result of the Rayleigh fading.

In figure 2.10, the two previous figures are combined to compare the performance of the ARCD with EGC and MRC. Most notably, this figure shows that the performance of the ARCD at  $\text{ISR}=0$  dB with EGC is almost always better than with MRC. This can be attributed to the fact that MRC ignores the presence of multiuser interference and thus, for a certain interference level, decreases rather than increases the SINR. Also, the figure shows that both the RCD and the FDD perform better with MRC than with EGC, albeit very slightly in the case of the RCD. Additionally, for both EGC and MRC the additional performance loss of an added user decreases as the number of active users increases. In other words, for a highly loaded system a varying number of active users does not greatly influence the BER of the desired user.

Figure 2.11 shows a performance comparison of the ARCD and AFDD when  $\text{ISR}=0$  dB. The performance of the AFDD with MRC is always better than with

EGC. On the other hand, the performance of the ARCD with EGC is almost always better than with MRC. This can be attributed to the fact that MRC ignores the presence of multiuser interference and thus, for a certain interference level, decreases rather than increases the SINR. Moreover, it is inferred that due to the reduced complexity the ARCD does not have sufficient degrees of freedom to eliminate the increased MUI, whereas the AFDD does.

Figures 2.12 and 2.13 compare the BER of the ARCD and AFDD with EGC for  $K_a = 8$  and  $K_a = 20$  respectively. For  $K_a = 20$  and low ISR<sup>10</sup>, the ARCD performs better than the SUD, and the AFDD performs better than the ARCD, because the AFDD has more degrees of freedom. Recall, however, that the calculation of the SUB assumes the use of only the conventional SUD with EGC. Additionally, for  $K_a = 20$  the AFDD performs at least as good as the ARCD over the full ISR range. This clearly indicates a possible trade-off between performance and complexity. For  $K_a = 8$ , however, there exists a small region where the ARCD slightly outperforms the AFDD. Moreover, for  $K_a = 8$  and low ISR, the ARCD and AFDD have similar performance, even though the AFDD has more degrees of freedom.

Figures 2.12 and 2.13 also show that with EGC the ARCD always outperforms the SUD and the RCD, by which it is bounded. When the adaptive ARCD is compared to the non-adaptive FDD, there exists an ISR level below which the ARCD performs better than the FDD. The ISR level at the cross-over point depends on the number of active users,  $K_a$ , and increases when  $K_a$  increases. This can also be verified from figure 2.10 by realizing that when a maximum number of users is active ( $K_a = K$ ) the full dimensional and reduced complexity decorrelators perform the same.

---

<sup>10</sup>The value of the BER for the ARCD is also determined numerically according to appendix B and the line representing this BER in the figure is a bound and does not represent a function of the ISR.

Figures 2.14 and 2.15 compare the BER of the ARCD and AFDD with MRC for  $K_a = 8$  and  $K_a = 20$  respectively. As expected, for both  $K_a = 8$  and  $K_a = 20$  in the low ISR region the BER of the ARCD, AFDD and SUD are equal to the SUB. The figures also show that the numerically determined bound for ARCD is equal to the SUB as well. Additionally, these two figures show that the AFDD always outperforms the ARCD. Also, for both  $K_a = 8$  and  $K_a = 20$  the AFDD performs at least as good as the ARCD for all ISRs, again indicating the possible trade-off between performance and complexity.

In figure 2.16, the performance of the ARCD is compared for three different numbers of active users with both EGC and MRC. From this figure it can be noted that MRC performs better than EGC when the strength of the interferers is sufficiently low. The ISR level above which MRC performs worse than EGC decreases as the number of active users and/or their interference levels increases. Thus, whether EGC or MRC will perform better depends on the total multiuser interference level observed by the receiver. However, for very strong interferers, MRC performs slightly better than EGC as indicated by the performance curves of the reduced complexity decorrelator.

In figure 2.17, the performance of the AFDD is compared for three different numbers of active users with both EGC and MRC. This figure shows that the AFDD with MRC always outperforms the AFDD with EGC. Moreover, the figure shows that for EGC the size of the AFDD, which depends on  $K_a$ , has an opposite effects for low and high ISRs. For low ISR, the performance is better when  $K_a$  is higher as it has more degrees of freedom to enhance the performance as discussed in 2.4.1. However, for high ISR, the higher  $K_a$  results in more noise amplification as the weights have converged to the decorrelating weights, resulting in similar performance as the FDD. The dependence of the FDD on  $K_a$  has been shown before in figure 2.8.

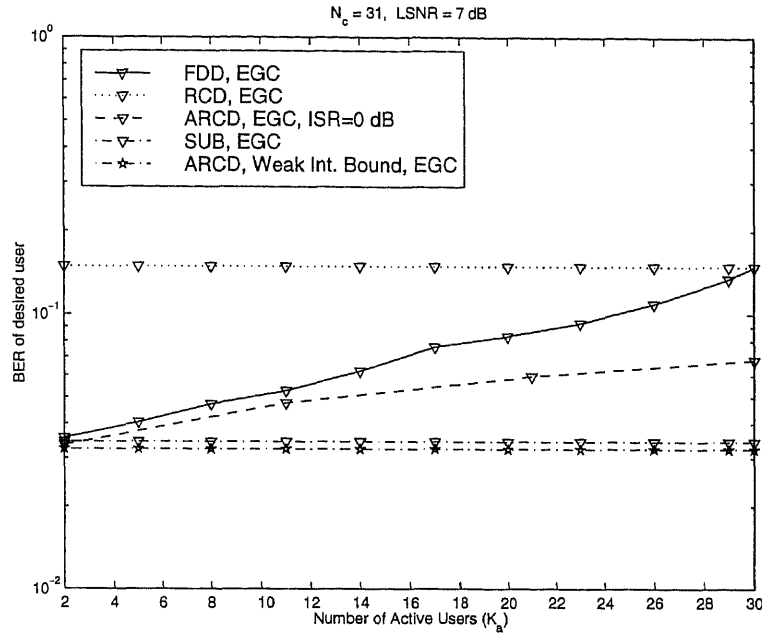


**Figure 2.8** BER of the RCD, ARCD( $\text{ISR}=0$  dB), and FDD vs.  $K_a$  with EGC in an i.i.d. Rayleigh faded channel, averaged over 250 Monte-Carlo runs.

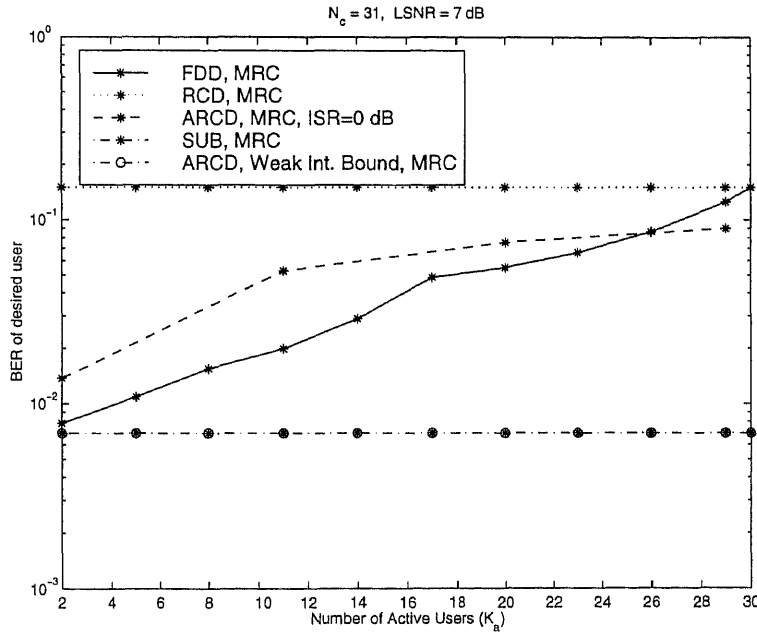


**Figure 2.9** BER of the RCD, ARCD( $\text{ISR}=0$  dB), and FDD vs.  $K_a$  with MRC in an i.i.d. Rayleigh faded channel, averaged over 250 Monte-Carlo runs.

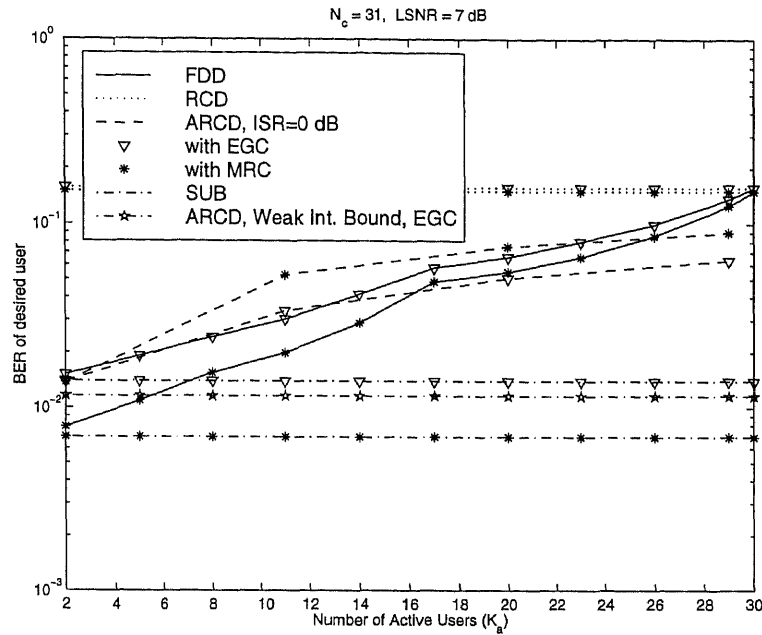


**Figure 2.10** BER of the RCD, ARCD( $ISR=0$  dB), and FDD vs.  $K_a$  with EGC and MRC in an i.i.d. Rayleigh faded channel, averaged over 250 Monte-Carlo runs.

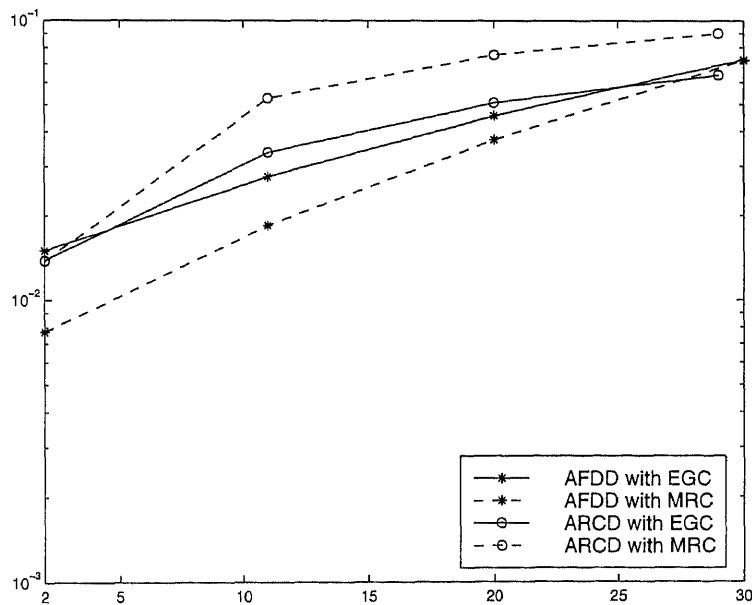


**Figure 2.11** BER of the ARCD and AFDD vs.  $K_a$  for  $ISR=0$  dB, with both EGC and MRC in an i.i.d. Rayleigh faded channel, averaged over 250 Monte-Carlo runs.

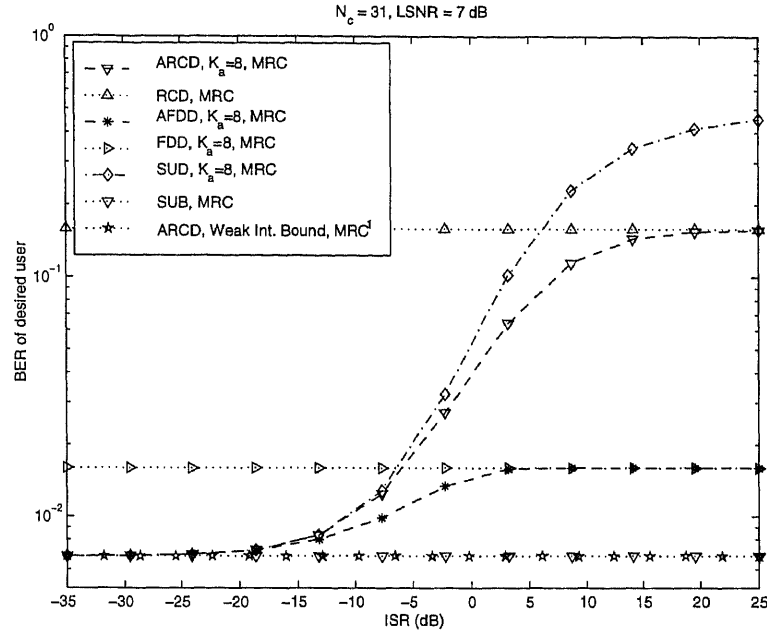


**Figure 2.12** BER of the ARCD and AFDD vs. ISR with EGC for  $K_a = 8$  in an i.i.d. Rayleigh faded channel, averaged over 100 Monte-Carlo runs. <sup>1</sup>Note that this line is a bound and therefore does not represent a function of the ISR.

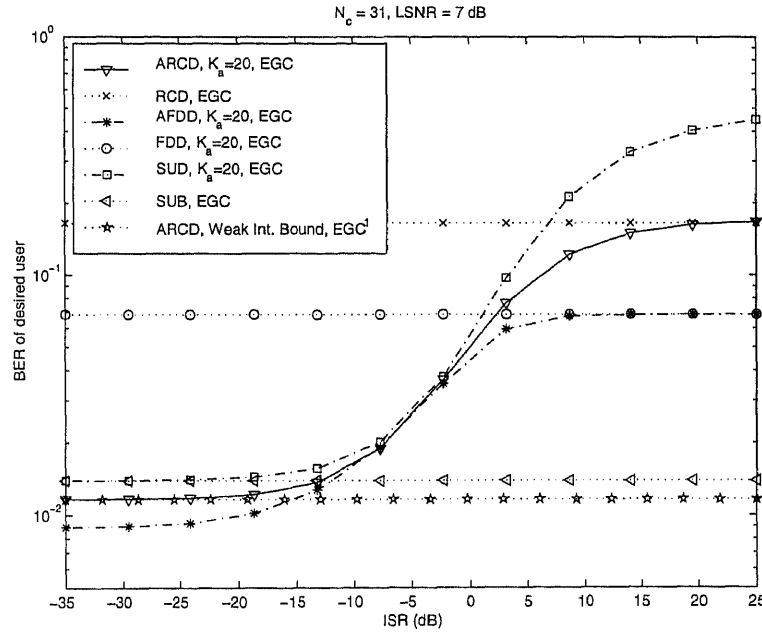


**Figure 2.13** BER of the ARCD and AFDD vs. ISR with EGC for  $K_a = 20$  in an i.i.d. Rayleigh faded channel, averaged over 100 Monte-Carlo runs. <sup>1</sup>Note that this line is a bound and therefore does not represent a function of the ISR.

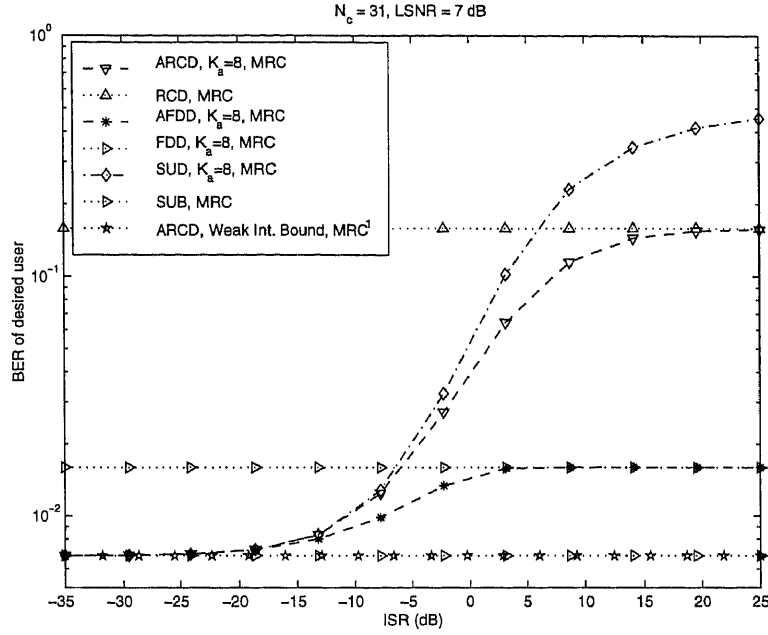


**Figure 2.14** BER of the ARCD and AFDD vs. ISR with MRC for  $K_a = 8$  in an i.i.d. Rayleigh faded channel, averaged over 100 Monte-Carlo runs. <sup>1</sup>Note that this line is a bound and therefore does not represent a function of the ISR.

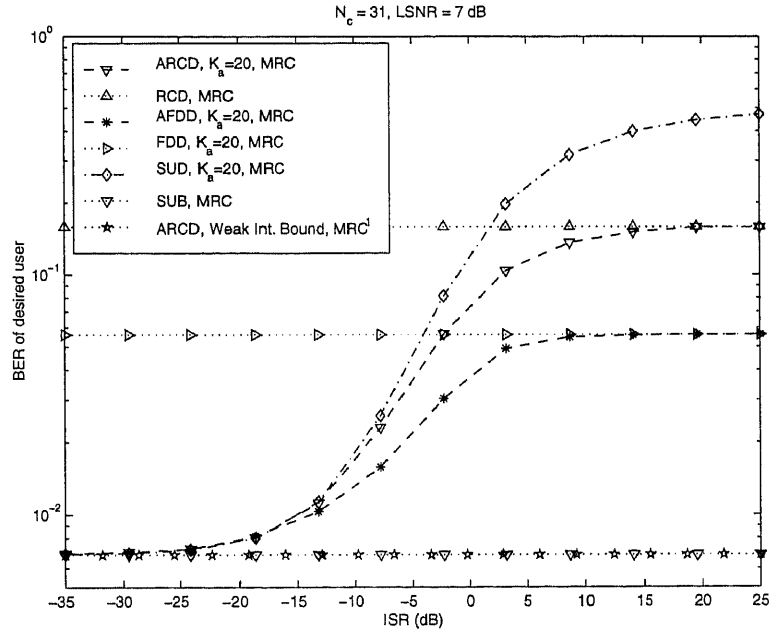


**Figure 2.15** BER of the ARCD and AFDD vs. ISR with MRC for  $K_a = 20$  in an i.i.d. Rayleigh faded channel, averaged over 100 Monte-Carlo runs. <sup>1</sup>Note that this line is a bound and therefore does not represent a function of the ISR.



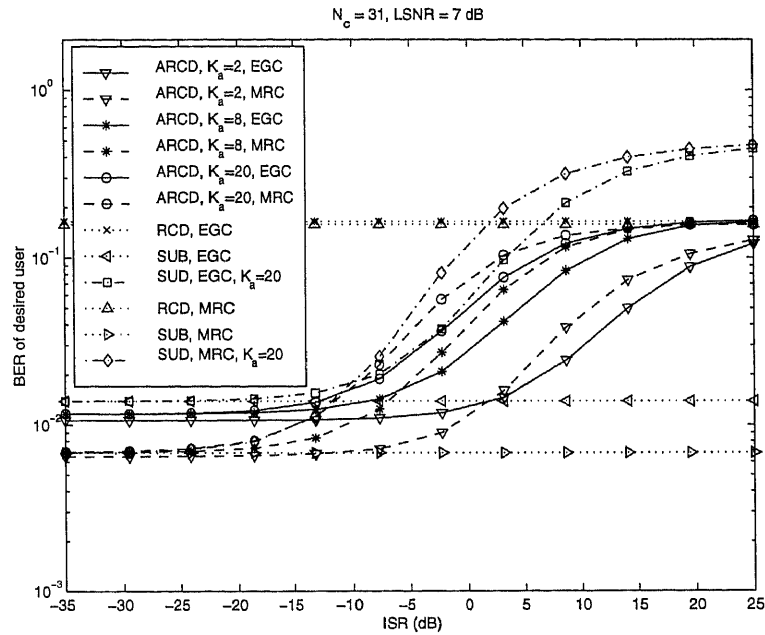


**Figure 2.16** BER of the ARCD vs. ISR with EGC and MRC for  $K_a = 2, 8, 20$  in an i.i.d. Rayleigh faded channel, averaged over 100 Monte-Carlo runs.

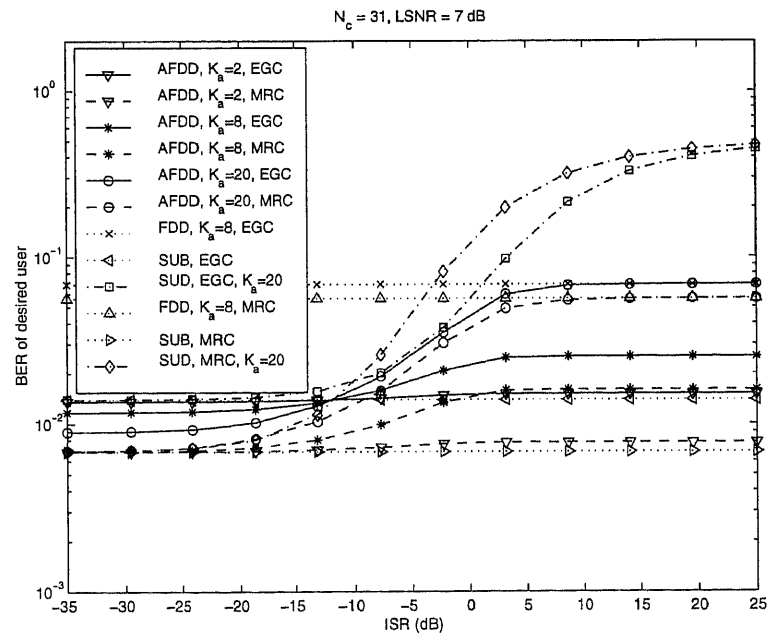


**Figure 2.17** BER of the AFDD vs. ISR with EGC and MRC for  $K_a = 2, 8, 20$  in an i.i.d. Rayleigh faded channel, averaged over 100 Monte-Carlo runs.

#### 2.4.4 Correlated Rayleigh Fading Channel

In this subsection a Rayleigh fading channel with correlation between the subcarriers is assumed. The channel is modeled as a Land-Mobile (LM) channel in an urban environment for which the maximum multipath delay (relative to the first path),  $\tau_{max}$ , typically is 1–3  $\mu s$ . As the rms channel delay spread  $\tau_d$  is always less than  $\tau_{max}$ ,  $\tau_d = 0.5 \mu s$  is selected. Additionally, the total bandwidth  $B_t = 2.06$  MHz, such that  $\Delta f \approx 64.5$  kHz. Also, it is assumed that  $F = 1$  such that the subcarriers are spaced by  $1/T_b$ , the closest possible spacing. These parameters define the correlation as expressed in equation (2.5) and as a result approximately five subcarriers fall within the coherence bandwidth. The generation of the correlated fading is detailed in appendix A.

Simulations for the correlated Rayleigh fading channel have been carried out with the following parameters:  $N_c = 31$  subcarriers, the local mean signal-to-noise ratio (LSNR) of the desired user is 7 dB, the maximum number of users,  $K = 30$ . The performance of the SUB, FDD, RCD and the bootstrap algorithm in the low ISR region, has been determined numerically by the application of the Q-function. All other BER curves have been obtained by bit error counting over  $10^5$  bits in the steady state of the adaptive algorithm. Since the BER is dependent on the channel realization, average BER curves are shown, where the averaging is indicated by the number of Monte-Carlo runs ( $N_{mc}$ ). For each Monte-Carlo run the conditional BER is obtained by bit error counting over  $10^5$  bits. The step-size parameter,  $\mu$ , of the bootstrap algorithm has been selected as  $\mu = 0.5 \times 10^{-3}$ . These parameters are summarized in table 2.4.4.

Figure 2.18 shows the performance of the RCD, the FDD, and the ARCD for  $ISR=0$  dB, in a correlated Rayleigh fading channel as a function of the number of active users ( $K_a$ ) for both EGC and MRC. Again, comparing the curves for the RCD and the FDD a trade-off between complexity and performance is noted. For

**Table 2.4** Parameters for simulation in a correlated Rayleigh fading channel.

Parameter	Value
$B_t$	2.06 Mhz
$\tau_d$	0.5 $\mu s$
$N_c$	31
$F$	1
$\Delta f$	64.5 kHz
$K$	30
LSNR	7 dB
$N_b$	$10^5$
$\mu$	$0.5 \times 10^{-3}$
$N_{mc}$	100 or 250

ISR=0 dB it is shown that the ARCD provides a considerable improvement over the RCD for both EGC and MRC. Moreover, the performance of the ARCD at ISR=0 dB with EGC is better than with MRC, for all numbers of active users, because MRC ignores the MUI, which decreases the SINR. The figure also shows that the ARCD at ISR=0 dB and with EGC always outperforms the FDD. For MRC, however, this is only the case when  $K_a > 17$  users are active. Additionally, as expected, the performance of the ARCD for weak interferers is closer to the SUB than in the case of an i.i.d. Rayleigh fading channel, because of less frequency diversity.

In comparing figure 2.18 with figure 2.10 it is noticed, as anticipated, that the SUB is higher for correlated Rayleigh fading than for i.i.d. Rayleigh fading for both EGC and MRC due to the reduced frequency diversity. The comparison also shows that, for EGC and MRC, the RCD performs almost the same for both channel types.

The performance of the ARCD at ISR=0 dB, in both i.i.d. and correlated Rayleigh fading channels, and for EGC as well as MRC is exemplified in figure 2.19. This figure shows that for both channel types EGC outperforms MRC for all numbers

of active users. This is consistent with our previous explanation that MRC does not necessarily improve the SINR. The figure also shows that the ARCD for a low number of active users, performs considerably better in an i.i.d. Rayleigh fading channel than in a correlated Rayleigh fading channel. However, as the number of active users increases the BER for the i.i.d. Rayleigh fading channel increases more rapidly than that of the correlated Rayleigh fading channel. As a result, both channel types have almost equal performance for a high number of active users.

Figure 2.20 shows the performance of the FDD in both i.i.d. and correlated Rayleigh fading channels, and for EGC as well as MRC. As expected, the performance of the FDD in an i.i.d. Rayleigh fading channel is better than in a correlated Rayleigh Fading channel. However, the performance difference between these two channel types becomes smaller for higher  $K_a$ . Additionally, the figure shows that for the FDD, MRC always outperforms EGC.

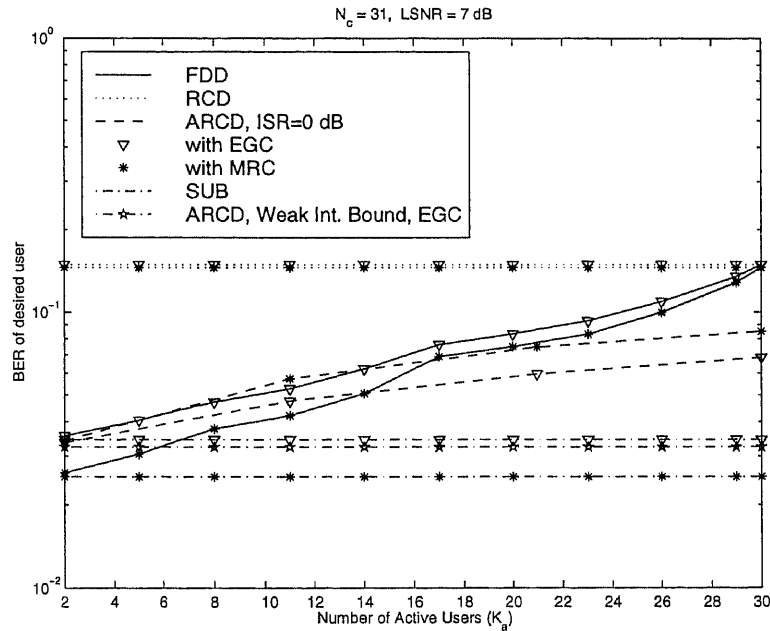


**Figure 2.18** BER of the RCD, ARCD(ISR=0 dB), and FDD vs.  $K_a$  with EGC and MRC in a correlated Rayleigh faded channel, averaged over 250 Monte-Carlo runs.

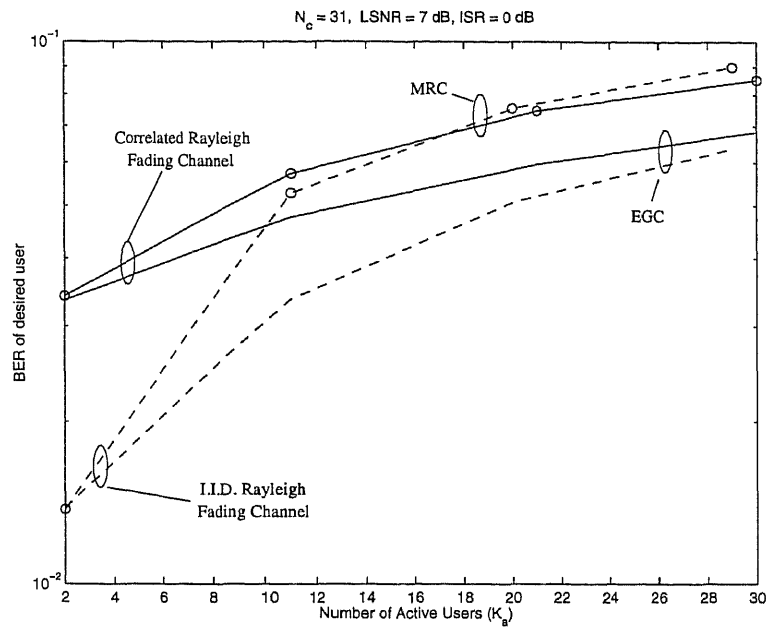


**Figure 2.19** BER of the ARCD (ISR=0 dB) vs.  $K_a$  with EGC and MRC in both an i.i.d. and correlated Rayleigh fading channel, averaged over 250 monte-carlo runs.

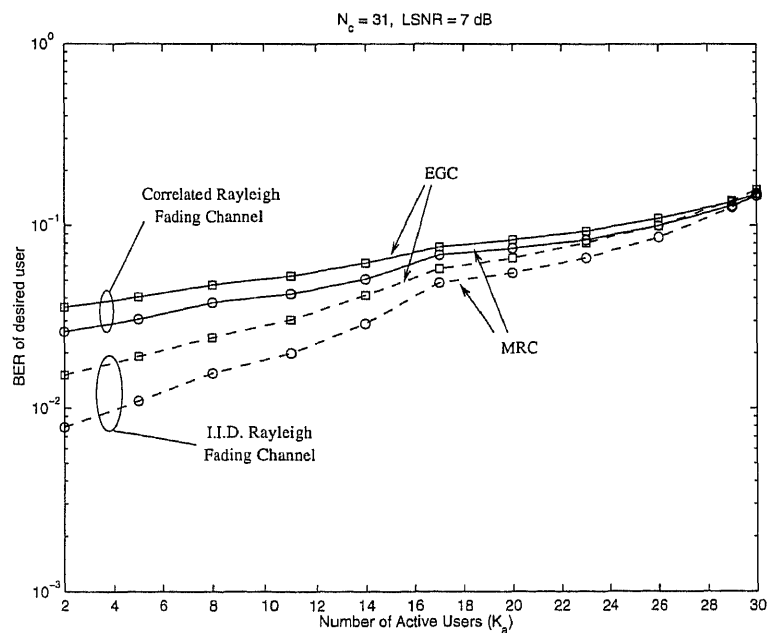


**Figure 2.20** BER of the FDD vs.  $K_a$  with EGC and MRC in both an i.i.d. and correlated Rayleigh fading channel, averaged over 250 monte-carlo runs.

## CHAPTER 3

### FREQUENCY OFFSET CORRECTION FOR OFDM

#### 3.1 Frequency Offset Correction Using a Blind Adaptive Decorrelator

In this section a method for eliminating the inter-carrier interference based on a blind adaptive decorrelator at the output of the OFDM demodulator is described. Following the initial decorrelator another decorrelator is applied to decorrelate the inphase and quadrature components of each subcarrier output, this also means that the constellation is rotated back to its original position. Additionally, a way for reducing the complexity of the adaptive decorrelator, by a factor  $N_c$ , will be shown, which is based on the circulant property of the ICI.

##### 3.1.1 System Model

The considered OFDM system block diagram is shown in figure 3.1. The system consists of  $N_c$  subcarriers, separated in frequency by  $\Delta f = 1/(N_c T_s)$ , where  $T_s$  is the unmodulated symbol duration. Each subcarrier is M-QAM modulated and the subcarrier generation can be efficiently implemented by an  $N_c$ -point inverse DFT operation, such that  $\mathbf{X} = \text{IDFT}\{\mathbf{b}\}$ . The output of the modulator,  $\mathbf{X}$ , is called an OFDM frame and consists of  $N_c$  samples of duration  $T_s$ , i.e. the duration of the OFDM frame is  $N_c T_s$ . The elements of  $\mathbf{X}$  are described by:

$$X_n = \sum_{l=0}^{N_c-1} b_l e^{j \frac{2\pi n l}{N_c}}, \quad (3.1)$$

where the  $b_l = b_l^I + j b_l^Q$  represents a point in a square M-QAM constellation, such that  $b^I, b^Q \in \{-\sqrt{M} + 1, -\sqrt{M} + 3, \dots, -1, 1, \dots, \sqrt{M} - 3, \sqrt{M} - 1\}$ . Thus, the average transmitted power per symbol is:

$$E_{\text{av}} = \frac{2(M-1)E_0}{3}, \quad (3.2)$$

where  $M$  is the number of points in the signal constellation and  $E_0$  is the energy of the constellation point with the lowest amplitude. Additionally, it is instructive to

think of the elements of  $\mathbf{b}$  as the frequency domain samples and those of  $\mathbf{X}$  as the corresponding time domain samples of the DFT pair, which is also indicated by the parallel-to-serial (P/S) conversion in figure 3.1.

The channel is considered frequency selective with respect to the total bandwidth. The subcarrier bandwidth, however, is assumed to be much smaller than the coherence bandwidth such that each subcarrier is subjected to flat Rayleigh fading. Thus, it is assumed that no inter-symbol interference occurs such that no guard-interval is needed. Taking into account the amplitudes of the subcarriers, the output of the channel may then be described as:

$$\mathcal{X}_n = \sum_{l=0}^{N_c-1} a_l b_l e^{j \frac{2\pi n l}{N_c}} = \text{IDFT}\{\mathbf{A}\mathbf{b}\}, \quad (3.3)$$

where  $a_l$  indicates the amplitude of the  $l^{\text{th}}$  subcarrier and  $\mathbf{A} = \text{diag}\{a_1, a_2, \dots, a_{N_c}\}$  is a diagonal matrix. The  $a_l$  are Rayleigh distributed random variables and possibly correlated.

The matched filter can be implemented as a quadrature detector, sampled at  $T_s$ . The complex valued samples are then passed to the  $N_c$ -point DFT for demodulation. As a result of the frequency offset the output of the DFT can be described by:

$$z_k = \frac{1}{N_c} \sum_{l=0}^{N_c-1} \mathcal{X}_l e^{-j \frac{2\pi l k}{N_c}} e^{j \frac{2\pi l \varepsilon}{N_c}} + \xi_k, \quad (3.4)$$

where  $\xi_k$  is a zero-mean complex Gaussian additive noise sample with variance  $\sigma_\xi^2$  and  $\varepsilon$  is the frequency offset normalized by the subcarrier spacing,

$$\varepsilon = \frac{\text{offset}}{\Delta f}. \quad (3.5)$$

After some goniometric manipulations  $z_k$  can be expressed as:

$$z_k = \sum_{m=0}^{N_c-1} s(m-k) a_m b_m + \xi_k, \quad (3.6)$$

where  $s(m-k)$  is defined as (see also appendix C):

$$s(m-k) = \frac{\sin(\pi \varepsilon) e^{j\pi \varepsilon}}{N_c} \left\{ \cot \left[ \frac{\pi(m-k+\varepsilon)}{N_c} \right] - j \right\}. \quad (3.7)$$

In order to get more insight in the effect of the frequency offset, the expression for  $z_k$  can be expressed as a sum of the signal, inter-carrier interference and the noise contribution respectively:

$$z_k = s(0)a_k b_k + \sum_{\substack{m=1 \\ m \neq k}}^{N_c-1} s(m-k)a_m b_m + \xi_k. \quad (3.8)$$

Combining the  $N_c$  DFT outputs,  $z_k$ , into a length  $N_c$  vector  $\mathbf{z}$ , it follows that:

$$\mathbf{z} = \mathbf{S}^T \mathbf{A} \mathbf{b} + \boldsymbol{\xi}, \quad (3.9)$$

where the  $N_c \times N_c$  matrix  $\mathbf{S}$ , which is termed the subcarrier correlation matrix, is defined using  $\mathbf{S}(n, m) = s(n - m)$ :

$$\mathbf{S} = \begin{bmatrix} s(0) & s(-1) & \dots & s(-N_c + 1) \\ s(1) & s(0) & \dots & s(-N_c + 2) \\ \vdots & & \ddots & \vdots \\ s(N_c - 1) & s(N_c - 2) & \dots & s(0) \end{bmatrix}. \quad (3.10)$$

and  $\boldsymbol{\xi}$  is a  $N_c \times 1$  vector containing i.i.d. zero-mean complex Gaussian additive noise components with variance  $\sigma_\xi^2$ . The subcarrier correlation matrix  $\mathbf{S}$  has the following three properties: (1) it is non-hermitian, i.e.  $\mathbf{S} \neq \mathbf{S}^H$ ; (2) it is orthonormal, i.e.  $\mathbf{S}^H \mathbf{S} = \mathbf{I}$  (or, equivalently, it is unitary as  $\mathbf{S}^H = \mathbf{S}^{-1}$ ); (3) it is a circulant matrix, i.e. the columns (as well as the rows) are shifted versions of each other, as  $s(i) = s(i + nN_c)$  for any integer  $n$ .

### 3.1.2 Time-Variant Channel

In [44] a method called Wittwer's fading channel simulator is described. This simulator is based on a fading power spectrum which falls off as  $f^{-4}$ . The implementation of this simulator is shown in figure 3.2, where  $p_n$  is a complex Gaussian noise sample with  $E[p_n^* p_{n+l}] = \delta(l)$ . The decorrelation time or coherence time,  $\tau_0$ , is defined as that value of  $\tau$  for which the correlation function has decreased to  $1/e$  of its peak. This choice for  $\tau_0$  yields  $\alpha = 2.146/\tau_0$  and  $\beta = \exp(-\alpha/T)$ , where  $T$  is the



unit time between samples. The fading rate is defined as  $1/\tau_0$ . The  $s_n$  are correlated complex Gaussian samples with approximate (for  $t_0/T \geq 10$ ) correlation function:

$$R_s(l) = E[s_n^* s_{n+l}] = (1 + \alpha l T) e^{-\alpha l T}. \quad (3.11)$$

The time-variant channel is implemented such that the fading parameters at each subcarrier are correlated in time whereas they are uncorrelated in frequency, i.e. the fading parameters at different subcarriers are uncorrelated. This channel can be implemented by using  $N$ , i.e. one for each subcarrier, independent fading simulators as shown in figure 3.2. The Rayleigh distributed channel amplitude is easily generated by  $a(i) = |s_i|$ , where  $i$  denotes the time dependence.

Figure 3.3 shows a simulated correlation function for  $\tau_0 = 1000$ .

### 3.1.3 Channel Amplitude Estimation

In order to be able to correctly detect the M-QAM symbols the received signal will be scaled by a factor  $1/\hat{a}_m$  for the  $m^{\text{th}}$  subcarrier, to compensate for the channel amplitude response (see also figure 3.1). In the simulations a very simple, sliding-window, channel amplitude estimation algorithm is employed:

$$\hat{a}_m = \left( \frac{1}{\mathcal{W}} \sum_{w=0}^{\mathcal{W}-1} |\tilde{y}_m(i-w-1)|^2 \right)^{1/2}. \quad (3.12)$$

where  $\mathcal{W}$  indicates the window length for averaging the last  $\mathcal{W}$  samples at the output of the decorrelator. Once the adaptive decorrelator is in the steady state, the output signal will be free of interference except for Gaussian noise. Hence, the channel estimates so obtained will, of course, be biased by the noise power. Simulations, however, will show that this does not greatly affect the performance of the overall detector.

### 3.1.4 Decorrelator Based Frequency Offset Correction

As the ICI introduces correlation between the different outputs of the DFT it is proposed to reduce the ICI by adding a decorrelator at the output of the DFT.

A so-called *conventional decorrelator* for frequency offset correction may be defined as the inverse of the transpose of the subcarrier correlation matrix  $\mathbf{S}$ , analogously to the conventional decorrelator previously defined for multiuser detection (see also section 2.2). From equation 3.9 it is clear that using  $(\mathbf{S}^T)^{-1} = \mathbf{S}^*$  will completely cancel all the ICI and thus correct for the effects of the frequency offset.

Because the use of the inverse of the subcarrier correlation matrix requires knowledge of the normalized frequency offset, an adaptive decorrelating detector is developed, utilizing the application of a linear transformation  $\mathbf{V}$  to the subcarrier outputs. In matrix notation this results in the following:

$$\mathbf{y}_v = \mathbf{V}^H \mathbf{z} = \mathbf{V}^H \mathbf{S}^T \mathbf{A} \mathbf{b} + \mathbf{V}^H \boldsymbol{\xi}, \quad (3.13)$$

where the  $K_a \times K_a$  matrix  $\mathbf{V} = \mathbf{I} - \mathbf{W}$  and where  $\mathbf{W}$  is a  $K_a \times K_a$  matrix with zeros on the diagonal to preserve the desired signal, a method previously used for multiuser interference cancelation [32, 45]. Using this definition for  $\mathbf{V}$  it follows that:

$$\mathbf{y} = (\mathbf{I} - \mathbf{W})^H \mathbf{z} = \mathbf{z} - \mathbf{W}^H \mathbf{z}. \quad (3.14)$$

In order to decorrelate the different outputs of the DFT and to motivate the adaptive control it has been proposed in [22] to choose the weight matrix  $\mathbf{W}$  such that

$$E[y_k \mathbf{b}_k] = \mathbf{0}, \quad (3.15)$$

where  $\mathbf{b}_k$  is the vector  $\mathbf{b}$  without the  $k^{\text{th}}$  element. If the SINR at any decorrelator output ( $j \neq k$ ) is sufficiently high then  $E[y_k \hat{b}_j] \simeq E[y_k b_j (1 - P_{e_j})]$ . The condition in equation (3.15) may then be interpreted as an approximation to  $E[y_k \hat{\mathbf{b}}_k] = \mathbf{0}$ , where  $\hat{\mathbf{b}}_k = \text{sgn}(\mathbf{y}_k)$  is the estimate of  $\mathbf{b}_k$  and  $\mathbf{y}_k$  is  $\mathbf{y}_v$  without the  $k^{\text{th}}$  element. Without loss of generality and assuming the condition on the SINR is met, equation (3.15) is expanded for  $k = 1$ :

$$E[y_1 \mathbf{b}_1] = E[(z_1 - \mathbf{w}_1^H \mathbf{z}_1) \mathbf{b}_1], \quad (3.16)$$

where  $\mathbf{w}_1$  is the first column of  $\mathbf{W}$  without the first element. To simplify the analysis, the subcarrier correlation matrix  $\mathbf{S}$  is partitioned as follows in the case of  $k = 1$ :

$$\mathbf{S} = \begin{bmatrix} s(0) & \tilde{\mathbf{s}}_{10}^T \\ \mathbf{s}_{10} & \mathbf{S}_{11} \end{bmatrix}. \quad (3.17)$$

Utilizing the partitioned subcarrier correlation matrix and assuming the data transmitted on different subcarriers is uncorrelated it follows that

$$\begin{aligned} E[y_1 \mathbf{b}_1] &= E[(s(0)a_1b_1 + \mathbf{s}_{10}^T \mathbf{A}_{11} \mathbf{b}_1) \mathbf{b}_1 - \mathbf{w}_1^H (\tilde{\mathbf{s}}_{10}a_1b_1 + \mathbf{S}_{11}^T \mathbf{A}_{11} \mathbf{b}_1) \mathbf{b}_1] \\ &= \mathbf{A}_{11} \mathbf{s}_{10} - \mathbf{A}_{11} \mathbf{S}_{11} \mathbf{w}_1^*, \end{aligned} \quad (3.18)$$

where  $\mathbf{A}_{11}$  is  $\mathbf{A}$  without its first row and column and the  $*$  operator denotes complex conjugation. Equating this expression to zero and solving for  $\mathbf{w}_1$ :

$$\mathbf{w}_1^* = (\mathbf{A}_{11} \mathbf{S}_{11})^{-1} \mathbf{A}_{11} \mathbf{s}_{10} = \mathbf{S}_{11}^{-1} \mathbf{s}_{10}. \quad (3.19)$$

These weights will be referred to as the *decorrelating weights*. Note that these *decorrelating weights* do not depend on the channel realizations. Due to the circulant property of  $\mathbf{S}$  the other columns of  $\mathbf{W}$  will be circularly shifted versions of  $\mathbf{w}_1$ , hence only  $N_c - 1$  complex weight values need to be determined.

Using the decorrelation weights as defined in equation (3.19) the  $k^{\text{th}}$  output of the decorrelator can be expressed as,

$$y_k = (s(0) - \mathbf{s}_{k0}^T (\mathbf{S}_{kk}^{-1})^T \tilde{\mathbf{s}}_{k0}) a_k b(k) = \alpha_k a_k b(k), \quad (3.20)$$

where  $\alpha_k$  represents the rotation of the symbol  $b(k)$ , which causes the so called inter-rail interference between the inphase (I) and quadrature (Q) components of  $b(k)$ . Note, it can be shown that  $\alpha_k$  is the same for all  $k$ , hence  $\alpha_k = \alpha$ . The effect of the rotation on a 16-QAM constellation is shown in figure 3.5(c) for  $N = 8$ ,  $\varepsilon = 0.2$  and  $\text{SNR} = 16$  dB. Also, comparing figure 3.5(b) and (c) shows that the received constellation points are more confined around the 'actual' constellation points as a result of the first decorrelation stage.

The I and Q components of each subcarrier may be decorrelated, assuming they were originally uncorrelated and the rotation is small enough (approximately satisfied when  $\text{angle}\{\alpha_k\} < \pi/4$  rad). The decorrelation is accomplished using a linear transformation  $\mathbf{V}_{\text{rot}_k}$  at each output of the first decorrelation stage (see figure 3.4). Because the constellation rotation is equal for all the subcarrier outputs, it follows that  $\mathbf{V}_{\text{rot}_k} = \mathbf{V}_{\text{rot}}$ .

In order to find the solution for the elements of  $\mathbf{V}_{\text{rot}}$  a vector  $\boldsymbol{\beta}$  is defined:

$$\boldsymbol{\beta}_k = \begin{bmatrix} \text{Re}\{\alpha b_k\} \\ \text{Im}\{\alpha b_k\} \end{bmatrix}. \quad (3.21)$$

The output of the I-Q decorrelator then becomes,

$$\begin{bmatrix} \text{Re}\{\tilde{y}_k\} \\ \text{Im}\{\tilde{y}_k\} \end{bmatrix} = \mathbf{V}_{\text{rot}}^T \boldsymbol{\beta}_k = \begin{bmatrix} 1 & -w_{r21} \\ -w_{r12} & 1 \end{bmatrix} \begin{bmatrix} \text{Re}\{\alpha b_k\} \\ \text{Im}\{\alpha b_k\} \end{bmatrix}. \quad (3.22)$$

From this equation, the weight values that cancel the effect of  $\alpha$  can easily be derived:

$$w_{r12} = -w_{r21} = \frac{\text{Im}\{\alpha\}}{\text{Re}\{\alpha\}}. \quad (3.23)$$

Using these weight values effectively rotates the constellation back to its original orientation as shown in figure 3.5(d). Additionally, as  $\mathbf{V}_{\text{rot}}$  is the same for each output only one additional weight value needs to be computed.

### 3.1.5 Adaptive Implementation

As  $\varepsilon$ , and thus  $\mathbf{S}$ , is unknown at the receiver it is proposed to use an adaptive algorithm, called complex bootstrap algorithm [46], to decorrelate the DFT outputs. Following this first adaptive decorrelator, a second adaptive decorrelator based on the real bootstrap algorithm is used. It will be shown by simulation that the performance of the adaptive decorrelator equals the performance when using the decorrelating weights.

The complex bootstrap algorithm uses the following recursive weight update equation:

$$\mathbf{w}_k(i+1) = \mathbf{w}_k(i) + \mu y_k^* \text{csgn}(\mathbf{y}_k), \quad (3.24)$$

where  $i$  denotes the time index of the OFDM symbol,  $\mu$  is the step-size parameter of the adaptation process and  $\text{csgn}(\cdot)$  is defined as  $\text{sgn}(\text{Re}\{\cdot\}) + j\text{sgn}(\text{Im}\{\cdot\})$ .

The  $2 \times 2$  real bootstrap algorithm used for the second, I-Q decorrelation stage uses

$$w_{r12}(i+1) = w_{r12}(i) + \mu_{\text{rot}} \text{Im}\{\tilde{y}_k\} \text{sgn}(\text{Re}\{\tilde{y}_k\}), \quad (3.25)$$

as the recursive weight update equation. Moreover,  $\mu_{\text{rot}}$  is the step-size parameter of the adaptation process.

### 3.1.6 Discussion of Results

**3.1.6.1 Non-faded AWGN Channel:** Using the orthonormal property of  $\mathbf{S}$ , i.e.  $\mathbf{s}_k^H \mathbf{s}_k = \sum_{n=0}^{N_c-1} |s(n)|^2 = 1$ , and using equation (3.8) the CIR of conventional OFDM, i.e. at the output of the DFT operation, can be formulated for  $k = 0$ :

$$\text{CIR}_{\text{ofdm}} = \frac{E_{av} |s(0)|^2}{\sum_{n=1}^{N_c-1} |s(n)|^2} = \frac{E_{av} |s(0)|^2}{1 - |s(0)|^2}. \quad (3.26)$$

It is clear that when the frequency offset  $\varepsilon$  increases the signal part decreases, as  $|s(0)|$  decreases because the constellation is further rotated. Additionally, the inter-carrier interference increases. In particular, figure 1.4 shows the decrease in CIR as a function of the normalized frequency offset. Rather than the CIR the SINR can be used, as it is a more realistic measure of the performance in a noisy environment. Equation (3.26) can easily be augmented to yield the SINR of conventional OFDM (at the output of the DFT operation):

$$\text{SINR}_{\text{ofdm}} = \frac{E_{av} |s(0)|^2}{\sum_{n=1}^{N_c-1} |s(n)|^2 + \sigma_\xi^2} = \frac{E_{av} |s(0)|^2}{1 - |s(0)|^2 + \sigma_\xi^2}. \quad (3.27)$$

In order to derive the output SINR when using the decorrelator we use equation (3.13) to get:

$$\begin{aligned} E[|\mathbf{y}|^2] &= E[\mathbf{V}^H \mathbf{S}^T \mathbf{b} \mathbf{b}^H \mathbf{S}^* \mathbf{V} + \mathbf{V}^H \boldsymbol{\xi} \boldsymbol{\xi}^H \mathbf{V}] \\ &= \gamma \mathbf{I}_{N_c} + \gamma \sigma_{\xi}^2 \mathbf{I}_{N_c}. \end{aligned} \quad (3.28)$$

where  $\gamma = \mathbf{v}_k^H \mathbf{v}_k$  and  $\mathbf{v}_k$  is any column of  $\mathbf{V}$ . Moreover, because the factor  $\gamma$  is present in the signal as well as the noise part it does not alter the SINR.

From equation (3.22), it can also easily be seen that

$$\mathbf{V}_{\text{rot}}^T \mathbf{V}_{\text{rot}} = \delta \mathbf{I}_2. \quad (3.29)$$

where  $\delta = 1 + (\text{Im}\{\alpha\}/\text{Re}\{\alpha\})^2$ . Therefore, it is concluded that the SINR at the output of the second decorrelator ( $\text{SINR}_V$ ) is equal to the SNR in the absence of a frequency offset ( $\text{SNR}_0$ ), i.e.  $\text{SINR}_V = \text{SNR}_0$ , where

$$\text{SNR}_0 = \frac{E_{av}}{\sigma_{\xi}^2}. \quad (3.30)$$

As a comparison the SINR of the ICI cancellation scheme discussed in [40] ( $\text{SINR}_{ici}$ ) and the SINR of OFDM with correlative coding [42] ( $\text{SINR}_{cc}$ ) is shown. The ICI cancellation scheme uses a form of repetition coding in the frequency domain, such that half the subcarriers are used for coding, i.e. the bandwidth efficiency is halved. The correlative coding scheme uses frequency domain correlative coding with correlation polynomial  $F(D) = 1 - D$ , which does not reduce the bandwidth efficiency. With  $E_{av} = 1$ , the SINR for these schemes can be shown to be

$$\text{SINR}_{ici} = \frac{1}{0.2\epsilon^2 + \sigma_{\xi}^2}, \quad (3.31)$$

$$\text{SINR}_{cc} = \frac{\sin^2(\pi\epsilon)/(\pi\epsilon)^2}{\sum_{n=1}^{N_c-1} |s(n)|^2 - \frac{1}{2} \sum_{n=2}^{N_c-1} [s(n)s^*(n-1) + s(n-1)s^*(n)] + \sigma_{\xi}^2}. \quad (3.32)$$

In figure 3.6 the SINR expressions are plotted as a function of the normalized frequency offset for  $N_c = 8$  subcarriers and an SNR of 0 dB, 10 dB and 20 dB. The

figure shows that the SINR for conventional OFDM quickly degrades for increasing  $\varepsilon$ . The SINR for the ICI cancelation scheme remains fairly constant and close to the SINR of the decorrelator for low SNRs because the noise power is dominant over the interference power. However, for higher SNRs the decorrelator clearly outperforms the ICI cancelation scheme as now the interference power dominates over the noise power. Additionally, one must realize that the ICI cancelation scheme has expended half of its bandwidth on the repetition coding. The correlative coding scheme performs better than conventional OFDM, however, not as good as the decorrelator or the ICI cancelation scheme.

In order to show the gain of the decorrelator using both stages, of the ICI cancelation scheme and of the correlative coding scheme relative to the conventional OFDM detector, the following three quantities are defined:

$$G_V = 10 \log_{10} \left( \frac{SINR_V}{SINR_{OFDM}} \right), \quad (3.33)$$

$$G_{ici} = 10 \log_{10} \left( \frac{SINR_{ici}}{SINR_{OFDM}} \right), \quad (3.34)$$

$$G_{cc} = 10 \log_{10} \left( \frac{SINR_{cc}}{SINR_{OFDM}} \right), \quad (3.35)$$

where  $G_V$ ,  $G_{ici}$  and  $G_{cc}$  express the gain over conventional OFDM of using both stages of the decorrelator, the ICI cancelation scheme and the correlative coding scheme respectively.

Figure 3.7 shows  $G_V$ ,  $G_{ici}$  and  $G_{cc}$  for  $N_c = 8$  subcarriers and an SNR of 0 dB, 10 dB and 20 dB. For small frequency offsets ( $\varepsilon < 0.05$ ) all schemes have a similar gain over conventional OFDM depending on the SNR. In general, the higher the SNR, the larger the gain over conventional OFDM as its performance drops off faster due to the dominance of the ICI relative to the noise. As  $\varepsilon$  increases, the performance differences between the different schemes increase, with the decorrelator always performing better than the other schemes. When  $\varepsilon = 0.2$  and SNR = 20 dB

the decorrelator performs 2.5 dB better than the ICI cancelation scheme and 6.5 dB better than the correlative coding scheme and 15 dB better than the conventional OFDM detector. Again, it must be noted that the bandwidth efficiency of the ICI cancelation scheme is half that of the other schemes.

Finally, in figure 3.8 simulation results of the Bit Error Rate (BER) for a 4-QAM OFDM transmission are shown versus the SNR for normalized frequency offsets of 10%, 15% and 20%. The BER after the first decorrelation stage ( $\mathbf{V}$ ) as well as after both stages ( $\mathbf{V}$  and  $\mathbf{V}_{\text{rot}}$ ) is compared to the BER of the matched filter. Clearly, the use of the first decorrelation stage significantly improves the performance over the matched filter performance. In addition, rotating the constellation using  $\mathbf{V}_{\text{rot}}$  completely eliminates the inter-rail interference, hence the performance becomes independent of the normalized frequency offset. Also, figure 3.8 shows that the performance is equal to the performance of a single carrier 4-QAM transmission in AWGN.

**3.1.6.2 Time-Variant Channel:** The use of the decorrelating weights for MUD in DS-CDMA and MC-CDMA leads to noise amplification, such that the performance is worse than the single user bound (see also chapter 2). The adaptive bootstrap algorithm performs similar to an MMSE detector, such that its performance reaches that of the SUB as the interference-to-signal-ratio (ISR) decreases.

The application of the decorrelating weights for FOC in OFDM does *not* lead to noise amplification (as  $\mathbf{V}^H \mathbf{V} = \eta \mathbf{I}$ ) due to the unitary structure of the  $\mathbf{S}$  matrix. This means that the decorrelating weights are optimum and thus the performance using the decorrelating weights is the best that can be achieved. Additionally, it has been shown in equation (3.19) that the decorrelating weights do not depend on the subcarrier amplitudes. This indicates that an adaptive algorithm to find the



optimum weights, as the one based on the bootstrap algorithm, should also *not* depend on the subcarrier amplitudes.

The regular implementation of the (complex) bootstrap algorithm inherently utilizes the amplitude information to improve the performance for low ISR. This is shown in the recursive update equation for the complex bootstrap in equation (3.24). Based on the previous discussion, however, it is proposed to remove this dependency on the subcarrier amplitudes. The (complex) bootstrap algorithm is modified by normalizing the signal vectors with the subcarrier amplitudes. This results in the so-called *augmented complex bootstrap algorithm*:

$$\mathbf{w}_k(i+1) = \mathbf{w}_k(i) + \mu \frac{y_k^*}{\hat{a}_k} \text{csgn} \left( \frac{\mathbf{y}_k}{\hat{\mathbf{a}}_k} \right). \quad (3.36)$$

Here, the division within the brackets is an element-by-element division (also referred to as right array division) of the two vectors, resulting in a vector of the same length. In addition,  $\hat{a}_k$  is the estimate of the channel amplitude of subcarrier  $k$ , and  $\hat{\mathbf{a}}_k$  is the vector containing the estimates of the channel amplitudes, except for the  $k^{\text{th}}$  element. It can easily be seen that the augmented complex bootstrap algorithm reduces to the complex bootstrap algorithm for a flat non-faded AWGN channel.

This augmented complex bootstrap algorithm no longer uses the subcarrier amplitude information that is embedded in the signals it attempts to decorrelate. As a result of the augmentation the stability of the bootstrap algorithm has been improved as can be seen by comparing figure 3.9 and figure 3.10. Figure 3.9 clearly shows that the complex bootstrap algorithm no longer converges when the channel amplitude changes too rapidly.

From figure 3.10 it can be seen that with the use of the augmented complex bootstrap algorithm, the BER for all three different values of  $\tau_0$  (where  $\tau_0$  is expressed in OFDM-symbols) is close to the optimum BER, achieved by the application of the conventional decorrelator  $\mathbf{S}^*$ . Additionally, it can be seen that there is only a small

loss in BER due to the use of imperfect channel estimation rather than the use of the actual channel amplitudes.

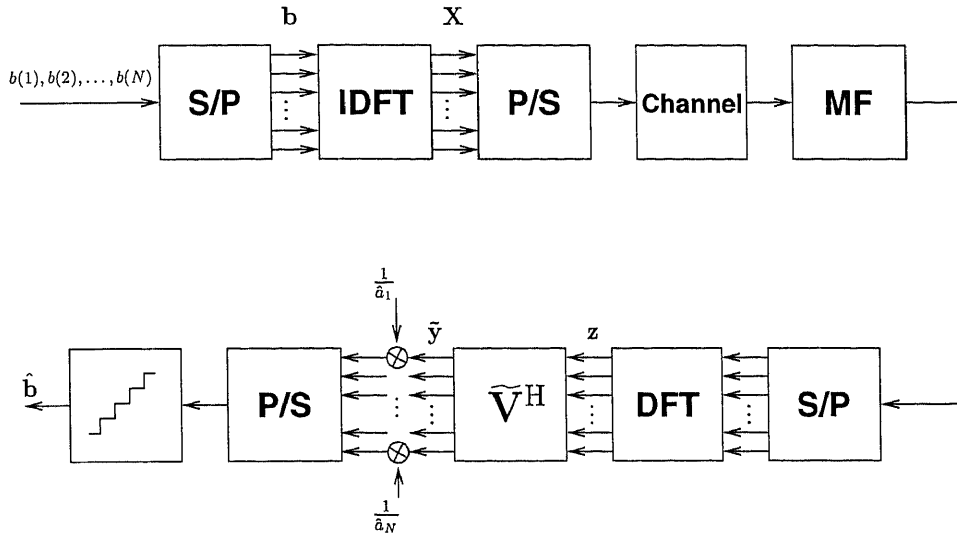


**Figure 3.1** Block diagram of an OFDM system with frequency offset correction.

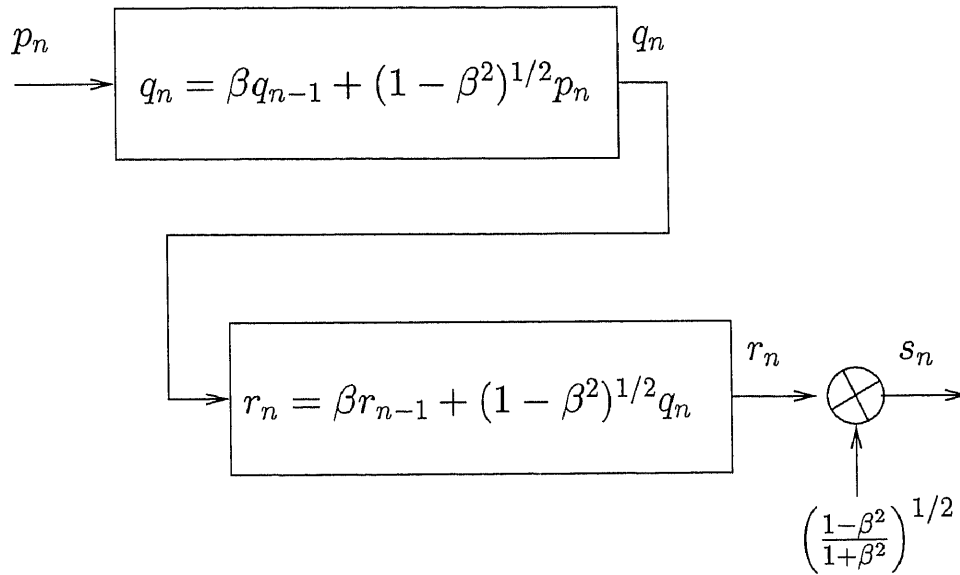


**Figure 3.2** Wittwer's method for generating correlated complex Gaussian samples.

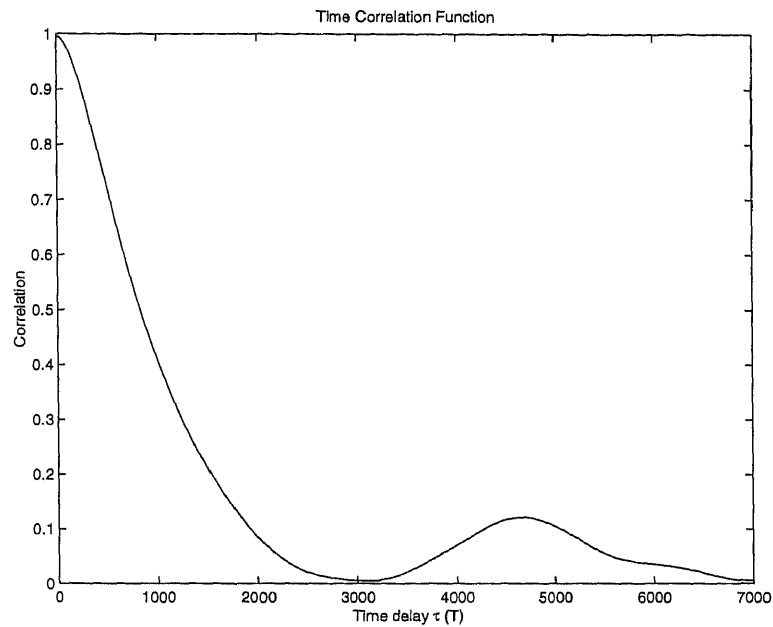


**Figure 3.3** Time Correlation Function for  $\tau_0 = 1000$ .

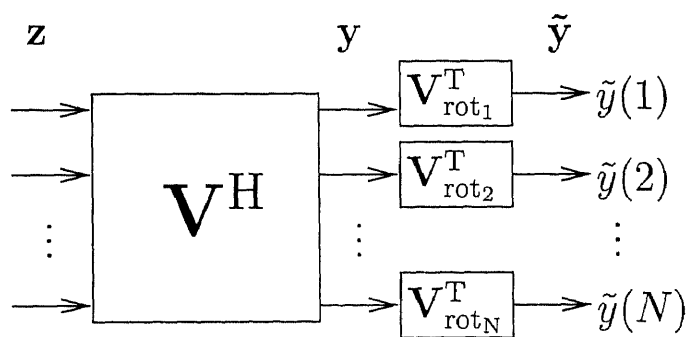


**Figure 3.4** Two stage implementation for adaptive frequency offset correction.

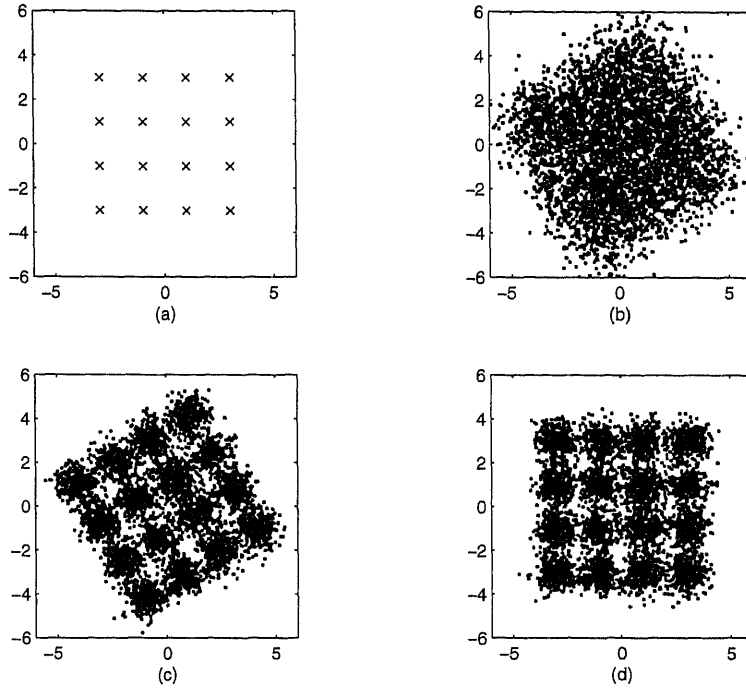


**Figure 3.5** Constellations of 16-QAM transmission for  $N_c = 8$ ,  $\varepsilon = 0.2$  and SNR = 16 dB, (a) transmitted constellation; (b) constellation at output of DFT; (c) constellation after  $\mathbf{V}$ ; (d) constellation after  $\tilde{\mathbf{V}}$ .

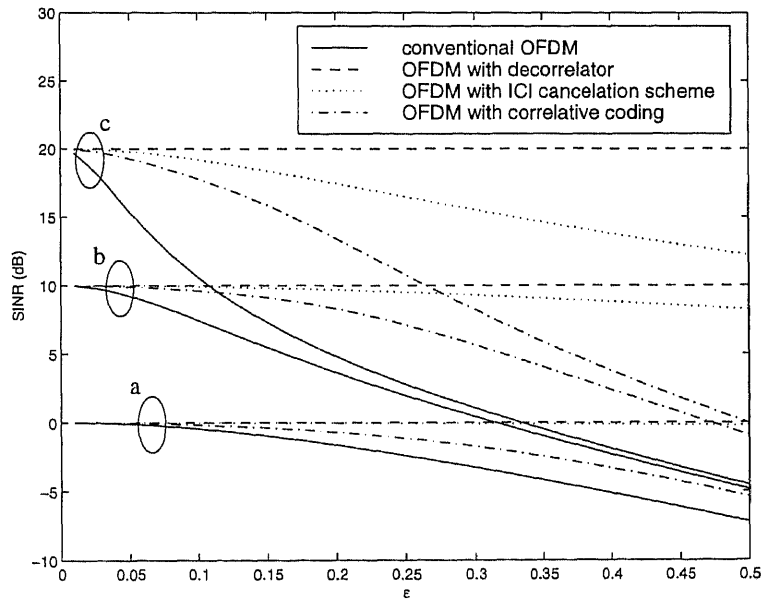


**Figure 3.6** SINR as a function of the normalized frequency offset  $\varepsilon$  for  $N_c = 8$  subcarriers, (a) SNR = 0 dB; (b) SNR = 10 dB; (c) SNR = 20 dB

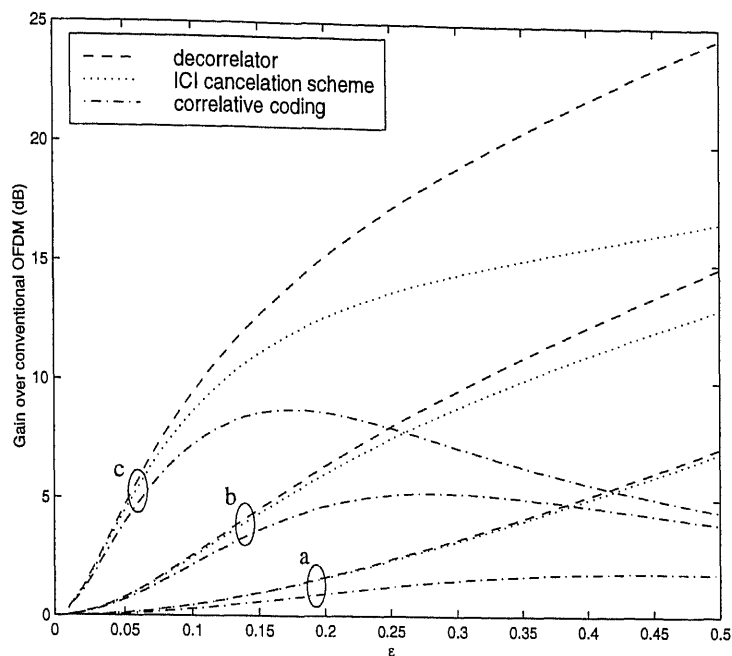


**Figure 3.7** Gain over conventional OFDM as a function of the normalized frequency offset  $\varepsilon$  for  $N_c = 8$  subcarriers, (a) SNR = 0 dB; (b) SNR = 10 dB; (c) SNR = 20 dB

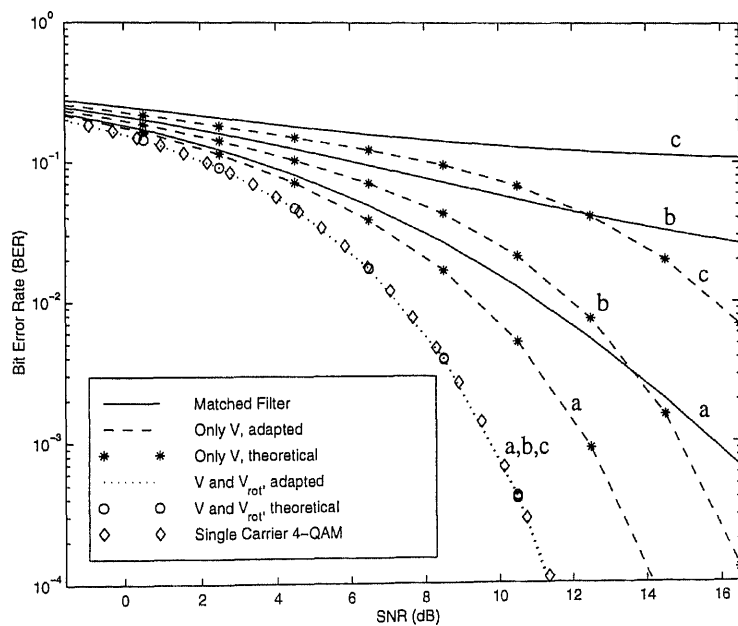


**Figure 3.8** Bit error rate of a 4-QAM transmission versus the SNR, (a)  $\varepsilon=0.1$ ; (b)  $\varepsilon=0.15$ ; (c)  $\varepsilon=0.2$

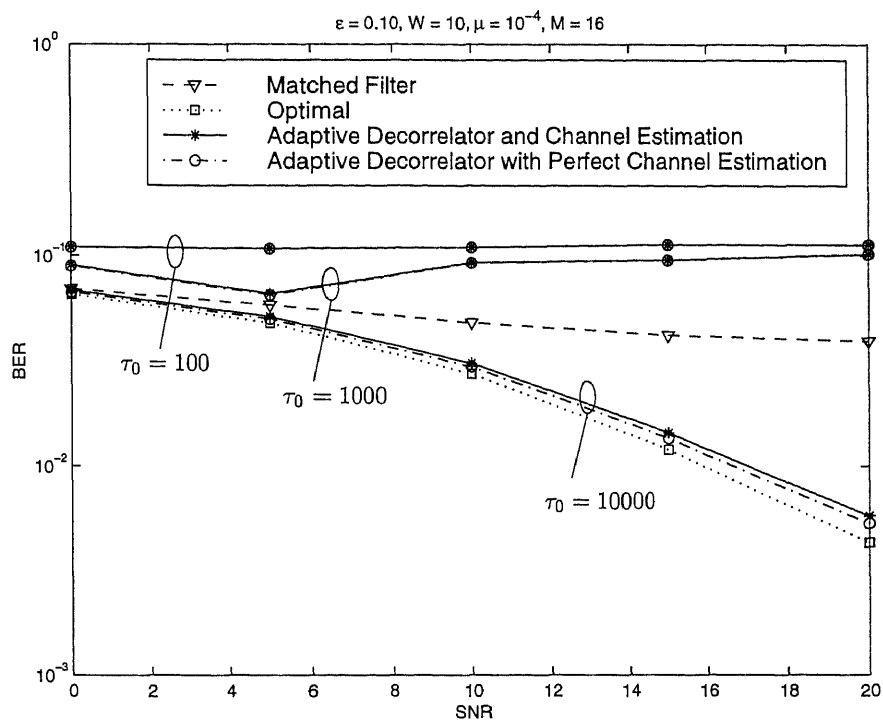


Figure 3.9 Performance with the regular bootstrap algorithm.

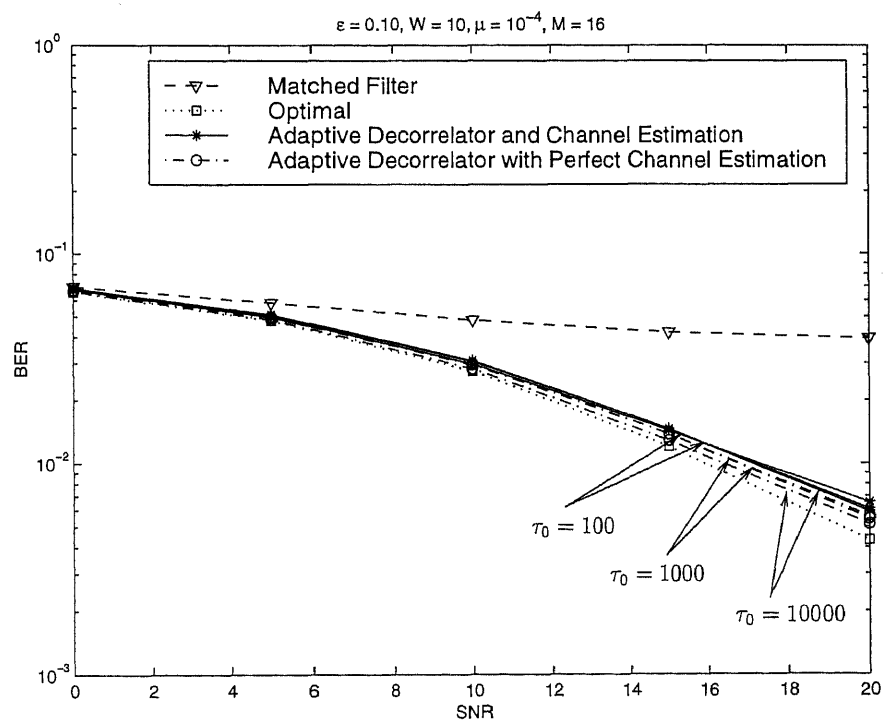


Figure 3.10 Performance with the augmented bootstrap algorithm.

### 3.2 Blind Adaptive Frequency Offset Estimation and Correction

In this section, a blind method for estimating the frequency offset is developed, which is based on the correlation of the received data samples. Additionally, an adaptive frequency offset correction algorithm is proposed. The algorithm is basically a stochastic gradient type algorithm which minimizes the mean squared frequency offset error. As our method does not require a training sequence or the retransmission of a data symbol there is no reduction in bandwidth efficiency.

#### 3.2.1 System Model

The considered OFDM system model is shown in figure 3.11. It consists of  $N_c$  equally spaced subcarriers, where each subcarrier is BPSK modulated. The multicarrier modulation can be efficiently implemented by the use of an inverse discrete Fourier transform. First, a sequence of  $N_c$  bits is converted from serial to parallel to form a vector  $\mathbf{b}$ . Then, the transmitted signal  $\mathbf{X}$  is formed from the  $N_c$ -point IDFT of  $\mathbf{b}$ . It is instructive to think of the elements of  $\mathbf{b}$  as the frequency domain samples and those of  $\mathbf{X}$  as the corresponding time domain samples of the DFT pair. Moreover, the elements of  $\mathbf{X}$  will be transmitted serially. Additionally, the channel is assumed to be a non-fading, additive white Gaussian noise channel with a Doppler shift due to mobile movement.

Mathematically, the output of the  $N_c$ -point IDFT can be described as:

$$X_n = \sum_{m=0}^{N_c-1} b_m e^{j2\pi \frac{nm}{N_c}}, \quad (3.37)$$

where  $b_m$  is the binary input data sequence with  $b_m = \pm\sqrt{E_s}$ , where  $E_s = E[b_k^2]$  is the energy per data symbol.

Assume the channel, due to mobile movement, introduces a Doppler shift that in combination with a possible mismatch between the transmitter and receiver carrier frequencies introduces a normalized frequency offset  $\varepsilon$ , where the normalization is

with respect to the subcarrier spacing. Compensating for the frequency offset by an estimate of this offset,  $\hat{\varepsilon}$ , will result in a residual frequency offset of  $\varepsilon - \hat{\varepsilon}$ .

Using the definition of the residual frequency offset, the output of the DFT at subcarrier  $k$  is given by (see also appendix C):

$$\begin{aligned} z_k &= \frac{1}{N_c} \sum_{l=0}^{N_c-1} X_l e^{-j\frac{2\pi lk}{N_c}} e^{j\frac{2\pi l\varepsilon}{N_c}} e^{-j\frac{2\pi l\hat{\varepsilon}}{N_c}} + \xi_k \\ &= \frac{1}{N_c} \sum_{m=0}^{N_c-1} b_m \sum_{l=0}^{N_c-1} e^{j\frac{2\pi l}{N_c}(m-k+(\varepsilon-\hat{\varepsilon}))} + \xi_k, \end{aligned} \quad (3.38)$$

where  $\xi_k$  is the complex Gaussian additive noise component with variance  $\sigma_\xi^2$  for both the in-phase and quadrature component. After some goniometric manipulations  $z_k$  can be expressed as:

$$z_k = \sum_{m=0}^{N_c-1} s(m-k)b_m + \xi_k, \quad (3.39)$$

where  $s(m-k)$  is defined as,

$$s(m-k) = \frac{\sin(\pi(\varepsilon - \hat{\varepsilon}))e^{j\pi(\varepsilon - \hat{\varepsilon})}}{N_c} \left( \cot \left( \frac{\pi(m-k+(\varepsilon - \hat{\varepsilon}))}{N_c} \right) - j \right). \quad (3.40)$$

The output of the DFT can also be written in matrix form as

$$\mathbf{z} = \mathbf{S}^T \mathbf{b} + \boldsymbol{\xi}, \quad (3.41)$$

where the subcarrier cross-correlation matrix  $\mathbf{S}$  is an  $N_c \times N_c$  matrix defined as

$$\mathbf{S} = \begin{bmatrix} s(0) & s(1) & s(2) & \dots & s(N_c-1) \\ s(-1) & s(0) & s(1) & \dots & s(N_c-2) \\ s(-2) & s(-1) & s(0) & & \vdots \\ \vdots & & & \ddots & \vdots \\ s(-N_c+1) & s(-N_c+2) & \dots & \dots & s(0) \end{bmatrix}^T. \quad (3.42)$$

### 3.2.2 Frequency Offset Calculation

In this section a formula is derived to determine the residual frequency offset  $\varepsilon - \hat{\varepsilon}$  based on the samples  $z_k$  at the output of the DFT. The matrix  $\mathbf{C}_z$  is defined as,

$$\mathbf{C}_z = E [\mathbf{z}\mathbf{z}^T]. \quad (3.43)$$



where  $E$  denotes the expectation operator. This definition differs from the covariance matrix  $\mathbf{R}_z = E[\mathbf{z}\mathbf{z}^H] = \mathbf{I}$ , which provides no information about the frequency offset. Utilizing the definition of  $\mathbf{C}_z$  given in equation (3.43), the element of  $\mathbf{C}_z$  at the  $k^{\text{th}}$  row and  $l^{\text{th}}$  column is defined as,

$$c_{kl} = E[z_k z_l], \quad (3.44)$$

where  $E[\xi_k \xi_l] = 0 \forall k, l$  was used.

Assuming the data and noise are uncorrelated  $c_{kl}$  becomes:

$$\begin{aligned} c_{kl} &= E \left[ \left( \frac{1}{N_c} \sum_{m=0}^{N_c-1} b_m \sum_{n=0}^{N_c-1} e^{j \frac{2\pi n}{N_c} (m-k+(\varepsilon-\hat{\varepsilon}))} \right) \left( \frac{1}{N_c} \sum_{t=0}^{N_c-1} b_t \sum_{u=0}^{N_c-1} e^{j \frac{2\pi u}{N_c} (t-l+(\varepsilon-\hat{\varepsilon}))} \right) \right] \\ &= \frac{1}{N_c^2} \sum_{m=0}^{N_c-1} \sum_{t=0}^{N_c-1} E[b_m b_t] \sum_{n=0}^{N_c-1} \sum_{u=0}^{N_c-1} e^{j \frac{2\pi n}{N_c} (m-k+(\varepsilon-\hat{\varepsilon}))} e^{j \frac{2\pi u}{N_c} (t-l+(\varepsilon-\hat{\varepsilon}))}. \end{aligned} \quad (3.45)$$

The data bits on different subcarriers are assumed uncorrelated such that equation (3.45) can be simplified further:

$$\begin{aligned} c_{kl} &= \frac{1}{N_c^2} \sum_{m=0}^{N_c-1} \sum_{t=0}^{N_c-1} \delta(m-t) E_s \sum_{n=0}^{N_c-1} \sum_{u=0}^{N_c-1} e^{j \frac{2\pi n}{N_c} (m-k+(\varepsilon-\hat{\varepsilon}))} e^{j \frac{2\pi u}{N_c} (t-l+(\varepsilon-\hat{\varepsilon}))} \\ &= \frac{E_s}{N_c^2} \sum_{m=0}^{N_c-1} \sum_{n=0}^{N_c-1} \sum_{u=0}^{N_c-1} e^{j \frac{2\pi m(n+u)}{N_c}} e^{j \frac{2\pi(\varepsilon-\hat{\varepsilon})(n+u)}{N_c}} e^{j \frac{2\pi}{N_c} (-nk-ul)}. \end{aligned} \quad (3.46)$$

First summing over  $m$ ,  $c_{kl}$  becomes:

$$c_{kl} = \frac{E_s}{N_c} \sum_{n=0}^{N_c-1} \sum_{u=0}^{N_c-1} \delta((n+u)_{N_c}) e^{j \frac{2\pi(\varepsilon-\hat{\varepsilon})(n+u)}{N_c}} e^{j \frac{2\pi}{N_c} (-nk-ul)}, \quad (3.47)$$

where  $(.)_{N_c}$  indicates modulo  $N_c$ .

The equality  $\delta((n+u)_{N_c}) = 1$  holds for  $n = u = 0$  as well for  $u = N_c - n$ .

Therefore, when  $n, u \neq 0$  the derivation of  $c_{kl}$  continues as:

$$c_{kl} = \frac{E_s}{N_c} \left( 1 + e^{j2\pi(\varepsilon-\hat{\varepsilon})} \sum_{n=1}^{N_c-1} e^{-j \frac{2\pi}{N_c} (n(k-l)+N_c l)} \right). \quad (3.48)$$

For the diagonal elements of  $\mathbf{C}_z$ , which are essentially  $z_k^2$ , the expression for  $c_{kl}$  can be simplified further using  $k = l$ :

$$c_{kk} = \frac{E_s}{N_c} \left( 1 + e^{j2\pi(\varepsilon-\hat{\varepsilon})} \sum_{n=1}^{N_c-1} e^{-j \frac{2\pi}{N_c} N_c l} \right)$$

$$\begin{aligned}
&= \frac{E_s}{N_c} \left( 1 + e^{j2\pi(\varepsilon - \hat{\varepsilon})} \sum_{n=1}^{N_c-1} 1 \right) \\
&= \frac{E_s}{N_c} \left( 1 + (N_c - 1)e^{j2\pi(\varepsilon - \hat{\varepsilon})} \right). \tag{3.49}
\end{aligned}$$

With a simple transformation equation (3.49) yields the following result for the residual frequency offset  $\varepsilon - \hat{\varepsilon}$ :

$$\varepsilon - \hat{\varepsilon} = \frac{1}{2\pi} \tan^{-1} \left( \frac{N_c \text{Im}\{c_{kk}\}}{N_c \text{Re}\{c_{kk}\} - E_s} \right). \tag{3.50}$$

A similar equation can be derived to calculate the residual frequency offset based on the off-diagonal elements of  $\mathbf{C}_z$ .

### 3.2.3 Frequency Offset Estimation

In the previous section a formula was derived that, for a known matrix  $\mathbf{C}_z$ , yields the exact solution for  $\varepsilon - \hat{\varepsilon}$ . In a practical system, however,  $\mathbf{C}_z$  is not known and a solution has to be based on  $\hat{\mathbf{C}}_z$ , an estimate of  $\mathbf{C}_z$ . It is proposed to use the instantaneous estimate for  $\mathbf{C}_z$  that is based on the sample values at the output of the DFT, as defined by

$$\hat{\mathbf{C}}_z(i) = \mathbf{z}(i) \mathbf{z}^T(i), \tag{3.51}$$

where  $i$  indicates the time index of the OFDM symbol.

Now,  $\hat{\Delta}(i)$  is defined as the estimate of  $\varepsilon - \hat{\varepsilon}$  at time  $i$  based on  $\hat{\mathbf{C}}_z(i)$  such that with  $E_s = 1$  equation (3.50) can be rewritten as:

$$\hat{\Delta}(i) = \frac{1}{2\pi} \tan^{-1} \left( \frac{\text{Im}\{N_c \hat{c}_{kk}(i) - 1\}}{\text{Re}\{N_c \hat{c}_{kk}(i) - 1\}} \right), \tag{3.52}$$

where  $\hat{c}_{kk}(i)$  is the  $k^{\text{th}}$  diagonal element of  $\hat{\mathbf{C}}_z(i)$ .

In order to further simplify the implementation of the algorithm, the arctangent is replaced by its argument in equation (3.52). Moreover, as the result of the arctan operation always lies in the range  $(-\pi/2, \pi/2)$  the algorithm is augmented with a soft limiter that limits at  $-\pi/2$  and  $\pi/2$ . The operation of the soft limiter on an

argument  $\theta$ , denoted as  $sl(\theta)$  can be described by,

$$sl(\theta) = \begin{cases} -\frac{\pi}{2} & \text{if } \theta \leq -\frac{\pi}{2} \\ \theta & \text{if } -\frac{\pi}{2} < \theta < \frac{\pi}{2} \\ \frac{\pi}{2} & \text{if } \theta \geq \frac{\pi}{2}. \end{cases} \quad (3.53)$$

Using the soft limiter operation equation (3.52) can be rewritten as

$$\hat{\Delta}(i) = \frac{1}{2\pi} sl \left( \frac{Im \{N_c \hat{c}_{kk}(i) - 1\}}{Re \{N_c \hat{c}_{kk}(i) - 1\}} \right). \quad (3.54)$$

### 3.2.4 Adaptive Frequency Offset Control

In this section an adaptive algorithm is derived to estimate the normalized frequency offset  $\varepsilon$  based on the estimate of the residual frequency offset,  $\varepsilon - \hat{\varepsilon}$ , derived in the previous section. The derived algorithm is a stochastic gradient algorithm based on minimization of the mean-squared frequency offset error as the cost function  $J$ :

$$J = E [|\hat{\varepsilon} - \varepsilon|^2]. \quad (3.55)$$

Rather than using the mean-squared error, the instantaneous squared error  $J(i)$  is used as an estimate, where

$$J(i) = |\hat{\varepsilon}(i) - \varepsilon|^2 = (\hat{\varepsilon}(i) - \varepsilon)^2. \quad (3.56)$$

The derivative of  $J(i)$  with respect to  $\hat{\varepsilon}$  (the adaptively controlled parameter), results in an instantaneous estimate of the gradient as described by

$$\widehat{\nabla} J(i) = 2[\hat{\varepsilon}(i) - \varepsilon]. \quad (3.57)$$

Applying the instantaneous gradient estimate  $\widehat{\nabla} J(i)$  to a steepest-descent algorithm [47] results in the following recursive relation:

$$\hat{\varepsilon}(i+1) - \varepsilon = \hat{\varepsilon}(i) - \varepsilon + \frac{1}{2}\mu[-\widehat{\nabla} J(i)], \quad (3.58)$$

where  $\mu$  is the step-size parameter.

Substituting for  $\widehat{\nabla}J(i)$  and eliminating  $\varepsilon$  on the left and right hand side of the equation gives

$$\hat{\varepsilon}(i+1) = \hat{\varepsilon}(i) + \mu(\varepsilon - \hat{\varepsilon}(i)). \quad (3.59)$$

In section 3.2.6 the convergence criteria are derived for the recursive equation shown in equation (3.59). Ensemble-averaged learning curves of the algorithm are shown in figure 3.12 for various values of the step-size parameter  $\mu$ . The results displayed in figure 3.12 were obtained for 8 subcarriers ( $N_c = 8$ ) and SNR = 10 dB, with ensemble-averaging over 100 independent trials for each value of  $\mu$ .

Finally, the algorithm is completed by replacing  $\varepsilon - \hat{\varepsilon}(i)$  with its estimate  $\hat{\Delta}(i)$ :

$$\hat{\varepsilon}(i+1) = \hat{\varepsilon}(i) + \mu \hat{\Delta}(i). \quad (3.60)$$

Figure 3.13 shows simulation results for  $\hat{\varepsilon}$  versus  $\varepsilon$  for 8 subcarriers and SNR = 10 dB as well as for a noiseless situation (SNR =  $\infty$ ). Figure 3.14 shows the effect of the algorithm on the constellation of the transmitted signal.

### 3.2.5 Statistical Properties Of The Frequency Offset Estimate

In this section it is shown that the frequency offset estimate is unbiased and an expression for the mean-squared error of the frequency offset estimate is derived. Assuming the algorithm has reached the steady state and the residual frequency offset is small, i.e.  $|\varepsilon - \hat{\varepsilon}| \ll 1/2\pi$ , the arctangent can be replaced by its argument and also  $\exp(-j2\pi(\varepsilon - \hat{\varepsilon})) \approx 1$  as well as  $\mathbf{S} \approx \mathbf{I}$ . Equation (3.50) then becomes:

$$\begin{aligned} \varepsilon - \hat{\varepsilon} &\approx \frac{1}{2\pi} \left( \frac{N_c \text{Im}\{\hat{c}_{kk}\}}{N_c \text{Re}\{\hat{c}_{kk}\} - E_s} \right) \\ &= \frac{1}{2\pi} \left( \frac{N_c \text{Im}\{(\mathbf{s}_k^T \mathbf{b} + \xi_k)^2\}}{N_c \text{Re}\{(\mathbf{s}_k^T \mathbf{b} + \xi_k)^2\} - E_s} \right) \\ &\approx \frac{1}{2\pi} \left( \frac{N_c \text{Im}\{(b_k + \xi_k)^2\}}{N_c \text{Re}\{(b_k + \xi_k)^2\} - E_s} \right), \end{aligned} \quad (3.61)$$

where  $\mathbf{s}_k$  is the  $k^{\text{th}}$  column of  $\mathbf{S}$ .

For a sufficiently high SNR equation (3.61) may be further approximated as follows:

$$\varepsilon - \hat{\varepsilon} \approx \frac{1}{2\pi} \left( \frac{N_c \text{Im} \{2b(k)\xi_k\}}{N_c b_k^2 - 1} \right), \quad (3.62)$$

from which it can be concluded that

$$E[\varepsilon - \hat{\varepsilon}] = 0, \quad (3.63)$$

where it was used that the signal and noise are uncorrelated. Equation (3.62) demonstrates that the estimate is unbiased. A plot of  $\hat{\varepsilon}$  versus  $\varepsilon$  in figure 3.13 confirms that the residual frequency offset estimate is unbiased by simulation.

Using the same assumptions and approximations as above, the variance of  $\varepsilon - \hat{\varepsilon}$  can be found from equation (3.62) as

$$\text{Var}[\varepsilon - \hat{\varepsilon}] = \frac{1}{\pi^2} \frac{N_c^2 \sigma_\xi^2}{(N_c - 1)^2 E_s}. \quad (3.64)$$

Figure 3.15 shows the theoretical result for the variance based on equation (3.64) as well as two cases of simulation results for the variance of  $\hat{\Delta}$ : (1) from equation (3.52) using the arctangent; (2) from equation (3.54) using the soft-limiter.

The variance of the estimate can be further reduced at the expense of increased complexity by averaging over multiple values of  $\hat{\Delta}$ . Each  $\hat{\Delta}$  is based on the squared sample value,  $\hat{c}_{kk}$ , at a single subcarrier (DFT output)  $k$ , where  $k \in \{1, \dots, N_c\}$ . As there are  $N_c$  subcarriers, averaging over  $N_c$  realizations of  $\hat{\Delta}$  is possible, thus reducing the variance by a factor  $N_c$ . Utilizing this averaging the variance can be expressed as

$$\text{Var}[\varepsilon - \hat{\varepsilon}] = \frac{1}{\pi^2} \frac{N_c^2}{(N_c - 1)^2} \frac{\sigma_\xi^2}{N_c E_s}. \quad (3.65)$$

The variance of the maximum likelihood estimate (MLE) of the frequency offset based on the retransmission of an information symbol was reported in [41]:

$$\text{Var}[\hat{\varepsilon}] = \frac{1}{\pi^2} \frac{\sigma_\xi^2}{N E_s}. \quad (3.66)$$

Comparing equation (3.66) with equation (3.65) shows that as the number of subcarriers,  $N_c$ , increases, the variance with averaging approaches the variance of the MLE. Simulation results of these various variances are shown in figure 3.15.

### 3.2.6 Convergence Criteria

In this section convergence criteria are derived. With  $\nu(i) = \hat{\varepsilon}(i) - \varepsilon$  equation (3.59) can be rewritten as:

$$\nu(i+1) = \nu(i) - \mu\nu(i). \quad (3.67)$$

From this it follows that

$$\nu(i+n) = (1-\mu)^n \nu(i). \quad (3.68)$$

Thus, for convergence it is required that

$$|1-\mu| < 1, \quad (3.69)$$

or, in other words,

$$0 < \mu < 2. \quad (3.70)$$

Also, the time constant of convergence,  $\tau$ , can be easily calculated:

$$\tau = \frac{-1}{\ln(|1-\mu|)}, \quad (3.71)$$

or, for  $\mu \ll 1$ :

$$\tau \approx \frac{1}{\mu}. \quad (3.72)$$

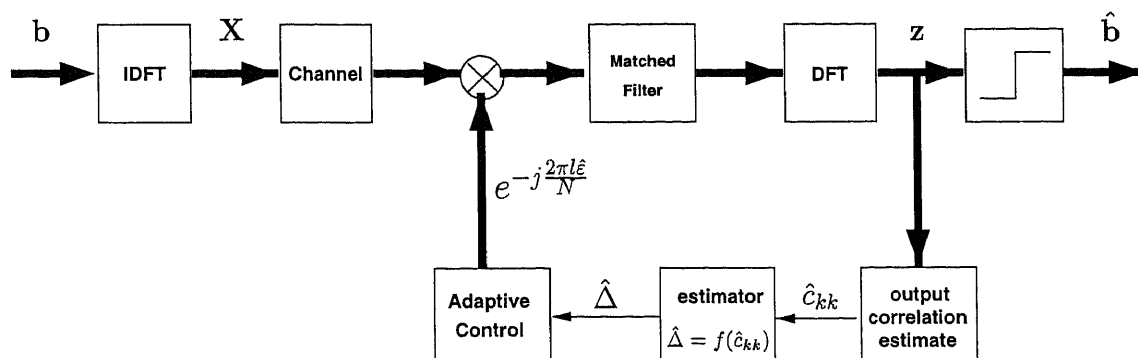


Figure 3.11 Block diagram of an OFDM system with adaptive frequency offset correction.

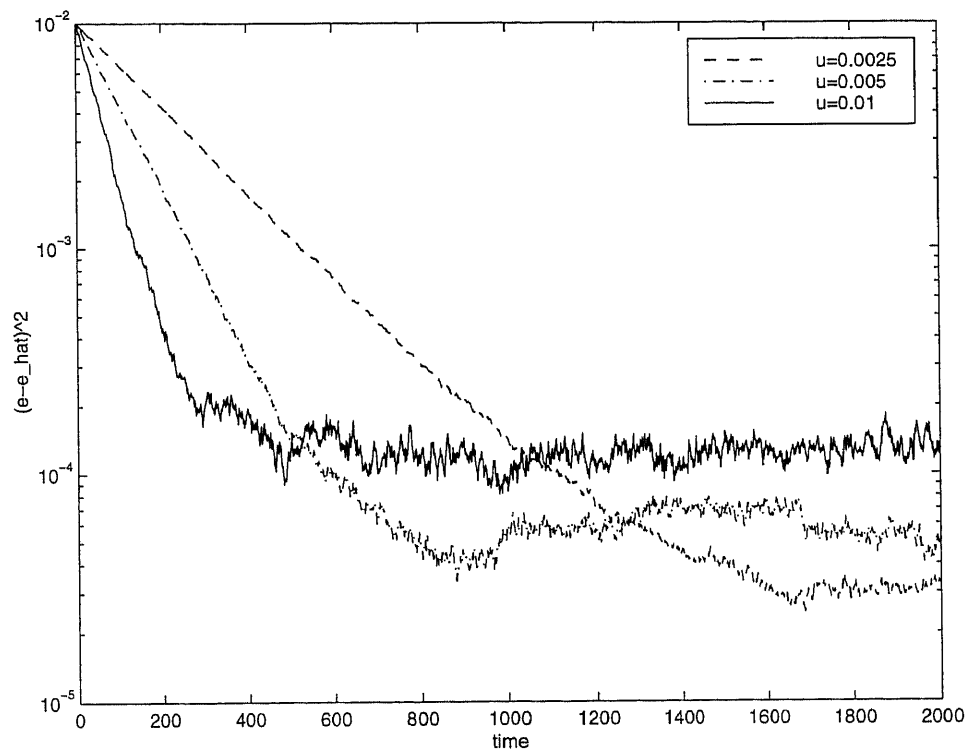
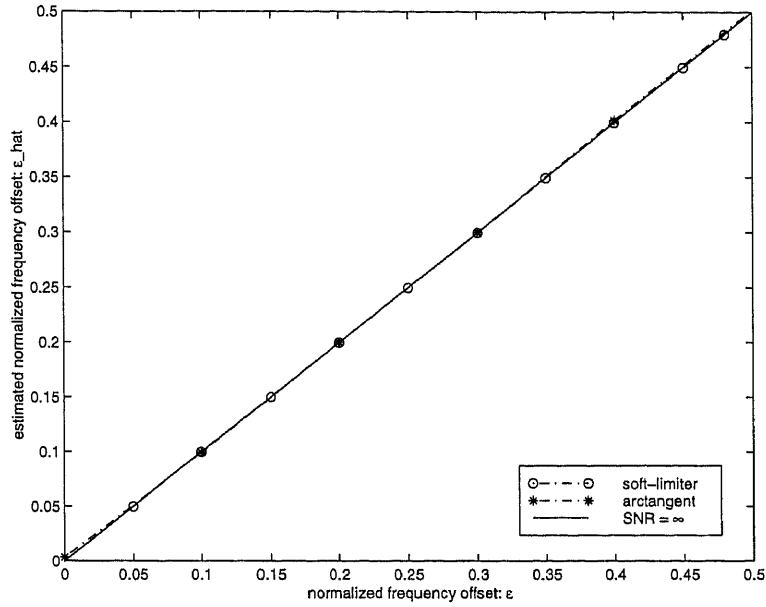
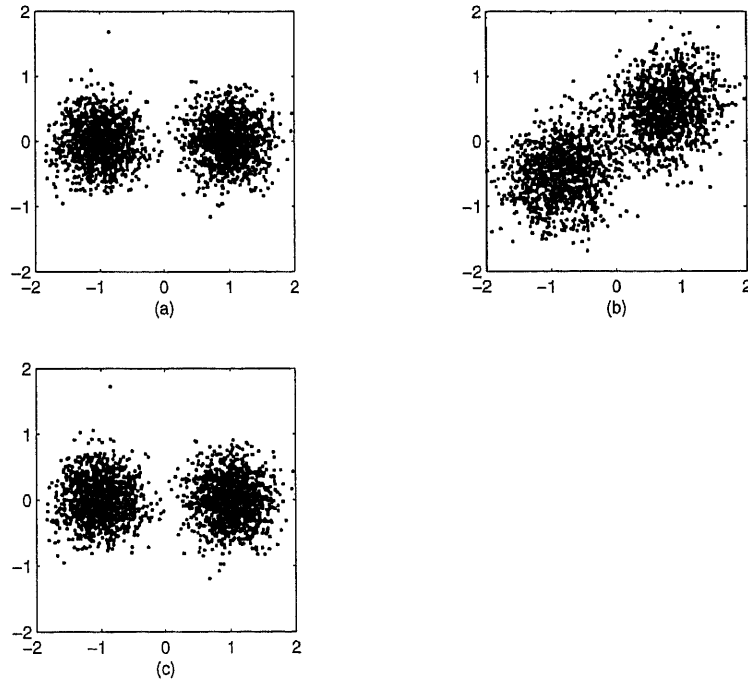


Figure 3.12 Ensemble averaged squared error for  $N_c = 8$  and SNR = 10 dB.



**Figure 3.13** Normalized frequency offset estimate  $\hat{\varepsilon}$  versus actual normalized frequency offset  $\varepsilon$  for  $N_c = 8$  and for  $\text{SNR} = 10$  dB and  $\text{SNR} = \infty$ .



**Figure 3.14** BPSK constellation for  $\varepsilon = 0.2$  and  $\text{SNR} = 10$  dB, (a) without frequency offset, (b) without correction, (c) with frequency offset correction



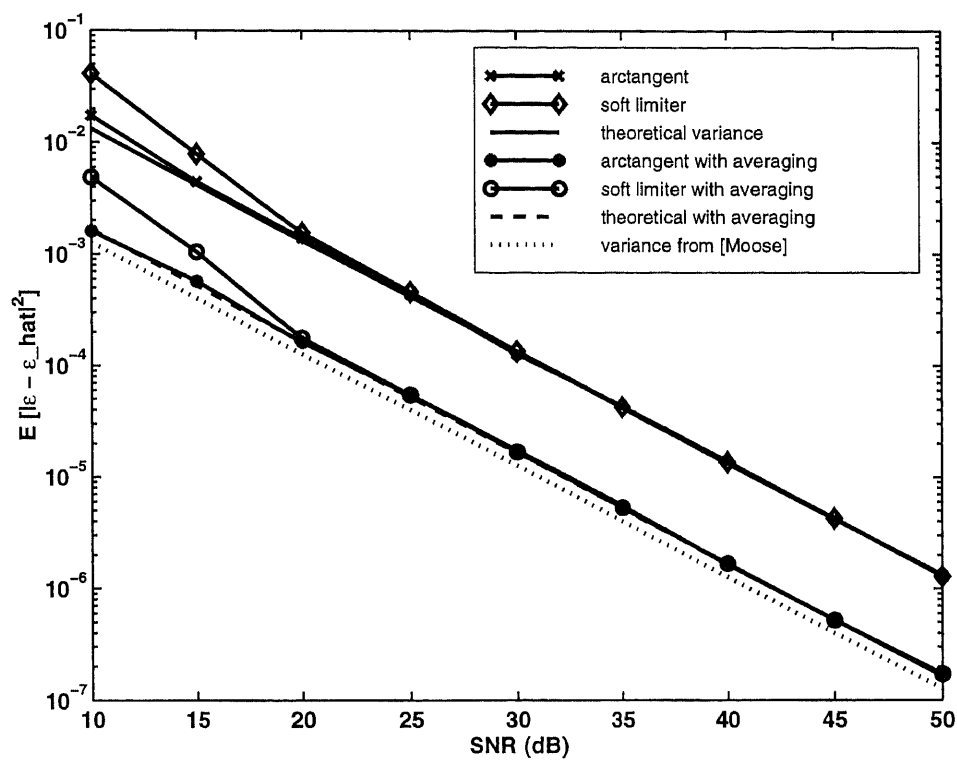


Figure 3.15 Variance of  $\hat{\Delta}$  versus the SNR for  $N_c = 8$ .

## CHAPTER 4

### JOINT MULTIUSER DETECTION AND FREQUENCY OFFSET CORRECTION FOR DOWNLINK MC-CDMA

In this chapter a detector with joint multiuser detection and frequency offset correction is proposed. This detector combines the work on multiuser detection (chapter 2) and frequency offset correction (chapter 3).

#### 4.1 System Model

The system under consideration is a downlink MC-CDMA system consisting of  $N_c$  subcarriers and  $K_a$  active users. The multiplexing-code length is assumed to be equal to the number of subcarriers,  $N_c$ , such that after multicarrier modulation each 'chip' will be transmitted on a different carrier, as described in [14]. Additionally, to increase the system capacity, transmissions aimed at different mobile users may be assigned different powers,  $p_k$ , essentially creating a near-far problem for some users. Mathematically, the multiplexed symbols, carried by the different carriers, can be described as an  $N_c \times 1$  vector  $\mathbf{b}_{ms}$ :

$$\mathbf{b}_{ms} = \sum_{k=1}^{K_a} \sqrt{p_k} b_k \mathbf{c}_k = \mathbf{C} \sqrt{\mathbf{P}} \mathbf{b}, \quad (4.1)$$

where the  $N_c \times 1$  vector  $\mathbf{c}_k$  contains the multiplexing-code of user  $k$ , the  $N_c \times K_a$  matrix  $\mathbf{C} = [\mathbf{c}_1, \mathbf{c}_2, \dots, \mathbf{c}_{K_a}]$  is called the code matrix, the  $K_a \times 1$  vector  $\mathbf{b} = [b(1), b(2), \dots, b(K_a)]^T$  contains the different users' symbols and the  $K_a \times K_a$  matrix  $\mathbf{P} = \text{diag}\{p_1, p_2, \dots, p_{K_a}\}$  is a diagonal matrix.

The subcarriers are separated in frequency by  $\Delta f = 1/T_s$ , where  $T_s$  is the duration of the unmodulated symbols. Each subcarrier is M-QAM modulated such that  $b(l) = b_I(l) + j b_Q(l)$  represents a point in a square M-QAM constellation, with  $b_I, b_Q \in \{-\sqrt{M} + 1, -\sqrt{M} + 3, \dots, -1, 1, \dots, \sqrt{M} - 3, \sqrt{M} - 1\}$ . Thus, the average transmitted power equals  $E_{av} = \frac{2(M-1)E_0}{3}$  per symbol, with  $M$  the number of points

in the signal constellation and  $E_0$  the energy of the constellation point with the lowest amplitude.

The multicarrier modulation can be efficiently implemented by an  $N_c$ -point inverse DFT operation, such that  $\mathbf{X} = \text{IDFT}\{\mathbf{b}_{ms}\}$ . The output of the modulator,  $\mathbf{X}$ , is called an MC-CDMA frame and consists of  $N_c$  samples of duration  $T_s/N_c$ , i.e. the duration of the MC-CDMA frame is  $T_s$ :

$$X_m = \sum_{n=0}^{N_c-1} b_{ms}(n) e^{j \frac{2\pi m n}{N_c}} = \sum_{n=0}^{N_c-1} \sum_{k=1}^{K_a} \sqrt{p_k} b_k c_k(m) e^{j \frac{2\pi m n}{N_c}}. \quad (4.2)$$

It is instructive to think of the elements of  $\mathbf{b}$  as the frequency domain samples and those of  $\mathbf{X}$  as the corresponding time domain samples of the DFT pair. This is also indicated by the parallel-to-serial (P/S) conversion in figure 4.1.

The channel is considered frequency selective with respect to the total bandwidth. The subcarrier bandwidth, however, is assumed to be much smaller than the coherence bandwidth of the channel, such that each subcarrier is subjected to flat Rayleigh fading. Thus, it is assumed that negligible inter-symbol interference occurs such that no guard-time or cyclic prefix is needed. At the output of the channel the signal may then be described as:

$$\mathcal{X}_m = \sum_{n=0}^{N_c-1} a_n b_{ms}(n) e^{j \frac{2\pi m n}{N_c}} = \text{IDFT}\{\mathbf{A} \mathbf{b}_{ms}\}, \quad (4.3)$$

where  $\mathbf{A} = \text{diag}\{a_1, a_2, \dots, a_{N_c}\}$  is a diagonal matrix and where  $a_n$  indicates the amplitude of the  $n^{\text{th}}$  subcarrier. The  $a_n$  are considered Rayleigh distributed random variables and possibly correlated.

The matched filter can be implemented as a quadrature detector, sampled at  $T_s/N_c$ . The complex valued samples are then passed to the  $N_c$ -point DFT for demodulation. As a result of the frequency offset the output of the DFT can be described by:

$$z_m = \frac{1}{N_c} \sum_{l=0}^{N_c-1} \mathcal{X}(l) e^{-j \frac{2\pi l m}{N_c}} e^{j \frac{2\pi l e}{N_c}} + n_m, \quad (4.4)$$

where  $n(m)$  is a zero-mean complex Gaussian additive noise sample with variance  $\sigma_n^2$  and  $\varepsilon$  is the frequency offset normalized by the subcarrier spacing,

$$\varepsilon = \frac{\text{offset}}{\Delta f}. \quad (4.5)$$

Combining the  $N_c$  DFT outputs,  $z(k)$ , into a length  $N_c$  vector  $\mathbf{z}$ , it follows that

$$\mathbf{z} = \mathbf{S}^T \mathbf{A} \mathbf{C} \sqrt{\mathbf{P}} \mathbf{b} + \mathbf{n}, \quad (4.6)$$

where  $\mathbf{n}$  is an  $N_c \times 1$  vector containing i.i.d. zero-mean complex Gaussian additive noise samples with variance  $\sigma_n^2$ , and the  $N_c \times N_c$  subcarrier correlation matrix  $\mathbf{S}$  is defined the same as before:

$$\mathbf{S} = \begin{bmatrix} s(0) & s(-1) & \dots & s(-N_c + 1) \\ s(1) & s(0) & \dots & s(-N_c + 2) \\ \vdots & & \ddots & \vdots \\ s(N_c - 1) & s(N_c - 2) & \dots & s(0) \end{bmatrix}, \quad (4.7)$$

the elements  $\mathbf{S}(n, m) = s(n - m)$  can be derived as (see appendix C):

$$s(n - m) = \frac{\sin(\pi\varepsilon)e^{j\pi\varepsilon}}{N_c} \left\{ \cot \left[ \frac{\pi(n - m + \varepsilon)}{N_c} \right] - j \right\}. \quad (4.8)$$

The matrix  $\mathbf{S}$  has the following properties: (1) it is non-hermitian, i.e.  $\mathbf{S} \neq \mathbf{S}^H$ ; (2) it is orthogonal, i.e.  $\mathbf{S}^H \mathbf{S} = \mathbf{I}$  (or, equivalently, it is unitary as  $\mathbf{S}^H = \mathbf{S}^{-1}$ ); (3) it is a circulant matrix, i.e. the columns (as well as the rows) are shifted versions of each other, as  $s(i) = s(i + nN_c)$  for any integer  $n$ .

In chapter 3, section 3.1, an adaptive decorrelating detector was used to compensate for the effect of a frequency offset in an OFDM system by decorrelating the outputs of the different subcarriers. This approach was based on the assumption that the data at the different subcarriers are uncorrelated, which is valid for OFDM but not for MC-CDMA. Therefore, the DFT outputs are, instead, first multiplied with the transpose of the code matrix  $\mathbf{C}$  in order to demultiplex the received signal and generate the different users' symbols for detection. The symbols of the different

users were originally uncorrelated and hence it is suggested that a decorrelating detector may be used to separate the different users' signals. The demultiplexed signal may be described as:

$$\begin{aligned} \mathbf{x} &= \mathbf{C}^T \mathbf{z} = \mathbf{C}^T \mathbf{S}^T \mathbf{A} \mathbf{C} \sqrt{\mathbf{P}} \mathbf{b} + \boldsymbol{\xi} \\ &= \mathbf{P}'_{sc} \sqrt{\mathbf{P}} \mathbf{b} + \boldsymbol{\xi}, \end{aligned} \quad (4.9)$$

where  $\boldsymbol{\xi} = \mathbf{C}^T \mathbf{n}$  is a zero-mean Gaussian noise vector with covariance matrix  $\mathbf{R}_{\boldsymbol{\xi}} = \sigma_n^2 \mathbf{C}^T \mathbf{C} = \sigma_n^2 \mathbf{P}_c$  and where  $\mathbf{P}'_{sc} = \mathbf{C}^T \mathbf{S}^T \mathbf{A} \mathbf{C}$  is the conditional (on  $\mathbf{A}$ ) code and subcarrier correlation matrix.

Ignoring the noise contribution, equation (2.12) can be expanded as follows for the first user ( $k = 1$ ):

$$x_1 = \underbrace{b_1 s(0) \mathbf{c}_1^T \mathbf{A} \mathbf{c}_1}_{\text{I}} + \underbrace{b_1 \sum_{i=1}^{M-1} s(i) \mathbf{c}_1^T (\mathbf{A} \mathbf{c}_1)^{(i)}}_{\text{II}} + \underbrace{\sum_{k=2}^K b_k \sum_{i=0}^{M-1} s(i) \mathbf{c}_1^T (\mathbf{A} \mathbf{c}_k)^{(i)}}_{\text{III}} \quad (4.10)$$

where the superscript  $(i)$  indicates an upward circular shift of a vector over  $i$  positions, which is a result of the circulant property of the matrix  $\mathbf{S}$ . Moreover, the following parts can be identified: (I) the desired symbol with a rotation as a result of  $s(0)$ ; (II) an interference term dubbed self-interference as it results from non-zero correlation between shifted versions of the desired user's code; (III) multiuser interference.

As has been stated previously, the presence of a frequency offset results in inter-carrier interference. Equation (4.9) implies that as a result of the demultiplexing process, the ICI results in additional interference from the desired user due to non-zero correlation between shifted versions of its code, as well as in additional multiuser interference.

## 4.2 Conventional Decorrelator

Decorrelating detectors have been used to implement near-far resistant detectors for DS-CDMA [46] as well as MC-CDMA [25, 26, 48] (see also chapter 2). For the

latter it was assumed that no frequency offset exists, such that  $\mathbf{S} = \mathbf{I}$  and only multiuser interference (MUI) is present. In the presence of a frequency offset there will be inter-carrier interference (ICI) in addition to the MUI. Moreover, the received symbol constellation will be rotated as can be seen in figure 4.3(b).

The linear multiuser decorrelating detector uses the inverse of the code-cross correlation matrix to completely separate the users' signals. For an MC-CDMA system in the presence of a frequency offset, a joint decorrelating detector (JDD) can be defined that performs joint multiuser detection and frequency offset correction. Hence, the JDD is defined as the inverse of  $\mathbf{P}'_{sc}$ . The output of the JDD then becomes:

$$\tilde{\mathbf{y}} = (\mathbf{P}'_{sc})^{-1}\mathbf{x} = \sqrt{\mathbf{P}}\mathbf{b} + \boldsymbol{\zeta}, \quad (4.11)$$

where  $\boldsymbol{\zeta} = (\mathbf{P}'_{sc})^{-1}\boldsymbol{\xi}$  is a zero-mean Gaussian noise vector with covariance matrix  $\mathbf{R}_{\boldsymbol{\zeta}} = \sigma_n^2(\mathbf{P}'_{sc})^{-1}\mathbf{P}_c(\mathbf{P}'_{sc})^{-1}$ .

The following two observations can be made linking this chapter to chapter 2:

1. When no frequency offset exists ( $\mathbf{S} = \mathbf{I}$ ) the conditional code and subcarrier cross-correlation matrix reduces to the conditional code cross-correlation matrix  $\mathbf{P}'_c$ .
2. When the channel is non-faded AWGN and no frequency offset exists ( $\mathbf{A} = \mathbf{I}$  and  $\mathbf{S} = \mathbf{I}$ ) the conditional code and subcarrier cross-correlation matrix reduces to the code cross-correlation matrix  $\mathbf{P}_c$ .

### 4.3 Adaptive Decorrelating Detector

The adaptive detector used in chapter 3, section 3.1 was implemented in two stages. The first stage decorrelates the subcarriers, whereas the second stage performs a decorrelation of the in-phase and quadrature components, effectively rotating the constellation back to its original orientation. In this section it will be shown that this two stage approach can also be applied to MC-CDMA to perform joint multiuser

detection and frequency offset correction. The two stage implementation is shown in figure 4.2, whereas in figure 4.1 the two stages have been combined into a single matrix  $\widetilde{\mathbf{V}}$ . The equivalence of the two representations is shown later in this section.

Applying the first decorrelation stage, using the  $K_a \times K_a$  matrix  $\mathbf{V}$ , the output  $\mathbf{y}$  becomes

$$\begin{aligned} \mathbf{y} &= \mathbf{V}^H \mathbf{x} = \mathbf{V}^H \mathbf{C}^T \mathbf{S}^T \mathbf{A} \mathbf{C} \sqrt{\mathbf{P}} \mathbf{b} + \boldsymbol{\zeta} \\ &= \mathbf{V}^H \mathbf{P}'_{sc} \sqrt{\mathbf{P}} \mathbf{b} + \boldsymbol{\zeta}, \end{aligned} \quad (4.12)$$

where  $\boldsymbol{\zeta} = \mathbf{V}^H \boldsymbol{\xi}$ . Also,  $\mathbf{V} = \mathbf{I} - \mathbf{W}$ , where  $\mathbf{W}$  is a matrix with zeros on the diagonal, to preserve the desired signal, and complex valued off-diagonal elements.

The so-called *decorrelating weights* can be derived based on the decorrelation criterion  $E[y(k)\mathbf{b}_k] = 0$ , where  $\mathbf{b}_k$  is the vector  $\mathbf{b}$  without the  $k^{\text{th}}$  element. Using these decorrelating weights will result in the same performance as the conventional decorrelator. Without loss of generality the decorrelating weights will be derived for user 1 ( $k = 1$ ) under the assumption that the different users' data is uncorrelated:

$$\begin{aligned} E[y_1 \mathbf{b}_1] &= E[x_1 \mathbf{b}_1 - \mathbf{w}_1^H \mathbf{x}_1 \mathbf{b}_1] \\ &= E[(\mathbf{c}_1^T \mathbf{S}^T \mathbf{A} \mathbf{C} \sqrt{\mathbf{P}} \mathbf{b}) \mathbf{b}_1 - \mathbf{w}_1^H (\mathbf{C}_1^T \mathbf{S}^T \mathbf{A} \mathbf{C} \sqrt{\mathbf{P}} \mathbf{b}) \mathbf{b}_1] \\ &= \sqrt{\mathbf{P}_1} (\mathbf{C}_1^T \mathbf{A} \mathbf{S} \mathbf{c}_1 - \mathbf{C}_1^T \mathbf{A} \mathbf{S} \mathbf{C}_1 \mathbf{w}_1^*), \end{aligned} \quad (4.13)$$

where  $*$  indicates the complex conjugate. Equating this expression to zero, the *decorrelating weights*  $\mathbf{w}_1$ , or, in general,  $\mathbf{w}_k$  can be derived:

$$\mathbf{w}_k = (\mathbf{C}_k^T \mathbf{A} \mathbf{S}^* \mathbf{C}_k)^{-1} \mathbf{C}_k^T \mathbf{A} \mathbf{S}^* \mathbf{c}_k = (\mathbf{P}'_{sc_k})^{-1} \boldsymbol{\rho}'_{sc_k}, \quad (4.14)$$

where  $\mathbf{P}'_{sc_k}$  is  $\mathbf{P}'_{sc}$  without the  $k^{\text{th}}$  row and column and  $\boldsymbol{\rho}'_{sc_k}$  is the  $k^{\text{th}}$  column of  $\mathbf{P}'_{sc}$  without the  $k^{\text{th}}$  element.

Using the decorrelating weights, and ignoring the additive Gaussian noise contribution, the output of the decorrelator for  $k = 1$  becomes

$$y_1 = x_1 - \mathbf{w}_1^H \mathbf{x}_1$$

$$\begin{aligned}
&= (\mathbf{c}_1^T \mathbf{S}^T \mathbf{A} \mathbf{c}_1 - \mathbf{c}_1^T \mathbf{S}^T \mathbf{A} \mathbf{C}_1 (\mathbf{C}_1^T \mathbf{S}^T \mathbf{A} \mathbf{C}_1)^{-1} \mathbf{C}_1^T \mathbf{S}^T \mathbf{A} \mathbf{c}_1) \sqrt{p_1} b_1 \\
&= \alpha_1 \sqrt{p_1} b_1,
\end{aligned} \tag{4.15}$$

where  $\alpha_1$ , or in general  $\alpha_k$ , is a complex constant that represents the rotation of symbol  $b_k$  and depends on the normalized frequency offset  $\varepsilon$ , the channel matrix  $\mathbf{A}$ , the number of active users,  $K_a$ , and the user number,  $k$ . Due to the rotation, correlation exists between the in-phase (I) and quadrature (Q) components of the signal. The constellation, at the output of the first decorrelator stage is shown in 4.3(c) for 7 subcarriers ( $N_c = 7$ ), 4 active users ( $K_a = 4$ ), a normalized frequency offset of 0.25 ( $\varepsilon = 0.25$ ) and SNR = 12 dB. This figure clearly shows the rotation as a result of  $\alpha_k$ . Also, comparison of figure 4.3(b) with figure 4.3(c) shows that the constellation points after the first decorrelation stage are slightly more confined around the 'actual' constellation points.

The I and Q components of each user may be decorrelated, assuming they were originally uncorrelated and assuming the rotation is small enough (approximately satisfied when  $\text{angle}\{\alpha_k\} < \pi/4$  rad). The decorrelation is accomplished using a linear transformation  $\mathbf{V}_{\text{rot}_k}$  at each output of the first decorrelation stage (see figure 4.2). In order to find the solution for the elements of  $\mathbf{V}_{\text{rot}_k}$  a vector  $\boldsymbol{\beta}_k$  is defined:

$$\boldsymbol{\beta}_k = \begin{bmatrix} \text{Re}\{\alpha_k b_k\} \\ \text{Im}\{\alpha_k b_k\} \end{bmatrix}. \tag{4.16}$$

The output of the I-Q decorrelator then becomes,

$$\begin{bmatrix} \text{Re}\{\tilde{y}(k)\} \\ \text{Im}\{\tilde{y}(k)\} \end{bmatrix} = \mathbf{V}_{\text{rot}_k}^T \boldsymbol{\beta}_k = \begin{bmatrix} 1 & -w_{r21_k} \\ -w_{r12_k} & 1 \end{bmatrix} \begin{bmatrix} \text{Re}\{\alpha_k b_k\} \\ \text{Im}\{\alpha_k b_k\} \end{bmatrix}. \tag{4.17}$$

From this equation the weight values that cancel the effect of  $\alpha_k$  can easily be derived:

$$w_{r12_k} = -w_{r21_k} = \frac{\text{Im}\{\alpha_k\}}{\text{Re}\{\alpha_k\}}. \tag{4.18}$$

Using these weight values effectively rotates the constellation back to its original orientation as shown in figure 4.3(d).



In order to show the equivalence of the two stage implementation shown in figure 4.2 and the one stage of figure 4.1, a complex constant  $\gamma_k$  is defined. Let  $\gamma_k$  be such that  $\nu_k = \gamma_k^* \alpha_k$ , where  $\nu_k$  is real ( $\nu_k \in \mathbb{R}$ ). This can be assured by choosing

$$\gamma_k = 1 + jw_{r12_k} = 1 + j \frac{Im\{\alpha_k\}}{Re\{\alpha_k\}}. \quad (4.19)$$

Now, let  $\mathbf{\Gamma} = \text{diag}\{\gamma_1, \gamma_2, \dots, \gamma_K\}$  be a  $K_a \times K_a$  diagonal matrix. Then, the equivalence of the one stage and two stage implementation can be understood as follows:

$$\widetilde{\mathbf{V}} = \mathbf{V}\mathbf{\Gamma}. \quad (4.20)$$

The previously calculated solutions for  $\mathbf{V}$  and  $\mathbf{V}_{\text{rot}}$  are dependent on the unknown quantity  $\varepsilon$ , the normalized frequency offset, and the channel realizations. Here it is suggested to use the bootstrap algorithm to implement an adaptive version of the joint multiuser detection and frequency offset correction scheme, such that knowledge of  $\varepsilon$  and  $\mathbf{A}$  is not required. The bootstrap algorithm [45] has been successfully applied to multiuser detection in DS-CDMA [46] and MC-CDMA [25, 26, 48] as well as to frequency offset correction for OFDM [49].

The adaptive algorithm is implemented in two stages (compare figure 4.2). The first stage uses the complex bootstrap algorithm [46], which efficiently implements the bootstrap algorithm for the decorrelation of complex signals. The recursive update equation of the complex bootstrap algorithm is as follows:

$$\mathbf{w}_k(i+1) = \mathbf{w}_k(i) + \mu y_k^* \text{csgn}(\mathbf{y}_k), \quad (4.21)$$

where  $\mu$  is the step-size parameter of the adaptation process,  $i$  denotes the time index of the MC-CDMA frame, which is equal to the user's symbol index. Additionally, as before,  $\text{csgn}(\cdot)$  is defined as  $\text{sgn}(Re\{\cdot\}) + j\text{sgn}(Im\{\cdot\})$

The second stage decorrelates the in-phase and quadrature components of each output of the first decorrelation stage. As this is essentially a decorrelation

of two M-PAM signals, only a  $2 \times 2$  real bootstrap decorrelator is required (see also section 3.1.5).

#### 4.4 Wiener Filter

In this section the Wiener filter solution for joint multiuser detection and frequency offset correction is derived, which is based on the minimum mean-square error criterion. In order to derive this linear optimum filter the vector  $\mathbf{x}$ , as defined previously in equation (4.9), is assumed as the input to the  $K_a \times K_a$  Wiener filter. The desired response  $\mathbf{d}$  equals the  $K_a \times 1$  vector  $\mathbf{b}$  weighted by the transmit powers, i.e.  $\mathbf{d} = \sqrt{\mathbf{P}}\mathbf{b}$ .

Let the  $K_a \times K_a$  conditional (on  $\mathbf{A}$ ) correlation matrix of  $\mathbf{x}$ , the input to the Wiener filter, be denoted by  $\mathbf{R}'_x$ :

$$\begin{aligned} \mathbf{R}'_x &= E[\mathbf{x}\mathbf{x}^H|\mathbf{A}] \\ &= \mathbf{C}^T \mathbf{S}^T \mathbf{A} \mathbf{C} \mathbf{P} \mathbf{C}^T \mathbf{S}^* \mathbf{A} \mathbf{C} + \sigma_n^2 \mathbf{C}^T \mathbf{C} \\ &= \mathbf{P}'_{sc} \mathbf{P} \mathbf{P}'_{sc} + \sigma_n^2 \mathbf{P}_c. \end{aligned} \quad (4.22)$$

Additionally, let  $\psi'_k$  denote the conditional (on  $\mathbf{A}$ ) cross-correlation vector between  $\mathbf{x}$  and the desired response of user  $k$ ,  $d_k$ :

$$\psi'_k = E[\mathbf{x}d_k^*|\mathbf{A}] = \mathbf{C}^T \mathbf{S}^T \mathbf{c}_k p_k, \quad (4.23)$$

where  $\psi'_k$  is the  $k^{\text{th}}$  column of  $\mathbf{P}'_{sc}$ .

Using these definitions, the Wiener-Hopf equations [47] may be expressed as:

$$\mathbf{R}'_x \boldsymbol{\omega}_k = \psi'_k, \quad (4.24)$$

where  $\boldsymbol{\omega}_k$  is the optimum weight vector. Clearly, the Wiener-Hopf equations can be solved under the assumption that  $\mathbf{R}_x$  is non-singular:

$$\boldsymbol{\omega}_k = \mathbf{R}'_x{}^{-1} \psi'_k. \quad (4.25)$$

The  $K_a \times K_a$  Wiener filter can then be defined as:

$$\mathbf{\Omega} = [\omega_1, \omega_2, \dots, \omega_{K_a}]. \quad (4.26)$$

#### 4.5 Discussion and Results

Results are presented for an MC-CDMA system in a non-faded AWGN channel with seven subcarriers ( $M = 7$ ), four active users ( $K_a = 4$ ), and a normalized frequency offset of 20% ( $\epsilon = 0.2$ ). In figures 4.4, 4.5 and 4.6 the bit error rate (BER) of several detectors is shown for a signal-to-interference ratio (SIR) of -10 dB, 0 dB and 10 dB respectively. The SIR is defined as the ratio of the desired user's signal power and any of the interfering users. Assuming the first user is the desired one ( $k = 1$ ) the SIR is defined as:

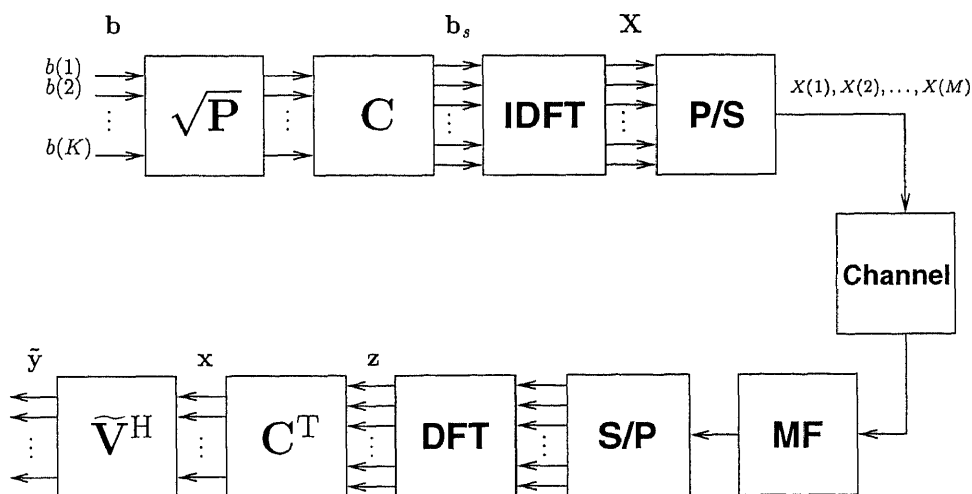
$$\text{SIR} = \frac{p_1}{p_i}, \quad i = 2, \dots, K_a. \quad (4.27)$$

Figure 4.4 shows the bit error rate of the detectors under consideration when  $\text{SIR} = -10$  dB. It can be seen that the performance of the single user detector, which simply performs a hard-decision after the demultiplexing stage, is dominated by the strong multiuser interference. Even the absence of a frequency offset hardly improves the performance of the SUD. Applying the first stage of the joint multiuser detection and frequency offset correction scheme, which decorrelates the different users but does not perform I-Q decorrelation, i.e. it does not rotate the constellation, greatly improves the performance over the SUD. Applying both stages of the joint detector results in a performance that is very close—less than 1 dB difference—to the single user bound (SUB). The SUB is expressed by the probability of bit error ( $P_e$ ) of 4-QAM. Additionally, the figure shows that the performance improvement of the second stage over the first stage is approximately 7 dB. Moreover, it can also be seen that the performance of the joint detector is approximately equal to the performance of the Wiener filter.

Figure 4.5 shows the performance of the various detectors for  $SIR = 0$  dB. Compared with figure 4.4 the SUD's performance has considerably improved for higher levels of the signal-to-noise ratio due to the reduced level of multiuser interference. The curve, however, still flattens out as there is still considerable MUI remaining. The increase of the MUI as a result of the frequency offset can be clearly seen when the SUD with no frequency offset ( $\varepsilon = 0$ ) and the SUD are compared.

Comparing figure 4.5 and 4.4 shows that the performance after the first stage is not dependent on the signal-to-interference ratio. This is as expected because the first stage decorrelates the different user's outputs, thus making each user's output independent of the other user's powers.

Figure 4.6 shows the performance of the different detectors for  $SIR = 10$  dB. Now, as the desired signal is much stronger than the interfering signals the difference between the SUD and the first stage is only about 3 dB. Additionally, for  $SIR = 10$  dB, the performance of the SUD without frequency offset is approximately equal to the joint detector as well as the Wiener filter and is also very close to the single user bound.



**Figure 4.1** Block diagram of a downlink MC-CDMA system with joint multiuser detection and frequency offset correction

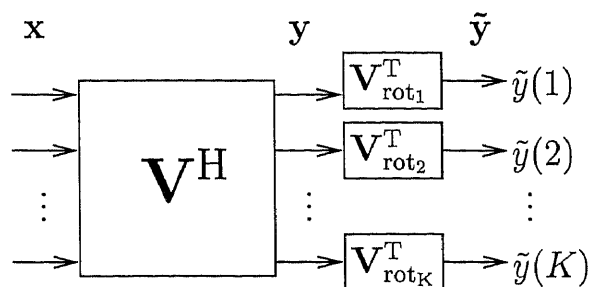


**Figure 4.2** Two stage implementation for joint multiuser detection and frequency offset correction

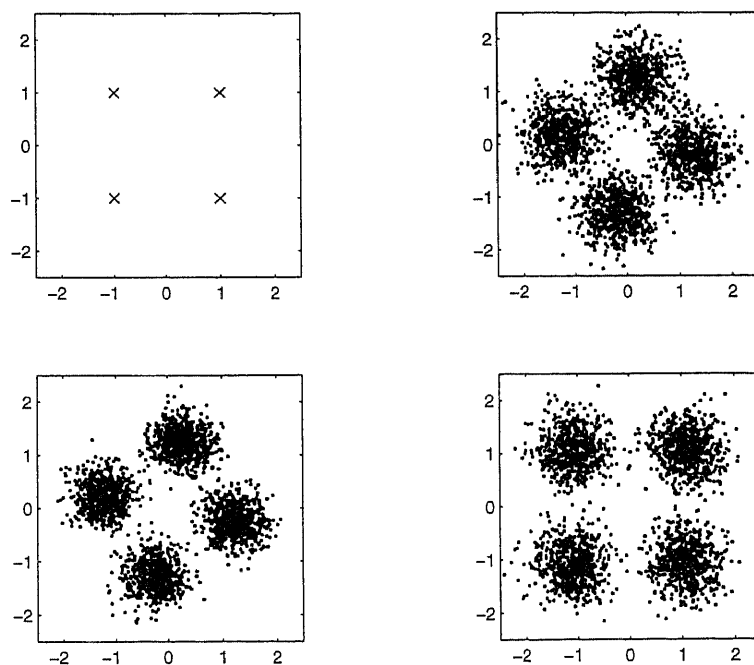


**Figure 4.3** Constellations of 4-QAM transmission for  $N_c = 7$ ,  $K_a = 4$ ,  $\varepsilon = 0.25$  and SNR = 12 dB, (a) transmitted constellation, (b) constellation after  $\mathbf{C}^T$ , (c) constellation after  $\mathbf{V}$ , (d) constellation after  $\tilde{\mathbf{V}}$

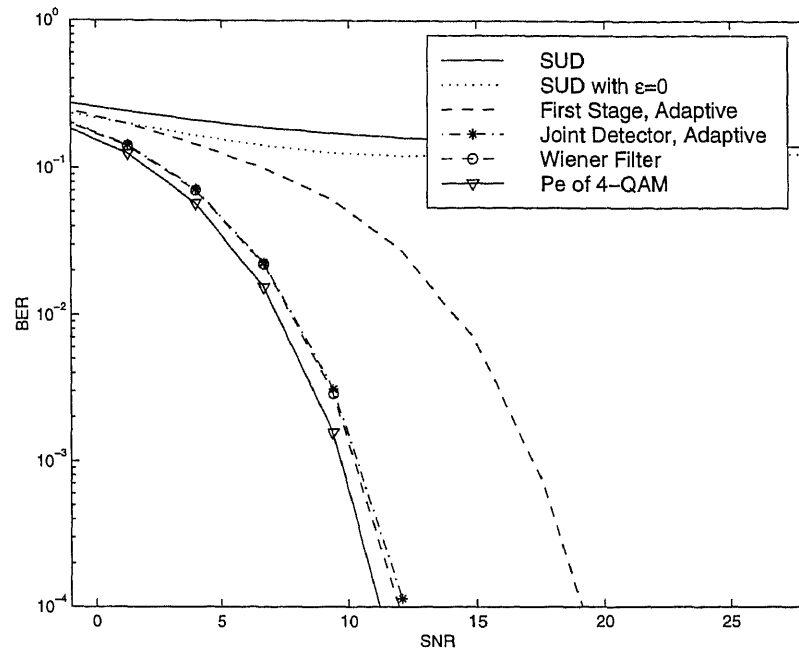


Figure 4.4 BER versus SNR for  $N_c = 7$ ,  $K_a = 4$ ,  $\varepsilon = 0.2$  and  $\text{SIR} = -10$  dB

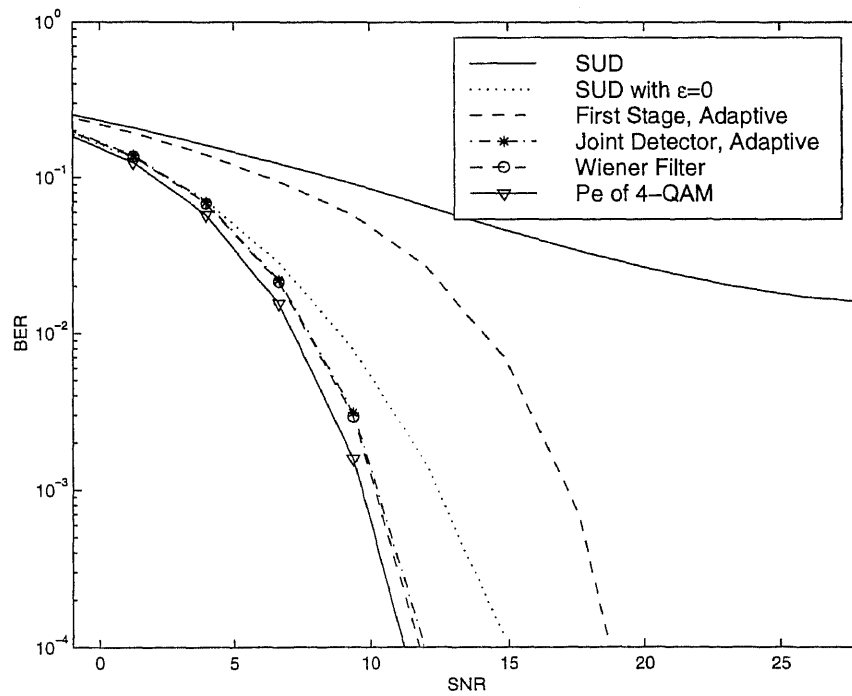
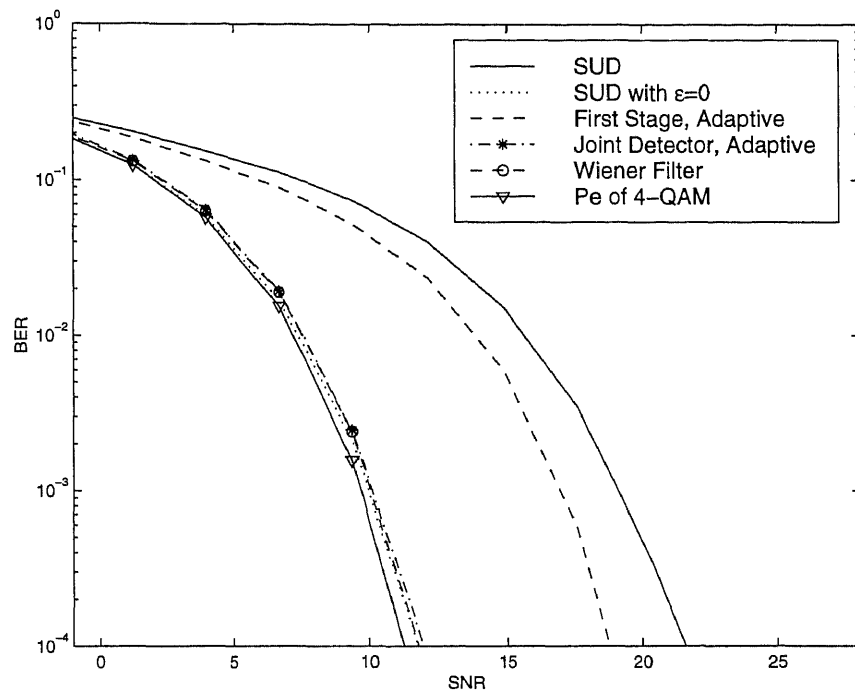


Figure 4.5 BER versus SNR for  $N_c = 7$ ,  $K_a = 4$ ,  $\varepsilon = 0.2$  and  $\text{SIR} = 0$  dB



**Figure 4.6** BER versus SNR for  $N_c = 7$ ,  $K_a = 4$ ,  $\varepsilon = 0.2$  and  $SIR = 10$  dB

## CHAPTER 5

### CONCLUSIONS

#### 5.1 Adaptive Multiuser Detection for MC-CDMA

Multiuser detection techniques have become an important method to improve the performance of multiple access systems such as multicarrier code division multiple access (MC-CDMA). However, the complexity of most multiuser detection techniques might prohibit its application in a mobile terminal with limited available resources. Additionally, the knowledge requirements of most multiuser detectors, such as which users are active and their codes, might be hard to satisfy in a dynamic multiuser scenario where users continuously enter and leave the network. A reduced complexity multiuser detector was proposed that replaces the bank of matched filters of the full dimensional detector with two filters; one filter matched to the desired user's code and another filter employing a combination of all the interfering users' codes, called the compounded code.

The performance of four different multiuser detectors was shown and compared: the adaptive reduced complexity multiuser detector (ARCD), the reduced complexity decorrelator (RCD), the adaptive full dimensional detector (AFDD), and the full dimensional decorrelator (FDD). Additionally, the performance of these detectors was compared to the single user bound (SUB) and the performance of the single user detector (SUD), also referred to as the conventional matched filter detector. Moreover, the performance was shown for equal gain combining (EGC) and maximal ratio combining (MRC) in a non-faded additive white Gaussian noise (AWGN) channel and a Rayleigh fading channel with and without correlation between the fading parameters at the different subcarriers.

It was determined that in an MC-CDMA system the FDD is dependent on the subcarrier amplitudes, suggesting the use of an adaptive detector.



It was shown that for very strong interfering users ( $\text{ISR} \rightarrow \infty$ ), the adaptive weights of the ARCD and AFDD approach their respective decorrelating weights as was shown in the preceding sections. Consequently, the performance of the ARCD and AFDD approaches the performance of the RCD and FDD respectively, hence this performance may be seen as the asymptotic performance of the adaptive detectors. Both the RCD and FDD are near-far resistant, i.e. their performances are independent of the ISR.

The ARCD and AFDD always outperform the RCD and FDD respectively, as the adaptive detectors inherently utilize knowledge about the signal powers. As a result, the ARCD and AFDD do not completely separate the users' signals, but leave some interference residue. However, because the additive noise is less enhanced there will be an SINR improvement, particularly when the interference power is low. As such the ARCD and AFDD behave similar to MMSE detectors.

In comparing the performance of the RCD with the FDD a trade-off between complexity and performance was shown. The performance difference between these two decorrelators was shown to decrease with an increasing number of active users ( $K_a$ ) as the performance of the FDD worsens, approaching the performance of the RCD. The two decorrelators yield the same performance when the maximum number of users is active. Thus, when the system is heavily loaded the knowledge of the actual active users and their respective codes does not provide additional performance improvement.

A comparison of the ARCD and AFDD reveals again a trade-off between complexity and performance as the AFDD performs better than the ARCD for practically all combinations of the number of active users and ISR levels.

For equal strength desired user and interferers ( $\text{ISR}=0$  dB), it was shown that the ARCD outperforms the RCD for any number of active users. Also, with both EGC and MRC the additional performance loss of an added user decreases as the

number of active users increases. In other words, for a highly loaded system the varying number of active users does not greatly influence the BER of the desired user.

It was shown that the performance of the AFDD with MRC is always better than with EGC. On the other hand, the performance of the ARCD at  $\text{ISR}=0$  dB with EGC is almost always better than with MRC. This can be attributed to the fact that MRC ignores the presence of multiuser interference and thus, for a certain interference level, decreases rather than increases the SINR. Moreover, it is inferred that due to the reduced complexity the ARCD does not have sufficient degrees of freedom to eliminate the increased MUI, whereas the AFDD does.

It was demonstrated that for the i.i.d. Rayleigh fading channel with EGC the size of the AFDD, which depends on the number of active users, has an opposite effects for low and high ISRs. For low ISR, the performance is better when  $K_a$  is higher as it has more degrees of freedom to enhance the performance. For high ISR, however, higher  $K_a$  results in worse performance due to more noise amplification as the weights have converged to the decorrelating weights, resulting in similar performance as the FDD.

Comparing the performance of the ARCD at  $\text{ISR}=0$  dB, in both i.i.d. and correlated Rayleigh fading channels, and for EGC as well as MRC reveals that for both channel types EGC outperforms MRC for all numbers of active users. This is consistent with our previous explanation that MRC does not necessarily improve the SINR when interference is present. Additionally, the ARCD for a low number of active users, performs considerably better in an i.i.d. Rayleigh fading channel than in a correlated Rayleigh fading channel. However, as the number of active users increases the BER for the i.i.d. Rayleigh fading channel increases more rapidly than that of the correlated Rayleigh fading channel. As a result, both channel types have almost equal performance for a high number of active users.

Examining the performance of the FDD in both i.i.d. and correlated Rayleigh fading channels, and for EGC as well as MRC shows that the performance of the FDD in an i.i.d. Rayleigh fading channel is better than in a correlated Rayleigh Fading channel. However, the performance difference between these two channel types becomes smaller for higher  $K_a$ . Additionally, the FDD with MRC always outperforms the FDD with EGC.

## 5.2 Frequency Offset Correction for OFDM

### 5.2.1 Frequency Offset Correction Using an Adaptive Decorrelator

Applying an adaptive decorrelator to an OFDM system operating in the presence of a frequency offset, achieves a significant improvement over the matched filter performance. The adaptive complex decorrelator eliminates the ICI as well as the inter-rail interference, which resulted from a rotation of the constellation. The complexity of the implementation can be considerably reduced by utilizing the circulant property of the matrix  $\mathbf{V}$  that decorrelates the DFT outputs. In addition, the matrix  $\mathbf{V}_{\text{rot}}$  that removes the inter-rail interference by rotating the constellation is the same for each DFT output and contains only one unknown weight. Consequently,  $N_c - 1$  complex weight values and 1 real weight value need to be determined, where  $N_c$  is the number of subcarriers.

Simulations with 4-QAM data symbols in a non-faded AWGN channel showed that the decorrelator achieves the single-carrier 4-QAM performance.

Additionally, in a non-faded AWGN channel, improved performance with respect to an ICI cancelation scheme using a form of repetition coding—thereby halving the bandwidth efficiency—in the frequency domain [40] was shown. Improved performance was also shown with respect to a scheme using frequency domain correlative coding [42]. In particular, for high signal-to-noise-ratios the decor-

relator outperforms the ICI cancelation scheme and correlative coding scheme as the remainder of the ICI dominates the performance.

For instance, when  $\varepsilon = 0.2$  and  $\text{SNR} = 20$  dB the decorrelator performs 2.5 dB better than the ICI cancelation scheme and 6.5 dB better than the correlative coding scheme and 15 dB better than the conventional OFDM detector.

It was established that in a time-variant channel the complex bootstrap algorithm no longer converges when the channel amplitudes change too rapidly. To remedy this problem, an augmented complex bootstrap algorithm was proposed that does not depend on the subcarrier amplitudes. Simulations showed the effectiveness of this new algorithm.

Moreover, in a time-variant channel, it was shown that with the use of the augmented complex bootstrap algorithm for  $\tau_0 = 100, 1000, 1000$  (where  $\tau_0$  is expressed in OFDM-symbols), the BER is close to the optimum BER, achieved by the application of the conventional decorrelator  $\mathbf{S}^*$ . Additionally, it was shown that there is only a small loss in BER due to the use of imperfect channel estimation rather than the use of the actual channel amplitudes.

### 5.2.2 Blind Adaptive Frequency Offset Estimation and Correction

A method for estimating the normalized frequency offset  $\varepsilon$  in an OFDM system which does not sacrifice bandwidth efficiency has been proposed. The frequency offset estimation is derived from the square of the data samples at the output of the DFT. It was shown that the estimate is unbiased and an expression for the variance of the estimate was derived, which was shown to be inversely proportional to the signal-to-noise-ratio. Additionally, it was suggested that the variance could be further reduced by a factor  $N_c$  by averaging over  $N_c$  estimates, where  $N_c$  is the number of subcarriers. With averaging, the variance approaches the variance of the maximum likelihood estimate reported in [41], which was based on the retransmission

of a symbol. Simulation results for the variance were shown and compared with the theoretical values.

Utilizing the proposed method for frequency offset estimation an adaptive frequency offset correction algorithm was developed. The algorithm is basically a stochastic gradient algorithm which minimizes the mean squared frequency offset error, defined as  $E[|\varepsilon - \hat{\varepsilon}|^2]$ . Convergence criteria for the algorithm were derived and ensemble averaged learning curves were shown. Moreover, simulation results for the estimate of the normalized frequency offset versus the actual frequency offset revealed a close match, resulting in a small residual frequency offset.

### 5.3 Joint Multiuser Detection and Frequency Offset Correction for Downlink MC-CDMA

A detector with joint multiuser detection and frequency offset correction was developed based on the application of an adaptive decorrelator with the bootstrap algorithm. The detector was implemented in two stages. The first stage decorrelated the different users' outputs and the second stage decorrelated the in-phase and quadrature components for each user, in effect rotating the received constellation to its original orientation. The equivalence of the two stage and one stage implementation was also shown.

In addition to the adaptive detector the Wiener filter solution for joint multiuser detection and frequency offset correction was derived, which is based on the minimum mean-square error criterion.

Simulation results were presented for an MC-CDMA system with 4-QAM symbols in a non-faded AWGN channel with seven subcarriers ( $N_c = 7$ ), four active users ( $K_a = 4$ ), and a normalized frequency offset of 20% ( $\varepsilon = 0.2$ ) for a signal-to-interference ratio of -10 dB, 0 dB and 10 dB.

The simulation results showed that the adaptive detector performed similar to the Wiener filter, where both performed close to the single user bound.

It was shown that the performance after the first stage is not dependent on the signal-to-interference ratio. This is as expected because the first stage decorrelates the different user's outputs, thus making each user's output independent of the other user's powers.

# APPENDIX A

## CORRELATED RAYLEIGH FADING IN THE FREQUENCY DOMAIN

### A.1 Derivation of the Frequency Correlation Function

A frequency selective Rayleigh faded channel can be represented in the frequency domain by the correlation between the different subcarriers in an MC-CDMA system. In order to introduce correlated fading between the different subcarriers spaced in frequency we derive the formula for the complex valued correlation as a function of frequency separation, rather than the envelope correlation as a function of frequency separation reported in [50].

The channel is assumed to be Wide-Sense Stationary Uncorrelated Scattering [51]. Additionally, it is assumed that the power-delay profile of the channel is exponentially decaying, as given by

$$Q(\tau) = |h(t, \tau)|^2 = \frac{1}{\tau_d} e^{-\tau/\tau_d}, \quad (\text{A.1})$$

where  $h(t, \tau)$  is the complex low-pass channel impulse response (cir) or the input delay-spread function [51]. The rms delay spread,  $\tau_d$ , is defined as the square root of the second central moment of the channel's power-delay profile.

$$\tau_d = \sqrt{\frac{\int_0^\infty (\tau - \bar{\tau})^2 Q(\tau) d\tau}{\int_0^\infty Q(\tau) d\tau}}, \quad (\text{A.2})$$

where  $\bar{\tau}$  is the mean propagation delay, given by

$$\bar{\tau} = \frac{\int_0^\infty \tau Q(\tau) d\tau}{\int_0^\infty Q(\tau) d\tau}. \quad (\text{A.3})$$

The complex low-pass impulse response has a correlation function  $R_h(t, t + \Delta t; \tau, \eta)$  which in the case of a WSSUS channel can be simplified as follows [51]

$$R_h(t, t + \Delta t; \tau, \eta) = P_h(\Delta t, \tau) \delta(\eta - \tau) = Q(\Delta t, \tau), \quad (\text{A.4})$$

where  $Q(\Delta t, \tau)$  is called the delay cross-power spectral density function. For  $\Delta t = 0$ , equation (A.4) reduces to the power-delay profile as shown in equation (A.1).

The time-variant transfer function  $T(f, t)$  has a correlation function which can be similarly simplified for the WSSUS channel, resulting in the time-frequency correlation function as described by

$$R_T(f, f + \Delta f; t, t + \Delta t) = R_T(\Delta f, \Delta t) = R(\Delta f, \Delta t). \quad (\text{A.5})$$

For  $\Delta t = 0$ , equation (A.5) reduces to the frequency correlation function –also called the spaced-frequency correlation function– denoted by  $\rho(\Delta f)$ . The frequency correlation function and the power delay profile are related by the Fourier transform

$$\rho(\Delta f) = \int_0^\infty \frac{1}{\tau_d} e^{-\tau/\tau_d} e^{-j2\pi\Delta f\tau} d\tau, \quad (\text{A.6})$$

where the limits of the integration reflect the possible values for the delay  $\tau$ . Solving this Fourier transform yields the result for the frequency correlation function:

$$\rho(\Delta f) = \frac{1 - j2\pi\tau_d\Delta f}{1 + (2\pi\tau_d\Delta f)^2}. \quad (\text{A.7})$$

A plot of the absolute value of the frequency correlation function as a function of  $\Delta f$  with  $\tau_d$  as a parameter is shown in figure A.1.

## A.2 Generation of Correlated Rayleigh Fading

The approach described in [52] is applied to a multicarrier system to generate correlated fading in the frequency domain. Let  $\Delta f$  be the frequency separation between the subcarriers,  $N_c$  the number of subcarriers, and  $\tau_d$  the delay spread of the channel. Additionally, let  $\boldsymbol{\xi} = [\xi_1, \dots, \xi_{N_c}]^T$  a vector of  $N_c$  zero-mean uncorrelated complex Gaussian random variables with correlation matrix  $R_\xi$ :

$$R_\xi = E[\boldsymbol{\xi}\boldsymbol{\xi}^H] = 2\sigma_\xi^2 \mathbf{I}_{N_c}, \quad (\text{A.8})$$

where  $\sigma_\xi^2 = 1/2$  is the variance for both the real and imaginary parts and is chosen such that the total variance is normalized to unity.



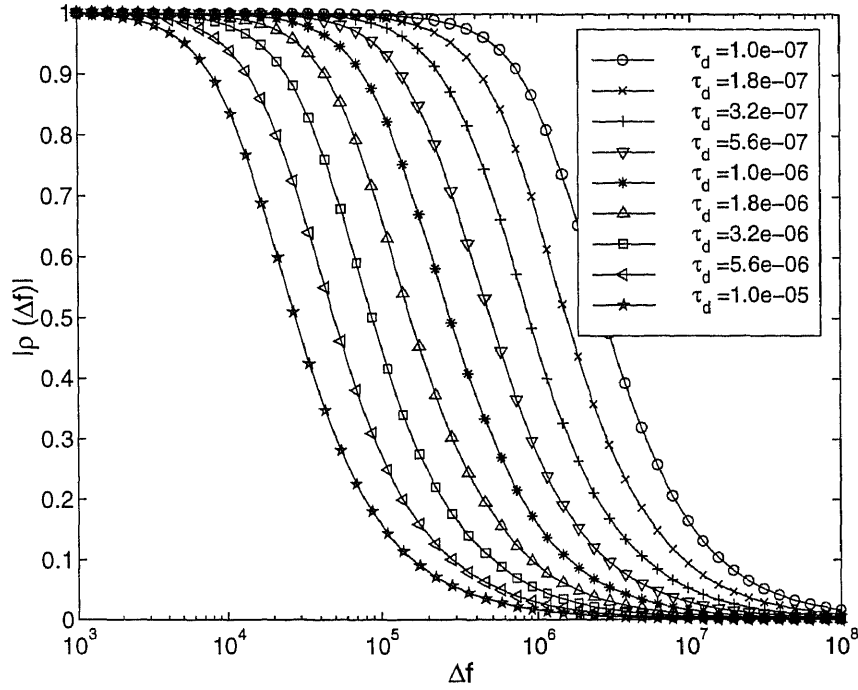


**Figure A.1** Absolute value of the frequency correlation function as a function of  $\Delta f$  with  $\tau_d$  as a parameter.

Define a vector  $\boldsymbol{\theta}$  containing correlated noise samples such that:

$$\boldsymbol{\theta} = \mathbf{Q}\boldsymbol{\xi}, \quad (\text{A.9})$$

where  $\mathbf{Q}$  introduces correlation between the noise samples from  $\mathbf{x}$ . The correlation matrix  $R_\theta$  follows as:

$$R_\theta = E[\boldsymbol{\theta}\boldsymbol{\theta}^H] = E[\mathbf{Q}\boldsymbol{\xi}\boldsymbol{\xi}^H\mathbf{Q}^H] = \mathbf{Q}R_\xi\mathbf{Q}^H = \mathbf{Q}\mathbf{Q}^H. \quad (\text{A.10})$$

The matrix  $R_\theta$  can be related to the desired correlation between the fading components at the different subcarriers using the frequency correlation function derived in the previous section:

$$R_\theta = \begin{bmatrix} \rho(0) & \rho(\Delta f) & \rho(2\Delta f) & \dots & \rho((N_c - 1)\Delta f) \\ \rho(-\Delta f) & \rho(0) & \rho(\Delta f) & \dots & \rho((N_c - 2)\Delta f) \\ \vdots & & \ddots & & \vdots \\ \vdots & & & \rho(0) & \rho(\Delta f) \\ \rho(-(N_c - 1)\Delta f) & \dots & & \rho(-\Delta f) & \rho(0) \end{bmatrix}. \quad (\text{A.11})$$

Note that  $R_\theta$  is hermitian as  $\rho(-\Delta f) = \rho(\Delta f)^*$ . Now, the unitary similarity transformation [47] is applied to  $R_\theta$ :

$$\mathbf{U}^H R_\theta \mathbf{U} = \mathbf{\Lambda}, \quad (\text{A.12})$$

where  $\mathbf{\Lambda}$  is an  $N_c \times N_c$  diagonal matrix with the eigenvalues of  $R_\theta$  on the diagonal and  $\mathbf{U}$  is a unitary matrix that contains a set of eigenvectors belonging to the eigenvalues in  $\mathbf{\Lambda}$ . Equation (A.12) can be rewritten to synthesize  $R_\theta$ :

$$R_\theta = \mathbf{U} \mathbf{\Lambda} \mathbf{U}^H = \mathbf{U} \mathbf{\Lambda}^{1/2} \mathbf{\Lambda}^{1/2} \mathbf{U}^H. \quad (\text{A.13})$$

Comparing equation (A.13) with equation (A.10) it follows that the vector  $\boldsymbol{\theta}$ , with the required correlation matrix  $R_\theta$ , can easily be generated by choosing:

$$\mathbf{Q} = \mathbf{U} \mathbf{\Lambda}^{1/2}. \quad (\text{A.14})$$

The correlated Rayleigh fading envelopes at the different subcarriers follow from  $\boldsymbol{\theta}$  by taking the absolute value:

$$\mathbf{A} = \text{diag}(|\boldsymbol{\theta}|), \quad (\text{A.15})$$

where  $\mathbf{A}$  is an  $N_c \times N_c$  diagonal matrix with the correlated Rayleigh fading envelopes on the diagonal.

## APPENDIX B

### NUMERICAL DETERMINATION OF THE BOOTSTRAP WEIGHTS FOR LOW INTERFERENCE TO SIGNAL RATIOS

In this appendix a numerical solution for the weights in the case of low ISR will be derived. Assuming  $\text{ISR} = -\infty$  and taking the desired user to be user number 1 ( $k = 1$ ), the matrix  $P$ , containing the different users' power levels, is given by:

$$P = \begin{bmatrix} p_1 & 0 & \dots & 0 \\ 0 & 0 & \dots & 0 \\ \vdots & & \ddots & \vdots \\ 0 & \dots & \dots & 0 \end{bmatrix} \begin{bmatrix} b_1 \\ b_2 \\ \vdots \\ b_K \end{bmatrix}. \quad (B.1)$$

The receiver output  $\mathbf{x}$  then becomes (compare with equation 2.12):

$$\mathbf{x} = \begin{bmatrix} \mathbf{c}_1^T \mathbf{A} \mathbf{c}_1 \\ \mathbf{c}_2^T \mathbf{A} \mathbf{c}_1 \\ \vdots \\ \mathbf{c}_K^T \mathbf{A} \mathbf{c}_1 \end{bmatrix} b_1 + \boldsymbol{\eta} = \boldsymbol{\rho}'_1 b_1 + \boldsymbol{\eta}, \quad (B.2)$$

where  $\boldsymbol{\rho}'_1$  is the first column of  $\mathbf{P}'_c$ .

At the output of the receiver the signal separator described in section 2.2 is applied. The weight matrix  $\mathbf{W}$  is chosen such that  $E[y_k \hat{\mathbf{b}}_k] = 0$ , where  $\hat{\mathbf{b}}_k$  is  $\hat{\mathbf{b}}$  without the  $k^{\text{th}}$  element and  $\hat{b}_k = \text{sgn}(y_k)$ . For user  $i$  this gives:

$$E[y_i \hat{b}_j] = E[y_i \text{sgn}(y_j)] = E[(\mathbf{v}^{iT} \mathbf{x}) \text{sgn}(\mathbf{v}^{jT} \mathbf{x})] = 0 \quad \text{for } j \neq i, \quad (B.3)$$

where  $\mathbf{v}^k$  is the  $k^{\text{th}}$  column of  $\mathbf{V}$  and  $\mathbf{V} = \mathbf{I} - \mathbf{W}$ . Substituting for  $\mathbf{x}$  this can be rewritten as

$$E[y_i \text{sgn}(y_j)] = E[\mathbf{v}^{iT} \boldsymbol{\rho}^1 b_1 \text{sgn}(\mathbf{v}^{jT} \boldsymbol{\rho}^1 b_1 + \xi_j)] + E[\xi_i \text{sgn}(\mathbf{v}^{jT} \boldsymbol{\rho}^1 b_1 + \xi_j)] = 0. \quad (B.4)$$

The first term of equation B.4 can be evaluated as follows for  $\text{ISR} = -\infty$ :

$$\begin{aligned} & E[\mathbf{v}^{iT} \boldsymbol{\rho}^1 b_1 \text{sgn}(\mathbf{v}^{jT} \boldsymbol{\rho}^1 b_1 + \xi_j)] \\ &= E[\mathbf{v}^{iT} \boldsymbol{\rho}^1 b_1 (Pr\{\mathbf{v}^{jT} \boldsymbol{\rho}^1 b_1 + \xi_j > 0\} - Pr\{\mathbf{v}^{jT} \boldsymbol{\rho}^1 b_1 + \xi_j < 0\})] \end{aligned}$$

$$\begin{aligned}
&= E \left[ \mathbf{v}^{iT} \boldsymbol{\rho}^1 b_1 \left( Pr \left\{ \xi_j > -\mathbf{v}^{jT} \boldsymbol{\rho}^1 b_1 \right\} - Pr \left\{ \xi_j < -\mathbf{v}^{jT} \boldsymbol{\rho}^1 b_1 \right\} \right) \right] \\
&= \frac{1}{2} \sum_{b_1 \in \{-1, 1\}} \left\{ \mathbf{v}^{iT} \boldsymbol{\rho}^1 b_1 \left( Q \left( -\frac{\mathbf{v}^{jT} \boldsymbol{\rho}^1 b_1}{\sigma_{\xi_j}} \right) - Q \left( \frac{\mathbf{v}^{jT} \boldsymbol{\rho}^1 b_1}{\sigma_{\xi_j}} \right) \right) \right\} \\
&= \frac{1}{2} \sum_{b_1 \in \{-1, 1\}} \left\{ \mathbf{v}^{iT} \boldsymbol{\rho}^1 b_1 \left( 1 - 2Q \left( \frac{\mathbf{v}^{jT} \boldsymbol{\rho}^1 b_1}{\sigma_{\xi_j}} \right) \right) \right\} \\
&= -\frac{1}{2} \mathbf{v}^{iT} \boldsymbol{\rho}^1 \left( 1 - 2Q \left( -\frac{\mathbf{v}^{jT} \boldsymbol{\rho}^1}{\sigma_{\xi_j}} \right) \right) + \frac{1}{2} \mathbf{v}^{iT} \boldsymbol{\rho}^1 \left( 1 - 2Q \left( \frac{\mathbf{v}^{jT} \boldsymbol{\rho}^1}{\sigma_{\xi_j}} \right) \right) \\
&= \mathbf{v}^{iT} \boldsymbol{\rho}^1 Q \left( -\frac{\mathbf{v}^{jT} \boldsymbol{\rho}^1}{\sigma_{\xi_j}} \right) - \mathbf{v}^{iT} \boldsymbol{\rho}^1 Q \left( \frac{\mathbf{v}^{jT} \boldsymbol{\rho}^1}{\sigma_{\xi_j}} \right) \\
&= \mathbf{v}^{iT} \boldsymbol{\rho}^1 \left( 1 - 2Q \left( \frac{\mathbf{v}^{jT} \boldsymbol{\rho}^1}{\sigma_{\xi_j}} \right) \right), \tag{B.5}
\end{aligned}$$

where

$$Q(x) = \frac{1}{\sqrt{2\pi}} \int_x^\infty e^{-t^2/2} dt. \tag{B.6}$$

Evaluation of the second term of equation B.4 can be facilitated by introducing a linear transformation expressing the correlated noise samples  $\xi_i$  and  $\xi_j$  as a function of uncorrelated (noise is Gaussian, thus uncorrelated is also independent) identically distributed noise samples  $\lambda_i$  and  $\lambda_j$ :

$$\begin{bmatrix} \xi_i \\ \xi_j \end{bmatrix} = \begin{bmatrix} F & G \\ 0 & 1 \end{bmatrix} \begin{bmatrix} \lambda_i \\ \lambda_j \end{bmatrix}. \tag{B.7}$$

It can be seen that

$$\xi_i = F\lambda_i + G\lambda_j, \tag{B.8}$$

$$\xi_j = \lambda_j. \tag{B.9}$$

Thus,

$$\lambda_i = \frac{\xi_i - G\xi_j}{F}. \tag{B.10}$$

Additionally,

$$E \left[ \xi_i^2 \right] = \sigma_{\xi_i}^2 = \sigma^2 \mathbf{v}^{iT} \mathbf{P}_c \mathbf{v}^i, \tag{B.11}$$

$$E \left[ \xi_j^2 \right] = \sigma_{\xi_j}^2 = \sigma^2 \mathbf{v}^{jT} \mathbf{P}_c \mathbf{v}^j, \tag{B.12}$$

$$E[\xi_i \xi_j] = \sigma^2 \mathbf{v}^{iT} \mathbf{P}_c \mathbf{v}^j, \quad (\text{B.13})$$

$$E[\lambda_i^2] = E[\lambda_j^2] = E[\xi_j^2]. \quad (\text{B.14})$$

It is known that  $\lambda_i$  and  $\lambda_j$  are uncorrelated thus,

$$\begin{aligned} E[\lambda_i \lambda_j] &= E\left[\xi_j \left(\frac{\xi_i - G\xi_j}{F}\right)\right] \\ &= \frac{E[\xi_i \xi_j] - G E[\xi_j^2]}{F} = 0. \end{aligned} \quad (\text{B.15})$$

Therefore,

$$G = \frac{E[\xi_i \xi_j]}{E[\xi_j^2]} = \frac{\mathbf{v}^{iT} \mathbf{P}_c \mathbf{v}^j}{\mathbf{v}^{jT} \mathbf{P}_c \mathbf{v}^j}. \quad (\text{B.16})$$

From  $E[\lambda_i^2] = E[\lambda_j^2]$  it follows that

$$\begin{aligned} E[\lambda_i^2] &= E\left[\left(\frac{\xi_i - G\xi_j}{F}\right)^2\right] \\ &= E\left[\frac{\xi_i^2 - 2G\xi_i \xi_j + G^2 \xi_j^2}{F^2}\right] \\ &= \frac{E[\xi_i^2] - 2\frac{E[\xi_i \xi_j]^2}{E[\xi_j^2]} + \frac{E[\xi_i \xi_j]^2}{E[\xi_j^2]}}{F^2} \\ &= \frac{E[\xi_i^2] - \frac{E[\xi_i \xi_j]^2}{E[\xi_j^2]}}{F^2} \\ &= E[\lambda_j^2] = E[\xi_j^2]. \end{aligned} \quad (\text{B.17})$$

From this it follows that,

$$F = \sqrt{\frac{E[\xi_i^2] E[\xi_j^2] - E[\xi_i \xi_j]^2}{E[\xi_j^2]^2}}. \quad (\text{B.18})$$

With this definition of  $F$  and  $G$  the second term of equation B.4 can be evaluated:

$$\begin{aligned} E[\xi_i \text{sgn}(\mathbf{v}^{jT} \boldsymbol{\rho}^1 b_1 + \xi_j)] &= E[(F\lambda_i + G\lambda_j) \text{sgn}(\mathbf{v}^{jT} \boldsymbol{\rho}^1 b_1 + \lambda_j)] \\ &= G E[\xi_j \text{sgn}(\mathbf{v}^{jT} \boldsymbol{\rho}^1 b_1 + \xi_j)], \end{aligned} \quad (\text{B.19})$$

since  $\lambda_i$  and  $\lambda_j$  are uncorrelated and  $\lambda_j = \xi_j$ . With the probability density function of  $\xi_j$  defined as

$$p_{\xi_j}(\xi_j) = \frac{1}{\sqrt{2\pi\sigma_{\xi_j}^2}} \exp\left(-\frac{\xi_j^2}{2\sigma_{\xi_j}^2}\right). \quad (\text{B.20})$$

Continuing the evaluation of the expectation:

$$\begin{aligned}
& G E \left[ \xi_j \text{sgn}(\mathbf{v}^{jT} \boldsymbol{\rho}^1 b_1 + \xi_j) \right] \\
&= \frac{1}{2} G \sum_{b_1 \in \{-1, 1\}} \left\{ \int_{-\mathbf{v}^{jT} \boldsymbol{\rho}^1 b_1}^{\infty} \xi_j p_{\xi_j}(\xi_j) d\xi_j - \int_{-\infty}^{-\mathbf{v}^{jT} \boldsymbol{\rho}^1 b_1} \xi_j p_{\xi_j}(\xi_j) d\xi_j \right\} \\
&= \frac{1}{2} G \sum_{b_1 \in \{-1, 1\}} \left\{ \int_{-\mathbf{v}^{jT} \boldsymbol{\rho}^1 b_1}^{\infty} \xi_j p_{\xi_j}(\xi_j) d\xi_j + \int_{\mathbf{v}^{jT} \boldsymbol{\rho}^1 b_1}^{\infty} \xi_j p_{\xi_j}(\xi_j) d\xi_j \right\} \\
&= \frac{1}{2} G \sum_{b_1 \in \{-1, 1\}} \frac{\sigma_{\xi_j}}{\sqrt{2\pi}} \left\{ \exp \left( -\frac{(\mathbf{v}^{jT} \boldsymbol{\rho}^1 b_1)^2}{2\sigma_{\xi_j}^2} \right) + \exp \left( -\frac{(\mathbf{v}^{jT} \boldsymbol{\rho}^1 b_1)^2}{2\sigma_{\xi_j}^2} \right) \right\} \\
&= \frac{2\sigma_{\xi_j}}{\sqrt{2\pi}} G \exp \left( -\frac{(\mathbf{v}^{jT} \boldsymbol{\rho}^1)^2}{2\sigma_{\xi_j}^2} \right) \\
&= \frac{2\sigma^2 \mathbf{v}^{iT} \mathbf{P}_c \mathbf{v}^j}{\sqrt{2\pi\sigma_{\xi_j}^2}} \exp \left( -\frac{(\mathbf{v}^{jT} \boldsymbol{\rho}^1)^2}{2\sigma_{\xi_j}^2} \right). \tag{B.21}
\end{aligned}$$

Utilizing this transformation, the second term of equation B.4 becomes

$$\begin{aligned}
E \left[ \xi_i \text{sgn}(\mathbf{v}^{jT} \boldsymbol{\rho}^1 b_1 + \xi_j) \right] &= E \left[ (F\lambda_i + G\lambda_j) \text{sgn}(\mathbf{v}^{jT} \boldsymbol{\rho}^1 b_1 + \lambda_j) \right] \\
&= G E \left[ \xi_j \text{sgn}(\mathbf{v}^{jT} \boldsymbol{\rho}^1 b_1 + \xi_j) \right]. \tag{B.22}
\end{aligned}$$

Combining the first and the second term of equation B.4 results in

$$\begin{aligned}
E[y_i \text{sgn}(y_j)] &= \mathbf{v}^{iT} \boldsymbol{\rho}^1 \left( 1 - 2Q \left( \frac{\mathbf{v}^{jT} \boldsymbol{\rho}^1}{\sigma_{\xi_j}} \right) \right) + \frac{2\sigma^2 \mathbf{v}^{iT} \mathbf{P}_c \mathbf{v}^j}{\sqrt{2\pi\sigma_{\xi_j}^2}} \exp \left( -\frac{(\mathbf{v}^{jT} \boldsymbol{\rho}^1)^2}{2\sigma_{\xi_j}^2} \right) \\
&= \mathbf{v}^{iT} \left[ \boldsymbol{\rho}^1 \left( 1 - 2Q \left( \frac{\mathbf{v}^{jT} \boldsymbol{\rho}^1}{\sigma_{\xi_j}} \right) \right) + \frac{2\sigma^2 \mathbf{P}_c \mathbf{v}^j}{\sqrt{2\pi\sigma_{\xi_j}^2}} \exp \left( -\frac{(\mathbf{v}^{jT} \boldsymbol{\rho}^1)^2}{2\sigma_{\xi_j}^2} \right) \right] \\
&= \mathbf{v}^{iT} \mathbf{r}^j, \tag{B.23}
\end{aligned}$$

where  $\mathbf{r}^j$  is defined by the term within the square brackets. Notice that,  $\mathbf{r}^j$  is only a function of  $\mathbf{v}^j$  and not of  $\mathbf{v}^i$ . Note however, that the expression is still conditional on the subcarrier amplitudes as they are incorporated in  $\boldsymbol{\rho}^1$ .

In the case of the reduced complexity receiver, as described in section 2.3, equation ( B.23) can be used with the following definitions:

$$\boldsymbol{\rho}^1 = \mathbf{C}_1^{cT} \mathbf{A} \mathbf{c}_1, \tag{B.24}$$

$$\mathbf{P}_c = \mathbf{C}_1^{c^T} \mathbf{C}_1^c, \quad (\text{B.25})$$

$$\sigma_{\xi_j}^2 = \sigma^2 \mathbf{v}^{j^T} \mathbf{P}_c \mathbf{v}^j. \quad (\text{B.26})$$

It is clear that the application of the reduced complexity receiver structure results in a  $2 \times 2$  system of non-linear equations, i.e.  $i, j = 1, 2$ :

$$\begin{cases} r_1^2 + v_{12} r_2^2 = 0 \\ v_{21} r_1^1 + r_2^1 = 0. \end{cases} \quad (\text{B.27})$$

Note, that for the  $2 \times 2$  case the  $r_j^i$  are only dependent on one parameter, either  $v_{12}$  or  $v_{21}$ . Therefore,  $v_{21}$  can be expressed as a function of  $r_1^1$  and  $r_2^1$ . Following this,  $v_{21}$  can be substituted into the second equation, resulting in a non-linear function of only one parameter,  $v_{12}$ . A numerical method, e.g. Matlab's 'fzero' function, can then be employed to search for the value of  $v_{12}$  which satisfies  $r_1^2 + v_{12} r_2^2 = 0$ . This value can then be used to compute the corresponding value of  $v_{21}$ .

The use of MRC in combination with the reduced complexity receiver structure results in the following definitions for use in equation (B.23):

$$\boldsymbol{\rho}^1 = \mathbf{C}_1^{c^T} \mathbf{A}^2 \mathbf{c}_1, \quad (\text{B.28})$$

$$\mathbf{P}_c = \mathbf{C}_1^{c^T} \mathbf{A}^2 \mathbf{C}_1^c, \quad (\text{B.29})$$

$$\sigma_{\xi_j}^2 = \sigma^2 \mathbf{v}^{j^T} \mathbf{P}_c \mathbf{v}^j. \quad (\text{B.30})$$

## APPENDIX C

### OUTPUT OF THE DFT IN THE PRESENCE OF A FREQUENCY OFFSET

Assume a multicarrier modulated system consisting of  $N_c$  subcarriers. Let  $\mathbf{b}$  be a length  $N_c$  vector containing the unmodulated symbols. Then,  $\mathbf{X} = \text{IDFT}\{\mathbf{b}\}$ , is the modulated sequence, where the modulation is implemented by the  $N_c$ -point IDFT:

$$X_n = \sum_{m=0}^{N_c-1} b_m e^{j \frac{2\pi n m}{N_c}}. \quad (C.1)$$

It is instructive to think of the elements of  $\mathbf{b}$  as the frequency domain samples and those of  $\mathbf{X}$  as the corresponding time domain samples of the DFT pair, i.e. in the above equation  $n$  can be considered a time index and  $m$  a frequency index.

The output of the demodulation by the  $N_c$ -point DFT in the presence of a frequency offset can be described as

$$z_k = \frac{1}{N_c} \sum_{l=0}^{N_c-1} X_l e^{-j \frac{2\pi l k}{N_c}} e^{j \frac{2\pi l \varepsilon}{N_c}}, \quad (C.2)$$

where  $k$  can be regarded as a frequency index and where  $\varepsilon$  is the normalized frequency offset:

$$\varepsilon = \frac{\text{offset}}{\Delta f}, \quad (C.3)$$

where  $\Delta f$  is the subcarrier spacing.

The  $z_k$  may be rewritten as follows:

$$\begin{aligned} z_k &= \frac{1}{N_c} \sum_{l=0}^{N_c-1} \left( \sum_{m=0}^{N_c-1} b_m e^{j \frac{2\pi l m}{N_c}} \right) e^{-j \frac{2\pi l k}{N_c}} e^{j \frac{2\pi l \varepsilon}{N_c}} \\ &= \frac{1}{N_c} \sum_{m=0}^{N_c-1} b_m \sum_{l=0}^{N_c-1} e^{j \frac{2\pi l}{N_c} (m-k+\varepsilon)} \\ &= \frac{1}{N_c} \sum_{m=0}^{N_c-1} b_m \frac{\sin(\pi(m-k+\varepsilon))}{\sin\left(\frac{\pi(m-k+\varepsilon)}{N_c}\right)} e^{j \frac{(N_c-1)\pi(m-k+\varepsilon)}{N_c}}, \end{aligned} \quad (C.4)$$

where the following equality was used:

$$\sum_{l=0}^{N_c-1} e^{-j\omega l} = \frac{1 - e^{j\omega N_c}}{1 - e^{j\omega}} = \frac{\sin(\omega N_c/2)}{\sin(\omega/2)} e^{-j(N_c-1)\omega/2}. \quad (C.5)$$



Continuing the derivation of  $z(k)$ :

$$\begin{aligned}
z_k &= \sum_{m=0}^{N_c-1} b_m \frac{\sin(\pi(m-k+\varepsilon))}{N_c \sin\left(\frac{\pi(m-k+\varepsilon)}{N_c}\right)} e^{-j\frac{\pi(m-k+\varepsilon)}{N_c}} e^{j\pi(m-k+\varepsilon)} \\
&= \sum_{m=0}^{N_c-1} b_m \frac{\sin(\pi(m-k+\varepsilon))}{N_c \sin\left(\frac{\pi(m-k+\varepsilon)}{N_c}\right)} \\
&\quad [\cos(\pi(m-k+\varepsilon)) + j \sin(\pi(m-k+\varepsilon))] e^{-j\frac{\pi(m-k+\varepsilon)}{N_c}} \\
&= \sum_{m=0}^{N_c-1} b_m \frac{\frac{1}{2} \sin(2\pi(m-k+\varepsilon)) + j\frac{1}{2} - j\frac{1}{2} \cos(2\pi(m-k+\varepsilon))}{N_c \sin\left(\frac{\pi(m-k+\varepsilon)}{N_c}\right)} e^{-j\frac{\pi(m-k+\varepsilon)}{N_c}} \\
&= \sum_{m=0}^{N_c-1} b_m \frac{\sin(2\pi\varepsilon) + j - j \cos(2\pi\varepsilon)}{2N_c \sin\left(\frac{\pi(m-k+\varepsilon)}{N_c}\right)} \\
&\quad \left( \cos\left(\frac{\pi(m-k+\varepsilon)}{N_c}\right) - j \sin\left(\frac{\pi(m-k+\varepsilon)}{N_c}\right) \right), \tag{C.6}
\end{aligned}$$

where it was used that  $\sin(2\pi(m-k+\varepsilon)) = \sin(2\pi\varepsilon)$  for  $m, k$  integer. Then, it follows that

$$\begin{aligned}
z_k &= \sum_{m=0}^{N_c-1} b_m \left[ \frac{2 \sin(\pi\varepsilon) \cos(\pi\varepsilon) + j(\cos^2(\pi\varepsilon) + \sin^2(\pi\varepsilon))}{2N_c} \right. \\
&\quad \left. - \frac{j(\cos^2(\pi\varepsilon) - \sin^2(\pi\varepsilon))}{2N_c} \right] \left( \cot\left(\frac{\pi(m-k+\varepsilon)}{N_c}\right) - j \right) \\
&= \sum_{m=0}^{N_c-1} b_m \frac{2 \sin(\pi\varepsilon) \cos(\pi\varepsilon) + 2j \sin^2(\pi\varepsilon)}{2N_c} \left( \cot\left(\frac{\pi(m-k+\varepsilon)}{N_c}\right) - j \right) \\
&= \sum_{m=0}^{N_c-1} b_m \frac{\sin(\pi\varepsilon) e^{j\pi\varepsilon}}{N_c} \left( \cot\left(\frac{\pi(m-k+\varepsilon)}{N_c}\right) - j \right) \\
&= \sum_{m=0}^{N_c-1} b_m s(m-k), \tag{C.7}
\end{aligned}$$

where  $s(m-k)$  is defined as,

$$s(m-k) = \frac{\sin(\pi\varepsilon) e^{j\pi\varepsilon}}{N_c} \left( \cot\left(\frac{\pi(m-k+\varepsilon)}{N_c}\right) - j \right). \tag{C.8}$$

## APPENDIX D

### LIST OF SYMBOLS AND ABBREVIATIONS

#### D.1 Symbols

$\mathbf{A}$	channel amplitude matrix ( $\mathbf{A} =  \mathbf{H} $ )
$\mathbf{b}$	vector containing user(s) data symbols
$\mathbf{b}_k$	$\mathbf{b}$ without the $k^{\text{th}}$ element
$\hat{\mathbf{b}}_k$	hard decision estimate of $\mathbf{b}_k$
$B_t$	total system bandwidth
$B_c$	coherence bandwidth
$B_s$	subcarrier bandwidth
$\mathbf{c}_k$	code sequence of user $k$
$\mathbf{c}_k^c$	compounded code sequence for user $k$
$\mathbf{C}$	code matrix of the $K_a$ active users
$\mathbf{C}_k$	$\mathbf{C}$ without the $k^{\text{th}}$ column
$\mathbf{C}_k^c$	matrix containing $\mathbf{c}_k$ and $\mathbf{c}_k^c$
$\mathbf{C}_K$	code matrix of all $K$ users
$\mathbf{C}_{K_k}$	$\mathbf{C}_K$ without the $k^{\text{th}}$ column
$E_0$	energy of the constellation point with the lowest amplitude
$\Delta f$	frequency separation
$F$	system parameter for frequency separation of subcarriers
$h(t, \tau)$	complex low-pass channel impulse response
$\mathbf{H}$	complex channel matrix
$\mathbf{I}_n$	$n \times n$ identity matrix
$K$	maximum number of users
$K_a$	number of active users
$M$	number of points in the signal constellation
$N_c$	number of subcarriers

$N_b$	number of symbols for bit error counting
$N_{mc}$	number of Monte-Carlo runs for bit error rate averaging
$\mathbf{P}$	signal power matrix
$\mathbf{P}_k$	$\mathbf{P}$ without the $k^{\text{th}}$ row and column
$\mathbf{P}_c$	code cross-correlation matrix ( $\mathbf{P}_c = \mathbf{C}^T \mathbf{C}$ )
$\mathbf{P}_c^{-1}$	conventional decorrelator for DS-CDMA, and MC-CDMA in a non-faded AWGN channel
$\mathbf{P}_{c_k}$	$\mathbf{P}_c$ without the $k^{\text{th}}$ row and column
$\mathbf{P}'_c$	conditional code cross-correlation matrix for MC-CDMA with EGC ( $\mathbf{P}'_c = \mathbf{C}^T \mathbf{A} \mathbf{C}$ )
$\mathbf{P}'_c{}^{-1}$	conventional decorrelator for MC-CDMA with EGC in a fading channel
$\mathbf{P}'_{c_k}$	$\mathbf{P}'_c$ without the $k^{\text{th}}$ row and column
$\mathbf{P}''_c$	conditional code cross-correlation matrix for MC-CDMA with MRC ( $\mathbf{P}''_c = \mathbf{C}^T \mathbf{A}^2 \mathbf{C}$ )
$\mathbf{P}''_c{}^{-1}$	conventional decorrelator for MC-CDMA with MRC in a fading channel
$\mathbf{P}''_{c_k}$	$\mathbf{P}''_c$ without the $k^{\text{th}}$ row and column
$\mathbf{P}_{sc}$	code and subcarrier cross-correlation matrix ( $\mathbf{P}'_{sc} = \mathbf{C}^T \mathbf{S}^T \mathbf{C}$ )
$\mathbf{P}'_{sc}$	conditional code and subcarrier cross-correlation matrix ( $\mathbf{P}'_{sc} = \mathbf{C}^T \mathbf{S}^T \mathbf{A} \mathbf{C}$ )
$Q(\tau)$	power-delay profile
$R_h(t, t + \Delta t; \tau, \eta)$	autocorrelation function of a WSS complex low-pass channel impulse response
$\mathbf{R}_x$	covariance matrix of $\mathbf{x}$
$R_T(f, f + \Delta f; t, t + \Delta t)$	time-frequency correlation function

$\mathbf{S}$	subcarrier correlation matrix
$\Delta t$	time difference
$T(f, t)$	time-variant transfer function
$T_b$	bit duration
$T_c$	coherence time
$T_s$	symbol duration
$\mathbf{V}$	signal separation matrix
$\mathcal{W}$	window length
$\mathbf{W}$	bootstrap weight matrix
$\mathbf{w}_k$	$k^{\text{th}}$ column of $\mathbf{W}$ without the $k^{\text{th}}$ element
$\boldsymbol{\alpha}$	compounding vector, to combine the codes of all the interfering users
$\mu$	step-size parameter
$\tau_d$	rms channel delay spread
$\tau_0$	decorrelation time or coherence time
$\bar{\tau}$	mean propagation delay
$\tau_{\max}$	maximum multipath delay relative to the first path
$\rho(\Delta f)$	frequency correlation function
$\boldsymbol{\rho}'_k$	the $k^{\text{th}}$ column of $\mathbf{P}'_c$ without the $k^{\text{th}}$ element
$(.)^T$	transpose of a vector or matrix
$(.)^H$	Hermitian transpose of a vector or matrix
$(.)^{-1}$	inverse of a scalar or matrix
$(.)^*$	complex conjugate
$ \cdot $	absolute value

## D.2 Abbreviations

AFDD	adaptive full dimensional detector
ARCD	adaptive reduced complexity detector
AWGN	additive white Gaussian noise
BB	backward-backward
BER	bit error rate
BPSK	binary phase shift keying
CDMA	code division multiple access
cir	channel impulse response
CIR	carrier-to-interference ratio
DAB	Digital Audio Broadcasting
DFT	discrete Fourier transform
DS	direct sequence
DS-CDMA	direct sequence code division multiple access
dTTb	digital terrestrial television broadcasting
EGC	equal gain combining
FDMA	frequency division multiple access
FB	forward-backward
FDD	full dimensional decorrelator
FF	forward-forward
FFT	fast Fourier transform
FH	frequency hopping
FO	frequency offset
FOC	frequency offset correction
GSM	Global System for Mobile Communications Groupe Spéciale Mobile
HDSL	high-rate digital subscriber line

IC	interference cancelation
ICI	inter-carrier interference
IDFT	inverse discrete Fourier transform
IFFT	inverse fast Fourier transform
i.i.d.	independent identically distributed
IMT-2000	International Mobile Telecommunications 2000
ISI	inter-symbol interference
ISR	interference-to-signal ratio
JDD	joint decorrelating detector
LAN	local area network
LM	land mobile
LSNR	local mean signal-to-noise ratio
MAI	multiple access interference
MC-CDMA	multicarrier code division multiple access
MCM	multicarrier modulation
MF	matched filter
MLE	maximum likelihood estimate
MMSE	minimum mean square error
MPSK	M-ary phase shift keying
MRC	maximal ratio combining
MUD	multiuser detection
MUI	multiuser interference
OFDM	orthogonal frequency division multiplexing
PCS	personal communication systems
pdf	probability density function
QAM	quadrature amplitude modulation
QOS	quality-of-service

QPSK	quaternary phase shift keying
RCD	reduced complexity decorrelator
rms	root mean square
SINR	signal-to-interference-plus-noise ratio
SNR	signal-to-noise ratio
SS	spread spectrum
SUB	single user bound
SUD	single user detector
TDMA	time division multiple access
TH	time hopping
UMTS	Universal Mobile Telecommunications Systems
WLAN	wireless local area network
WSS	wide sense stationary
WSSUS	wide sense stationary uncorrelated scattering

## REFERENCES

1. R. Prasad, *CDMA for Wireless Personal Communications*. London, Great-Britain: Artech House Publishers, 1996.
2. J. G. Proakis, *Digital Communications*. New York, NY, U.S.A.: McGraw-Hill, third ed., 1995.
3. R. W. Chang, "Synthesis of band-limited orthogonal signals for multichannel data transmission," *Bell System Technical Journal*, vol. 45, pp. 1775–1796, Dec. 1966.
4. B. R. Saltzberg, "Performance of an efficient parallel data transmission system," *IEEE Transactions on Communication Technology*, vol. 15, pp. 805–811, Dec. 1967.
5. R. W. Chang and R. A. Gibby, "A theoretical study of performance of an orthogonal multiplexing data transmission scheme," *IEEE Transactions on Communication Technology*, vol. 16, pp. 529–540, Aug. 1968.
6. S. B. Weinstein and P. M. Ebert, "Data transmission by frequency-division multiplexing using the discrete fourier transform," *IEEE Transactions on Communication Technology*, vol. 19, pp. 626–634, Oct. 1971.
7. J. A. C. Bingham, "Multicarrier modulation for data transmission: An idea whose time has come," *IEEE Communications Magazine*, vol. 28, pp. 5–14, May 1990.
8. L. J. Cimini, Jr., "Analysis and simulation of a digital mobile channel using orthogonal frequency division multiplexing," *IEEE Transactions on Communications*, vol. 33, pp. 665–675, July 1985.
9. M. Alard and R. Lasalle, "Principles of modulation and channel coding for digital broadcasting for mobile receivers," *EBU Review*, pp. 168–190, Aug. 1987.
10. J.-P. Linnartz and S. Hara, "Special issue on multi-carrier communications," *Wireless Personal Communications*, vol. 2, no. 1/2, 1995.
11. K. Fazel, S. Kaiser, P. Robertson, and M. J. Ruf, "A concept of digital terrestrial television broadcasting," *Wireless Personal Communications, special issue on multi-carrier communications*, vol. 2, no. 1&2, pp. 9–27, 1995.
12. L. J. Cimini, Jr., "Performance studies for high-speed indoor wireless communications," *Wireless Personal Communications, special issue on multi-carrier communications*, vol. 2, no. 1&2, pp. 67–85, 1995.



13. E. G. Tiedemann, Jr., Y.-C. Jou, and J. P. Odenwalder, "The evolution of IS-95 to a third generation system and to the IMT-2000 era," in *ACTS Summit*, (Aalborg, Denmark), pp. 924–929, Oct. 1997.
14. N. Yee, J. P. M. G. Linnartz, and G. Fettweis, "Multi-carrier CDMA indoor wireless radio networks," in *Proc. IEEE Personal, Indoor and Mobile Radio Communications Conference*, (Yokohama, Japan), pp. 109–113, Sept. 1993.
15. K. Fazel, "Performance of cdma/ofdm for mobile communication system," in *Proceedings IEEE International Conference on Universal Personal Communications (ICUPC'93)*, (Ottawa, Canada), pp. 975–979, Oct. 1993.
16. S. Kaiser, "On the performance of different detection techniques for OFDM-CDMA in fading channels," in *Proceedings IEEE Global Telecommunications Conference (Globecom'95)*, (Singapore), pp. 2059–2063, Nov. 1995.
17. L. Vandendorpe, "Multitone spread spectrum multiple access communications system in a multipath rician fading channel," *IEEE Transactions on Vehicular Technology*, vol. 44, no. 4, pp. 327–337, 1995.
18. S. Verdú, "Minimum probability of error for asynchronous gaussian multiple-access channels," *IEEE Transactions on Information Theory*, vol. 32, pp. 85–96, Jan. 1986.
19. R. Lupas and S. Verdú, "Linear multiuser detector for asynchronous code division multiple access channels," *IEEE Transactions on Information Theory*, vol. 35, pp. 123–136, Jan. 1989.
20. R. Lupas and S. Verdú, "Near-far resistance of multi-user detectors in asynchronous channels," *IEEE Transactions on Communications*, vol. 38, pp. 496–508, Apr. 1990.
21. Y. Bar-Ness, "The bootstrap decorrelating algorithm: A promising tool for adaptive separation of multiuser CDMA signals," in *Proc. 7th Tyrrhenian International Workshop on Digital Communication, invited paper*, (Viareggio, Italy), Sept. 1995.
22. Y. Bar-Ness and J. B. Punt, "Adaptive bootstrap multi-user CDMA detector," special issue on "Signal Separation and Interference Cancellation for Personal, Indoor and Mobile Radio Communications," *Wireless Personal Communications*, vol. 3, no. 1-2, pp. 55–71, 1996.
23. Y. Bar-Ness and N. van Waes, "Adaptive algorithm for the multishot matched detector in a multipath rayleigh fading environment," in *Proc. IEEE Vehicular Technology Conference*, (Ottawa, Canada), pp. 179–183, May 1998.

24. N. van Waes and Y. Bar-Ness, "The bootstrap algorithm for a one-shot matched filtering multiuser detector in a multipath environment," in *Proc. IEEE Vehicular Technology Conference*, (Ottawa, Canada), pp. 184–188, May 1998.
25. Y. Bar-Ness, J. P. Linnartz, and X. Liu, "Synchronous multi-user multi-carrier CDMA communications system with decorrelating interference canceler," in *Proc. IEEE Personal, Indoor and Mobile Radio Communications Conference*, (The Hague, The Netherlands), pp. 184–188, Sept. 1994.
26. P. Zong, "Signal processing topics in multicarrier modulation: Frequency offset correction for OFDM and multiuser interference cancellation for MC-CDMA," Master's thesis, New Jersey Institute of Technology, Newark, NJ, U.S.A., May 1998.
27. U. Madhow and M. L. Honig, "MMSE interference suppression for direct-sequence spread-spectrum CDMA," *IEEE Transactions on Communications*, vol. 42, pp. 3178–3188, Dec. 1994.
28. H. Ge and Y. Bar-Ness, "Comparative study of linear minimum mean square error (lmmse) and the adaptive bootstrap multiuser detectors for CDMA communications," in *Proc. International Conference on Communications*, (Dallas, TX, U.S.A.), pp. 78–82, June 1996.
29. M. Varanasi and B. Aazhang, "Near-optimum detector in synchronous code division multiple access communications," *IEEE Transactions on Communications*, vol. 39, pp. 725–736, May 1991.
30. Z. Siveski, Y. Bar-Ness, and D. Chen, "Error performance of synchronous multiuser code division multiple access detector with multidimensional adaptive canceller," *European Transactions on Telecommunications and Related Technologies*, vol. 5, pp. 719–724, Nov.-Dec. 1994.
31. P. Komulainen, Y. Bar-Ness, and J. Lilleberg, "Simplified bootstrap adaptive decorrelator for CDMA downlink," in *Proc. IEEE International Conference on Communications*, (Atlanta, GA, U.S.A.), pp. 380–384, June 1998.
32. M. A. Visser and Y. Bar-Ness, "Adaptive Multi-Carrier CDMA (MC-CDMA) Structure for Downlink PCS," in *Proc. 9th Tyrrhenian International Workshop on Digital Communication*, (Lerici, Italy), Sept. 1997.
33. P. Komulainen, Y. Bar-Ness, and J. Lilleberg, "Two and six matched filter adaptive decorrelator for down link multipath CDMA channels," in *Proc. IEEE Vehicular Technology Conference*, (Ottawa, Canada), pp. 963–967, May 1998.

34. Y. Bar-Ness and J. Rokach, "Cross-coupled bootstrapped adaptive interference canceler," in *International Conference on Antennas and Propagation*, (Los Angeles, CA), pp. 292–295, June 1981.
35. Y. Bar-Ness, J. W. Carlin, and M. L. Steinberger, "Bootstrapping adaptive cross pol cancelers for satellite communications," in *Proc. International Communications Conference*, (Philadelphia, PA), pp. 4F.5.1–4F.5.5, June 1982.
36. W. Carlin, Y. Bar-Ness, S. Gross, M. Steinberger, and W. Studdiford, "An IF cross-pol canceler for microwave radio systems," *Journal on Selected Areas in Communications: Advances in Digital Communications by Radio*, vol. SAC-5, pp. 502–514, April 1987.
37. A. Dinc and Y. Bar-Ness, "Error probability of bootstrapped blind adaptive cross-pol cancellers for m-ary QAM over non-dispersive fading channels," in *Proceedings International Communications Conference*, 1992.
38. A. Dinc and Y. Bar-Ness, "Convergence and performance comparison of three different structures of bootstrap blind adaptive algorithms for multisignal co-channel separation," in *Proc. MILCOM*, (San Diego, CA, U.S.A), Oct. 1992.
39. T. Pollet, M. van Bladel, and M. Moeneclaey, "BER sensitivity of OFDM systems to carrier frequency offset and wiener phase noise," *IEEE Transactions on Communications*, vol. 43, pp. 191–193, Feb. 1995.
40. Y. Zhao and S.-G. Häggman, "Sensitivity to doppler shift and carrier frequency errors in OFDM systems – the consequences and solutions," in *Proc. IEEE Vehicular Technology Conference*, (Atlanta, GA, U.S.A.), pp. 1564–1568, Apr. 1996.
41. P. H. Moose, "A technique for orthogonal frequency division multiplexing frequency offset correction," *IEEE Transactions on Communications*, vol. 42, pp. 2908–2914, Oct. 1994.
42. Y. Zhao, J.-D. Leclercq, and S.-G. Häggman, "Intercarrier interference compression in OFDM communication systems by using correlative coding," *IEEE Communications Letters*, vol. 2, pp. 214–216, Aug. 1998.
43. M. G. Jansen, *Design considerations for specifying, modelling and performance trade-offs of wireless communications systems based on DS-CDMA*. TWAIO thesis, Delft University of Technology, Delft, the Netherlands, June 1994.
44. N. P. Shein, "An algorithm for generating nonuniformly spaced correlated samples for simulating a nonselective rayleigh fading channel," in *Proc. of MILCOM '91*, pp. 291–294, 1991.

45. Y. Bar-Ness and N. J. M. van Waes, "Multistage detector for adaptive separation of QAM-modulated multiusers CDMA signals," in *Proc. IEEE Int. Symposium on Spread Spectrum Techniques and Applications*, (Sun City, South Africa), pp. 927–931, Sept. 1998.
46. N. van Waes and Y. Bar-Ness, "The complex bootstrap algorithm for blind separation of co-channel QAM signals," *Wireless Personal Communications, An International Journal*, Kluwer Publishers, forthcoming.
47. S. Haykin, *Adaptive Filter Theory*. Upper Saddle River, NJ, U.S.A: Prentice Hall, third ed., 1996.
48. M. A. Visser and Y. Bar-Ness, "Adaptive reduced complexity multi-carrier CDMA (MC-CDMA) structure for downlink PCS," *to appear in the special issue on Multi-Carrier Spread-Spectrum of the European Transactions on Telecommunications*.
49. M. A. Visser and Y. Bar-Ness, "OFDM frequency offset correction using an adaptive decorrelator," in *Proc. of the 32nd Annual Conference on Information Sciences and Systems*, (Princeton, NJ, U.S.A.), pp. 483–488, Mar. 1998.
50. W. C. Jakes, Jr., *Microwave Mobile Communications*. New York, NY, U.S.A.: John Wiley and Sons, 1974.
51. P. A. Bello, "Characterization of randomly time-variant linear channels," *IEEE Transactions on Communications Systems*, vol. 11, pp. 360–393, Dec. 1963.
52. A. Leon-Garcia, *Probability and Random Processes for Electrical Engineering*. Reading, MA, U.S.A.: Addison-Wesley, second ed., 1994.